TUM SCHOOL OF
NATURAL SCIENCES

TECHNICAL UNIVERSITY OF MUNICH

Dissertation

Multi-Scale Tight Binding Model for Optoelectronic Properties of Hybrid Halide Perovskites

Maximilian Schilcher

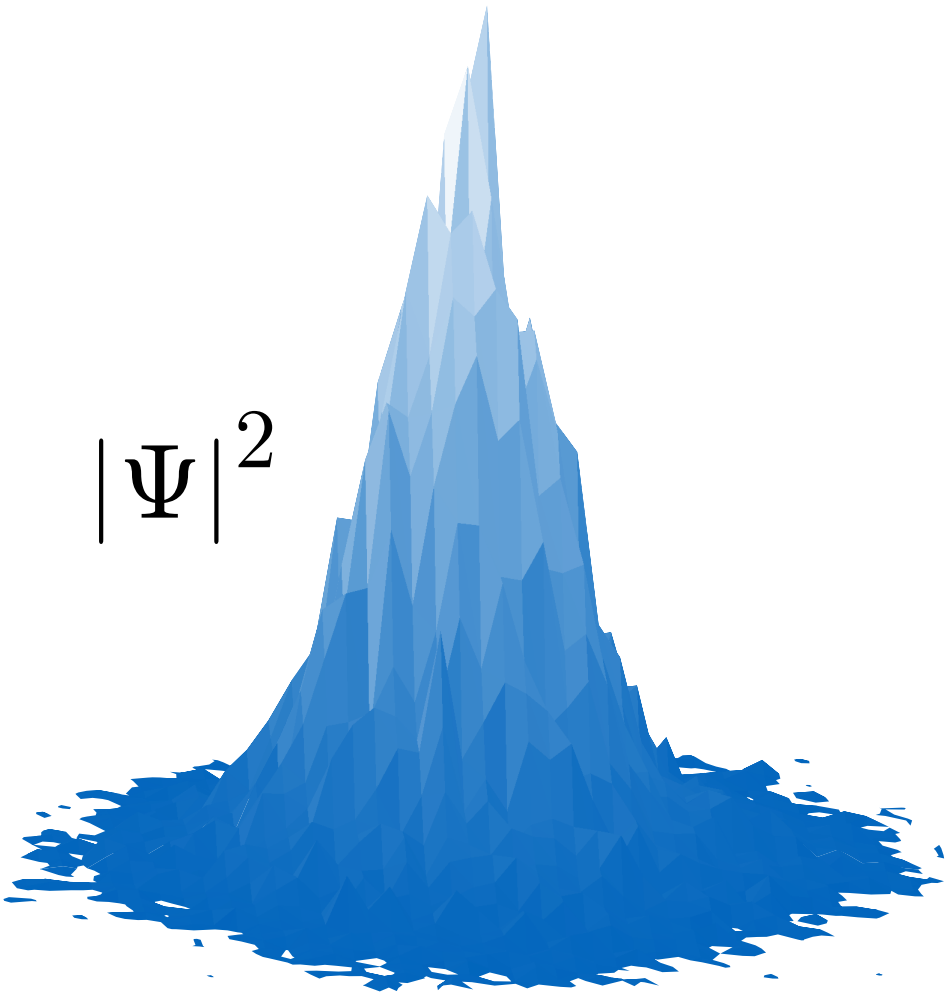

Technische Universität München
TUM School of Natural Sciences

Multi-Scale Tight Binding Model for Optoelectronic Properties of Hybrid Halide Perovskites

Maximilian J. Schilcher

Vollständiger Abdruck der von der TUM School of Natural Sciences der Technischen Universität München zur Erlangung eines

Doktors der Naturwissenschaften (Dr. rer. nat.)

genehmigten Dissertation.

Vorsitz: Prof. Dr. Julia Herzen

Prüfer*innen der Dissertation:

1. Prof. Dr. David Egger
2. Prof. Dr. Linn Leppert

Die Dissertation wurde am 06.11.2023 bei der Technischen Universität München eingereicht und durch die TUM School of Natural Sciences am 04.12.2023 angenommen.

Acknowledgments

First and foremost, I would like to express my deepest gratitude to my supervisor, Prof. Dr. David Egger, for his support during the last few years. He never lost patience and always gave me valuable advice when I needed it. I am also grateful to my mentor, Dr. Bernhard Kretz. His advice, especially regarding IT and supercomputers, was always helpful.

In my work, I have benefited a lot from the support of various collaborators. First, I would like to mention Matt Mayers, from whom I learned the basics of the multi-scale TB model during a visit to Columbia University. Much-appreciated assistance in this regard also came from Liang Tan and David Abramovitch. All three never hesitated to answer any questions and provide me with helpful code. Furthermore, my appreciation also goes to my collaborators Dave Reichman, Andrew Rappe, and Paul Robinson.

During the time of my work in the TheoFEM group in Munich (which emerged from the CMS group in Regensburg), I not only enjoyed the fruitful discussions with all group members very much but also many social activities. For example, the enthusiastic foosball games and vacations in Jerusalem after a scientific stay at the Weizmann Institute. I would like to thank Martin Schwade, for whom I had the pleasure of being an advisor during his master's thesis before he joined the group as a PhD student. I also learned a lot from him about tight binding and other topics.

I thankfully acknowledge the Gauss Centre for Supercomputing e.V. for providing computing time through the John von Neumann Institute for Computing on the GCS Supercomputer JUWELS at Jülich Supercomputing Centre.

Finally, I would also like to thank my family and my girlfriend Wan-Hua, for their emotional support during all that time.

Abstract

Solar cells based on halide perovskites (HaPs) have reached enormous power conversion efficiencies in a short time and are already close to the performance of silicon devices. This is due to their notable optoelectronic properties, but it is still an open question how these can arise despite the remarkably soft lattice of HaPs.

In a traditional framework, the interaction between charge carriers and polar lattice vibrations is often described by the Fröhlich Hamiltonian, which is based on certain approximations such as linear electron-phonon coupling, leading to the formation of large polarons. While there is undoubtedly some degree of polaronic behavior in HaPs, it becomes evident that several fundamental assumptions underlying the large-polaron formalism consistently conflict with the microscopic behavior of these materials, as indicated by numerous experimental studies. We introduce an alternative approach - the dynamic disorder concept.

Based on this, traditional theoretical calculations can reveal important structure-function relations in HaPs. However, these calculations are often limited by computational costs. An efficient approach to modeling large-scale structural distortions is the tight binding (TB) formalism, which operates at much lower computational complexity compared to, e.g., density functional theory. We parameterize a multi-scale TB model (based on the approach from Ref. [5]) for the two hybrid HaPs $MAPbI_3$ and $MAPbBr_3$ with the help of first-principles calculations, projecting the Bloch wavefunctions on basis functions corresponding to specific orbitals of the atoms. Our goal is to combine this TB scheme with molecular dynamics and semiclassical Ehrenfest dynamics simulations to examine the effects of structural distortions, vibrational anharmonicity, and dynamic disorder on the optoelectronic properties of HaPs.

Our multi-scale model helps reconcile the discrepancies between experimental observations and the large-polaron theory. Aligning with experimental findings, we explain the differences in temperature-dependent charge carrier mobilities in $MAPbI_3$ and $MAPbBr_3$ across structural phase transitions. Building upon these discoveries, our model not only improves the prediction of electronic conductivity but also offers valuable guidance for tailoring the characteristics of charge transport in anharmonic semiconductors.

In summary, we present a multi-scale TB model for the hybrid HaPs $MAPbI_3$ and $MAPbBr_3$, investigating the impact of anharmonicity and dynamic disorder on their optoelectronic properties, including charge carrier mobilities.

Kurzfassung

Solarzellen auf Basis von Halogenperowskiten (HaPs) haben in kurzer Zeit enorm hohe Wirkungsgrade bei der Energieumwandlung erreicht und liegen bereits nahe an der Leistung von Silizium-Solarzellen. Dies ist auf ihre beachtlichen optoelektronischen Eigenschaften zurückzuführen, aber es bleibt eine offene Frage, wie diese trotz des bemerkenswert weichen Gitters von HaPs zustande kommen.

In einem traditionellen Rahmen wird die Wechselwirkung zwischen Ladungsträgern und polaren Gitterschwingungen oft mit dem Fröhlich-Hamiltonian beschrieben, der auf bestimmten Näherungen wie der linearen Elektron-Phonon-Kopplung beruht, was zur Bildung großer Polaronen führt. Obwohl es zweifellos ein gewisses Maß an polaronischem Verhalten in HaPs gibt, wird deutlich, dass mehrere grundlegende Annahmen, die dem Formalismus der großen Polaronen zugrunde liegen, im Widerspruch zum mikroskopischen Verhalten dieser Materialien stehen, wie zahlreiche experimentelle Studien zeigen. Wir führen einen alternativen Ansatz ein - das Konzept der dynamischen Unordnung.

Auf dieser Grundlage können herkömmliche theoretische Berechnungen wichtige Struktur-Funktions-Beziehungen in HaPs aufdecken. Diese Berechnungen sind jedoch oft durch den Rechenaufwand begrenzt. Ein effizienter Ansatz zur Modellierung struktureller Verzerrungen ist der Tight-Binding-Formalismus (TB), der deutlich weniger rechenintensiv ist als beispielsweise die Dichtefunktionaltheorie. Wir parametrisieren ein Multiskalen-TB-Modell (basierend auf Ref. [5]) für die beiden hybriden HaPs $MAPbI_3$ und $MAPbBr_3$ durch First-Principles-Rechnungen, indem wir die Bloch-Wellenfunktionen auf Basisfunktionen projizieren, die bestimmten Atom-Orbitalen entsprechen. Wir kombinieren dieses TB-Schema mit Molekulardynamik- und semiklassischen Ehrenfest-Dynamik-Simulationen, um die Auswirkungen von strukturellen Verzerrungen, Schwingungsanharmonizität und dynamischer Unordnung auf die optoelektronischen Eigenschaften von HaPs zu untersuchen.

Unser Multiskalenmodell trägt dazu bei, die Diskrepanzen zwischen den experimentellen Beobachtungen und der Theorie der großen Polaronen in Einklang zu bringen und erklärt die Unterschiede in der temperaturabhängigen Ladungsträgermobilität in $MAPbI_3$ und $MAPbBr_3$ bei strukturellen Phasenübergängen. Unser Modell bietet deshalb wertvolle Hinweise für die Anpassung des Ladungstransports in anharmonischen Halbleitern.

Zusammenfassend stellen wir ein Multiskalen-TB-Modell für die hybriden HaPs $MAPbI_3$ und $MAPbBr_3$ vor und untersuchen die Auswirkungen von Anharmonizität und dynamischer Unordnung auf ihre optoelektronischen Eigenschaften, einschließlich der Ladungsträgermobilitäten.

List of Publications

The research of this work was started in the Computational Materials Physics research group at the University of Regensburg and continued in the Theory of Functional Energy Materials research group at the Technical University of Munich. Some of the findings of this research have been published in the following peer-reviewed publications:

[1] M. J. Schilcher, P. J. Robinson, D. J. Abramovitch, L. Z. Tan, A. M. Rappe, D. R. Reichman, D. A. Egger, *ACS Energy Lett.* **2021**, *6*, 2162–2173.

[2] M. J. Schilcher, D. J. Abramovitch, M. Z. Mayers, L. Z. Tan, D. R. Reichman, D. A. Egger, *Phys. Rev. Materials* **2023**, *7*, L081601.

[3] M. Schwade, M. J. Schilcher, C. R. Baecker, M. Grumet, D. A. Egger, **2023**, DOI 10.48550/ARXIV.2308.08897.

[4] E. Sirotti, L. I. Wagner, C.-M. Jiang, J. Eichhorn, F. Munnik, V. Streibel, M. J. Schilcher, B. März, M. Kuhl, M. Höldrich, D. A. Egger, I. D. Sharp, *in preparation* **2023**.

Contents

1 Introduction

The production of renewable energy has long been recognized as one of the most significant socio-political challenges, even before the ever-increasing importance of climate change. Our society has realized that we must transcend the fossil fuel era. Among various clean energy sources, photovoltaics (PV) holds great promise. It involves the conversion of light into electricity using semiconductor materials that exhibit the photovoltaic effect, closely related to the photoelectric effect. However, scientific challenges still exist, particularly in implementing large-scale solar cell arrays and improving overall efficiency. It is important to acknowledge that the sun represents an immense energy source, emitting over 120 Petawatts of power annually. Just one hour of this energy could meet the entire year's energy needs of the global population [6]. Furthermore, solar power is rapidly becoming, or already is, the most cost-effective technology for electricity generation in many regions worldwide, with costs as low as 4 cents per kilowatt-hour [7]. This achievement can be attributed, in part, to the significant cost reduction of crystalline silicon technology, among other contributing factors [8].

To lower energy generation costs even further, there are several possibilities, such as the use of thin-film strategies and an increase in power conversion efficiency (ratio between the effective power output of an energy conversion machine and the energy input). This can be achieved by advanced techniques such as multi-junction approaches or multi-exciton generations. There are also materials like Gallium arsenide (GaAs) that can lead to an efficiency of 28% [6], which is close to the fundamental limit of about 33% as discovered by Shockley and Queisser [9]. However, much effort and expensive procedures are necessary to build devices that use GaAs. Therefore, the discovery of novel functional materials that are also cost-efficient remains a major challenge towards more efficient sustainable energy conversion.

However, a new class of materials, which are very promising in energy conversion through photovoltaics, is emerging: Halide perovskites (HaPs). Perovskites are certain solid-state materials consisting of cations and anions arranged in a specific manner. Hybrid HaPs were discovered in Stuttgart in 1978 [10] when they were characterized by Weber and co-workers for the first time. Despite their close structural relationship to oxides, they behave differently: they can contain organic and inorganic parts (hence the addition of "hybrid"), making their production very simple and cheap compared to GaAs and other inorganic semiconductors. Nevertheless, the potential of these perovskites for use in solar cells was not discovered until 2009 [11]. Much research has been done since then [11–19], achieving remarkable progress in PV-conversion efficiency for devices based on bulk HaPs [20–23]. Moreover, these devices can be produced by low-temperature procedures. Optimizing them has been much quicker than for established PV materials, where it has taken decades

of research. However, we still face the challenge of understanding the physical and chemical reasons for this enormous PV-conversion efficiency of HaPs. Only with a profound knowledge of them can it be possible to make these materials even more stable or to remove the often contained but toxic element lead, with possibly even higher efficiencies. To summarize, the fascinating physical properties of HaPs are far from understood [24].

Having explored the significance of HaPs for efficient energy conversion, it is not surprising that substantial research efforts have been undertaken in a growing scientific community. Recent years have witnessed a surge in investigations owing to the multifaceted potential of HaPs. This has led to exploring their intriguing intrinsic, structural, and optoelectronic properties. One of the most distinctive and important of these properties is their mechanical softness. This means that the equilibrium configuration of the constituent atoms can be altered with relative ease. The ordered crystalline arrangement in the perovskite structure emerges primarily when considering a macroscopic crystal size. However, on significantly smaller length scales, the atomic lattice encounters pronounced distortions, subsequently impacting the electronic configuration. This remarkable phenomenon is hereby referred to as "dynamic disorder". Even though the motion of charge carriers occurs on temporal scales shorter than atomic motion, it is plausible to deduce their susceptibility to these atomic dynamics. Consequently, the conversion of solar energy into electrical power might also be influenced by these interactions.

Another pivotal issue is the discrepancy between theoretical predictions and experimental observations. Currently, there is an increasing amount of evidence that the established theories of semiconductor physics do not readily transfer to the intricate charge carrier dynamics in HaPs [1]. This puzzle is closely linked to the aforementioned mechanical flexibility of hybrid HaPs. In addition, the exceptional absorption rates characterized by small Urbach energies (approximately 15 meV at room temperature) [25–29] are fascinating, especially considering the concurrent dynamic disorder. The extraordinary absorption capability forms the basis for the fabrication of ultrathin solar cells. Conventionally, disorder would typically result in band smearing, yet curiously, such is not the case here.

In the pursuit of investigating these issues and other material properties, the use of computers proves immensely valuable. Computational methods enable us to perform complex numerical procedures in conjunction with precise experimental approaches. The aim is to employ atomistic calculations that comprehensively describe chemical and physical phenomena. A range of conventional and well-established methods exists in solid-state physics to tackle such challenges. Referred to as first-principles methods, these approaches are solely grounded in the quantum theory of matter and the Schrödinger or Dirac equations governing multi-particle systems. Here, the incorporation of additional empirical data or external input is unnecessary. Among these methods, density functional theory (DFT) is the most prevalent theoretical tool, which addresses the Kohn-Sham equations for individual particles by employing suitable approximations for the exchange-correlation functional.

This approach effectively computes properties such as total energy and electron density, particularly for simple crystals. It is common practice to use a harmonic approximation for lattice vibrations and linear electron-phonon coupling. However, as previously highlighted, HaPs exhibit mechanical softness. This characteristic might underlie the theory-experiment disparities encountered. Thus, going beyond the confines of the harmonic approximation and linear electron-phonon coupling becomes necessary. The complexity of these challenges is enhanced by their multi-scale characteristics: we have to formulate a multi-scale model capable of predicting optoelectronic properties of hybrid HaPs. Progress in this domain could reverberate across other materials, including conventional oxide perovskites like $SrTiO_3$ and organic crystals [30].

A prerequisite for an alternative formalism lies in its capacity to simulate realistic multi-electron systems with low computational costs, all while upholding the precision required for reliable, first-principles-based predictions of material properties. This is why we turn to the tight binding (TB) model when delineating materials like hybrid HaPs - a straightforward and effective model applicable across a broad spectrum of scenarios. The primary reason behind this choice is obvious: the computational demands of this approach are remarkably low. The traditional scaling of standard DFT resides at $\mathcal{O}(n^3)$ [31] (with n denoting the particle number), whereas that of TB stands at $\mathcal{O}(n)$ [32, 33]. However, this disparity in scaling is not the only determinant of TB's heightened efficiency compared to DFT, as the $\mathcal{O}(n^3)$ scaling is not intrinsic to DFT and can be mitigated through sophisticated implementation. In reality, the prefactor accompanying the respective order of scaling is notably larger in DFT. This underlines why TB facilitates computations involving materials composed of a large number of atoms. While DFT typically allows calculations for systems with around 100 atoms, TB extends its scope to cells with about 10,000 or more atoms. In broader terms, developing an efficient TB model for the hybrid HaP domain could provide support for the fascinating field of data-driven materials science.

However, it is important to note that TB does not fall under the category of first-principles methods. For that reason, empirical parameters must be supplied for TB to operate effectively. This requires the use of molecular dynamics (MD) trajectories and DFT calculations to parameterize our TB model. Once this parameterization is accomplished, TB operates independently of DFT calculations. Furthermore, MD is employed to provide input for the TB model, thereby enabling the computation of realistic properties for hybrid HaPs. MD stands as a parameter-free model devoid of assumptions regarding the harmonic motion of ion movement. This approach ensures that the anharmonic behavior at each temperature is accurately computed, obviating the need for a harmonic approximation of phonons. By combining MD and TB, we can thus obtain a comprehensive treatment of the electron-phonon coupling, bridging a crucial gap in our understanding.

To encapsulate, our main goal is to formulate a TB model that is specifically tailored for hybrid HaPs and enables the computation of realistic optoelectronic properties. Importantly, we highlight again that the TB model, while not precisely a first-principles approach, still relies on material-specific parameters. The determination

of these parameters is an essential task in which DFT is indispensable. However, we can carry out independent TB calculations once this parameterization is done. This workflow is depicted in the schematic diagram in Fig. 1.1.

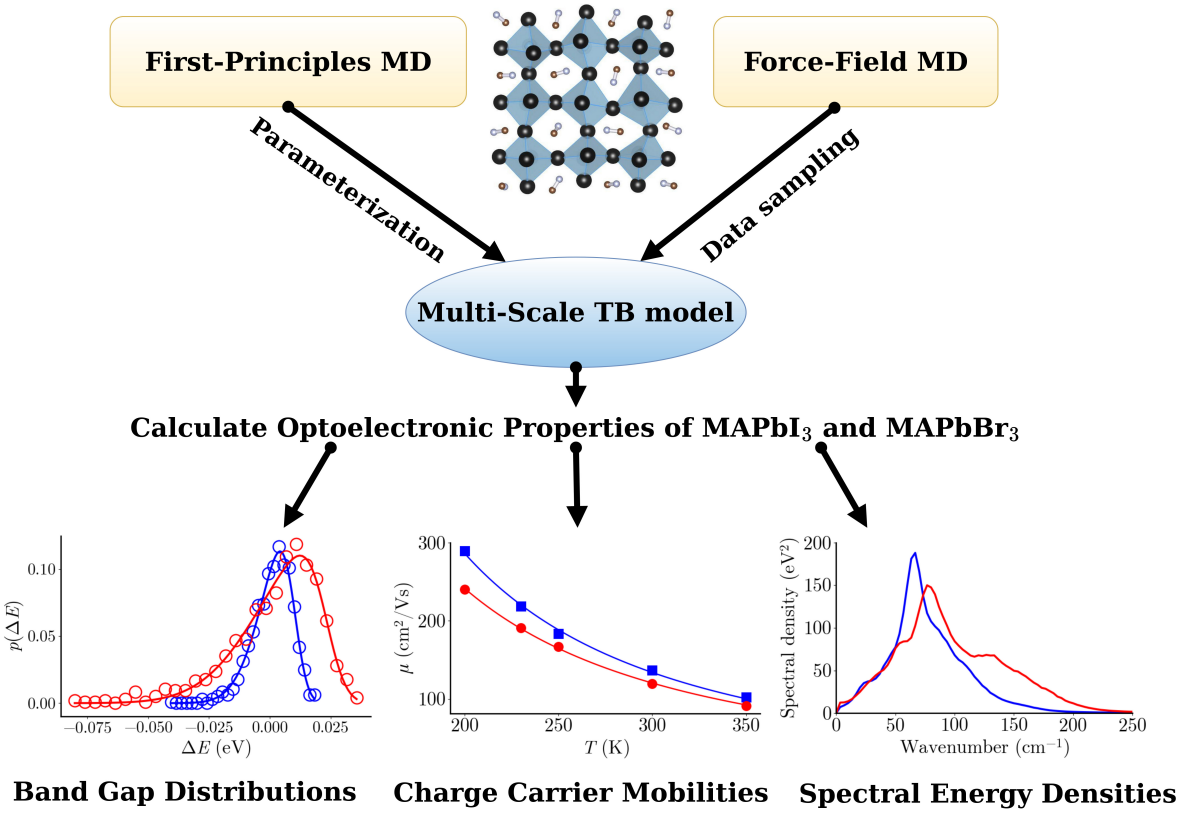

Figure 1.1: Schematic illustrating the process of constructing and employing the multi-scale TB model.

2 Theory

The world around us consists of atoms, which are themselves composed of atomic nuclei and electrons. The interplay between these constituents is fundamentally rooted in electrostatic and electronic interactions, governing the optoelectronic characteristics of materials. Exploring these materials holds the promise of yielding both breakthroughs and practical advancements. Notably, this domain has earned significant recognition, as evidenced, for example, by numerous Nobel Prizes in recent decades.

In general, the behavior of quantum mechanical particles can be precisely described by solving the corresponding Schrödinger equation. However, when dealing with a solid, the sheer quantity of particles - approximately 10^{23} per cm^3 - renders this issue a many-body problem that defies analytical solutions. Yet, it is within this complexity that we encounter unforeseen physical phenomena. For that reason, theoretical solid-state physics strives to forge and apply clever approximations, fostering comprehension of material properties.

Unless explicitly cited, the theoretical framework presented in this chapter draws from the foundational textbooks from Refs. [34–43]. Additionally, we make use of online resources such as Refs. [44–46].

2.1 The Many-Particle Problem

From the viewpoint of quantum mechanics, the nuclei and electrons constituting a solid can be elegantly encapsulated in a wavefunction denoted as $\Psi(\{\mathbf{r}_i\}, \{\mathbf{R}_I\}, t)$ which inherently depends on the electronic ($\{\mathbf{r}_i\}$) and nuclear ($\{\mathbf{R}_I\}$) degrees of freedom. This wavefunction obeys the principles of the time-dependent Schrödinger equation, given by

$$i\hbar \frac{\partial \Psi}{\partial t} = \hat{H}\Psi. \tag{2.1}$$

Here and in the following, $\hbar$ denotes the reduced Planck constant. It is important to recognize that the description presented here is based on a non-relativistic approach. The consideration of relativistic effects introduces a spin-orbit coupling (SOC) contribution, which is of paramount importance in our TB model and will be discussed in Sections 2.2.2 and 2.3.4. The Hamiltonian operator acting upon the wavefunction is

depicted as

$$\hat{H} = \underbrace{-\sum_i \frac{\hbar^2}{2m_\mathrm{e}}\nabla_i^2}_{\hat{T}_\mathrm{e}} \underbrace{-\sum_I \frac{\hbar^2}{2M_I}\nabla_I^2}_{\hat{T}_\mathrm{n}} + \frac{1}{4\pi\epsilon_0}\left(\underbrace{\sum_{i<j}\frac{e^2}{|\mathbf{r}_i-\mathbf{r}_j|}}_{\hat{V}_{\mathrm{e-e}}} \underbrace{-\sum_{i,I}\frac{Z_I e^2}{|\mathbf{R}_i-\mathbf{r}_I|}}_{\hat{V}_{\mathrm{e-n}}} + \underbrace{\sum_{I<J}\frac{Z_I Z_J e^2}{|\mathbf{R}_I-\mathbf{R}_J|}}_{\hat{V}_{\mathrm{n-n}}}\right). \tag{2.2}$$

The five terms encompass the kinetic energy operators of both electrons and nuclei ($\hat{T}_\mathrm{e}$ and $\hat{T}_\mathrm{n}$), as well as the Coulomb interaction operator involving electrons ($\hat{V}_{\mathrm{e-e}}$), the Coulomb interaction operator between electrons and nuclei ($\hat{V}_{\mathrm{e-n}}$) and the Coulomb interaction operator among nuclei ($\hat{V}_{\mathrm{n-n}}$). The summation denoted by $\sum_{i<j}$ operates over unique pairs of indices i and j, excluding cases where $i = j$. Here, Z_I and M_I represent the atomic number and mass of the I-th nucleus, respectively, while m_e and e denote the electron mass and charge, and ϵ_0 stands for vacuum permittivity.

As previously noted, solving the Schrödinger equation for real-world materials proves infeasible owing to the substantial number of particles in solid materials. Moreover, obtaining a numerical solution would exhibit an exponential scaling of e^N, where N signifies the particle number. Consequently, it becomes inevitable to employ sophisticated methodologies that enable the computation of approximate solutions.

Many of the methods employed in this context, such as the Hartree-Fock Method or DFT, employ a technique known as the mean-field approximation. This approximation hinges on the assumption that the intricate interplay between particles can be simplified. Essentially, we posit that the interaction between pairs of particles can be collectively represented as a summation over an effective and averaged potential. Remarkably, this potential relies solely upon the spatial coordinates of individual particles. To be more specific, this implies that the term responsible for electron-electron interaction can be written as

$$\frac{1}{4\pi\epsilon_0}\sum_{i<j}\frac{e^2}{|\mathbf{r}_i-\mathbf{r}_j|} \approx \sum_i \hat{V}_\mathrm{int}(\mathbf{r}_i). \tag{2.3}$$

Here, the complex many-body problem of particles interacting is thereby approximated as a set of single-particle Schrödinger equations, one for each particle. This reduction allows us to tackle the Schrödinger equation for a system of N particles as an equivalent task of solving the one-particle Schrödinger equation N times over.

2.1.1 Born-Oppenheimer Approximation

We can decompose equation 2.2 into distinct components: the contributions of kinetic energy stemming from the nuclei and an electronic Hamiltonian:

$$\hat{H} = -\sum_I \frac{\hbar^2}{2M_I}\nabla_I^2 + \hat{H}_\mathrm{e}(\{\mathbf{r}_i\},\{\mathbf{R}_I\}). \tag{2.4}$$

In addition, we assume the existence of a set of wavefunctions $\psi_i(\{\mathbf{r}_i\},\{\mathbf{R}_I\})$ that satisfy the stationary electronic Schrödinger equation

$$\hat{H}_\mathrm{e}\psi_i = E_i\psi_i. \tag{2.5}$$

This leads to a plausible solution $\Psi_s(\{\mathbf{r}_i\},\{\mathbf{R}_I\},t)$ for the total wavefunction, employing the quasi-separable ansatz

$$\Psi_s(\{\mathbf{r}_i\},\{\mathbf{R}_I\},t) = \sum_i \psi_i(\{\mathbf{r}_i\},\{\mathbf{R}_I\})\chi_{si}(\{\mathbf{R}_I\},t). \tag{2.6}$$

Here, the expansion coefficients $\chi_{si}(\{\mathbf{R_I}\},t)$ represent the nuclear wavefunctions that carry the temporal dependence. By inserting this wavefunction into the pertinent Schrödinger equation 2.1, then multiplying both sides by ψ_k^* and integrating over all electronic coordinates, the following expression emerges:

$$\int \psi_k^* \left(\mathrm{i}\hbar\frac{\partial}{\partial t}\right)\sum_i \psi_i\chi_{si}\,\mathrm{d}\mathbf{r} = \int \psi_k^* \left(-\sum_I \frac{\hbar^2}{2M_I}\nabla_I^2 + \hat{H}_\mathrm{e}\right)\sum_i \psi_i\chi_{si}\,\mathrm{d}\mathbf{r}. \tag{2.7}$$

As the electronic wavefunction remains independent of time, we can move the time derivative out of the integral as far as the left-hand side of the equation is concerned. Given our assumption of the electronic wavefunction's orthonormality ($\int \psi_k^*\psi_i\,\mathrm{d}\mathbf{r} = \delta_{ki}$), the resulting sum and integral simplify into a single term χ_{sk}. On the right-hand side of the equation, rearranging the order of the wavefunction and the operators is not straightforward since we cannot change the order of the product $\psi_i\chi_{si}$. Instead, we exploit the commutator involving the momentum operator $\hat{p} = -\mathrm{i}\hbar\nabla$ which reads

$$[\hat{p}^2,\psi_i]\chi_{si} = -\hbar^2\left[\nabla^2\psi_i - \psi_i\nabla^2\right]\chi_{si} = -\hbar^2\left[\chi_{si}\nabla^2\psi_i + 2\nabla\psi_i\cdot\nabla\chi_{si}\right]. \tag{2.8}$$

By employing this relation alongside equation 2.5, we arrive at an expression for equation 2.7 that reads

$$\left[-\sum_I \frac{\hbar^2}{2M_I}\nabla_I^2 + E_k(\{\mathbf{R}_I\})\right]\chi_{sk} + \sum_i C_{ki}\chi_{si} = \mathrm{i}\hbar\frac{\partial}{\partial t}\chi_{sk}. \tag{2.9}$$

The matrix elements $C_{ki} = A_{ki} + B_{ki}$ can be explicitly defined as

$$A_{ki} = \sum_I \frac{-\hbar^2}{M_I}\left[\int \psi_k^*(\nabla_I)\psi_i\,\mathrm{d}\mathbf{r}\right]\nabla_I, \tag{2.10}$$

$$B_{ki} = \sum_I \frac{-\hbar^2}{2M_I}\int \psi_k^*\nabla_I^2\psi_i\,\mathrm{d}\mathbf{r}. \tag{2.11}$$

Here, the adiabatic approximation, commonly known as neglecting all off-diagonal terms in C_{ki}, emerges. Furthermore, due to the normalization of ψ_i, it follows that $A_{kk} = 0$. Thus, equation 2.9 becomes

$$\left[-\sum_I \frac{\hbar^2}{2M_I}\nabla_I^2 + E_k(\{\mathbf{R}_I\}) + C_{kk}(\{\mathbf{R}_I\})\right]\chi_{sk} = \mathrm{i}\hbar\frac{\partial}{\partial t}\chi_{sk} \tag{2.12}$$

where

$$C_{kk} = -\sum_I \frac{\hbar^2}{2M_I} \int \psi_k^* \nabla_I^2 \psi_k \, \mathrm{d}\mathbf{r}. \tag{2.13}$$

This describes the complete separation of the original differential equations, implying that the electrons retain a specific state while the nuclei undergo motion. Accordingly, we can approximate the coupled wavefunctions as $\Psi_s(\{\mathbf{r}_i\}, \{\mathbf{R}_I\}, t) = \psi_k(\{\mathbf{r}_i\}, \{\mathbf{R}_I\})\chi_{sk}(\{\mathbf{R}_I\}, t)$. This approximation involves the multiplication of an electronic and a nuclear wavefunction, capturing the primary interactions.

In a further step, we can even neglect the diagonal terms. This translates to the complete neglect of the coupling matrix C_{kk}, rendering the nuclear motion entirely describable through a pure nuclear equation utilizing the potential E_k. This theoretical construct, known as the Born-Oppenheimer approximation, gains justification owing to significant mass disparities between electrons and nuclei (resulting in a relatively small term m_e/M_I). Notably, Born and Oppenheimer originally derived this approximation by exploiting a perturbation expansion of the mass ratio $(m_\mathrm{e}/M_I)^{1/4}$ [47]. The Born-Oppenheimer approximation finds widespread use in solid-state theory and prominently surfaces in DFT, as will be explored in the following chapters.

2.1.2 Hartree-Fock Approximation

Upon establishing the possibility of independently treating the electronic and nucleonic components of the many-body Hamiltonian, we proceed to restructure the electronic part, giving it the form

$$\hat{H}_\mathrm{e} = \hat{T}_\mathrm{e} + \hat{V}_\mathrm{ext} + \hat{V}_\mathrm{int}. \tag{2.14}$$

Here, the term $\hat{V}_\mathrm{ext}$ encompasses electron-nuclei interactions, while $\hat{V}_\mathrm{int}$ characterizes electron-electron interactions. Note that in the Born-Oppenheimer approximation, the electrostatic interaction between nuclei is considered a constant and therefore neglected (adding a constant to an operator does not influence the operator eigenfunctions). As previously hinted, our intention is to handle these potentials in the mean-field approximation, rendering them contingent solely on the position of an individual electron. For the external potential, this criterion is already met, and we can express it as

$$\hat{V}_\mathrm{ext}(\mathbf{r}_i) = -e^2 \sum_I \frac{Z_I}{|\mathbf{r}_i - \mathbf{R}_I|}. \tag{2.15}$$

For the sake of simplicity, we omit here and in the following the prefactor $1/4\pi\epsilon_0$. Concerning the internal potential, we postulate that one electron perceives the influence of all other electrons as a smoothed-out charge density $\rho(\mathbf{r})$. In the context of an independent-electron framework, this charge density takes the form

$$\rho(\mathbf{r}) = \sum_j \rho_j(\mathbf{r}) = \sum_j -e|\psi_j(\mathbf{r})|^2 \tag{2.16}$$

with ψ_j representing the respective electronic wavefunction and $\rho_j(\mathbf{r}) = -e|\psi_j(\mathbf{r})|^2$ denoting the charge distribution generated by the respective electron. The internal potential thus adopts the shape

$$\hat{V}_{\text{int}}(\mathbf{r}_i) = -e \int \mathrm{d}\mathbf{r}' \frac{\rho(\mathbf{r}')}{|\mathbf{r}_i - \mathbf{r}'|} = e^2 \sum_j \int \mathrm{d}\mathbf{r}' \frac{|\psi_j(\mathbf{r}')|^2}{|\mathbf{r}_i - \mathbf{r}'|}. \tag{2.17}$$

The resulting stationary one-particle electronic Schrödinger equations are called Hartree equations and read

$$\left(\hat{T}_{\text{e}} + \hat{V}_{\text{ext}}(\mathbf{r}) + \hat{V}_{\text{int}}(\mathbf{r})\right)\psi_i(\mathbf{r}) = \epsilon_i \psi_i(\mathbf{r}). \tag{2.18}$$

However, maintaining the total electronic wavefunction as

$$\psi(\mathbf{r}_1, \sigma_1, ..., \mathbf{r}_N, \sigma_N) = \psi_1(\mathbf{r}_1, \sigma_1) \cdot ... \cdot \psi_N(\mathbf{r}_N, \sigma_N) \tag{2.19}$$

while also introducing spin ($\sigma_i = \pm 1/2$ denotes the magnetic spin quantum numbers of the respective electrons) results in ψ violating the Pauli exclusion principle, which requires a sign change upon interchanging any two of the N particles. This is addressed by adopting a Slater determinant for ψ:

$$\psi(\mathbf{r}_1, \sigma_1, ..., \mathbf{r}_N, \sigma_N) = \frac{1}{\sqrt{N!}} \begin{vmatrix} \psi_1(\mathbf{r}_1, \sigma_1) & \psi_1(\mathbf{r}_2, \sigma_2) & \cdots & \psi_1(\mathbf{r}_N, \sigma_N) \\ \psi_2(\mathbf{r}_1, \sigma_1) & \psi_2(\mathbf{r}_2, \sigma_2) & \cdots & \psi_2(\mathbf{r}_N, \sigma_N) \\ \vdots & \vdots & \ddots & \vdots \\ \psi_N(\mathbf{r}_1, \sigma_1) & \psi_N(\mathbf{r}_2, \sigma_2) & \cdots & \psi_N(\mathbf{r}_N, \sigma_N) \end{vmatrix}. \tag{2.20}$$

Applying the variational principle, minimizing $\langle \hat{H}_{\text{e}} \rangle = \frac{\langle \Psi | \hat{H}_{\text{e}} | \Psi \rangle}{\langle \Psi | \Psi \rangle}$ yields (for convenience we write $\mathbf{r}_i = \mathbf{r}$ and $\sigma_i = \sigma$)

$$\begin{aligned} &(\hat{T}_{\text{e}} + \hat{V}_{\text{ext}}(\mathbf{r}))\psi_i(\mathbf{r}, \sigma) + e^2 \sum_j \sum_{\sigma'} \int \mathrm{d}\mathbf{r}' \, \frac{|\psi_j(\mathbf{r}', \sigma')|^2}{|\mathbf{r} - \mathbf{r}'|} \psi_i(\mathbf{r}, \sigma) \\ &- \sum_j \sum_{\sigma'} \int \mathrm{d}\mathbf{r}' \, \frac{e^2}{|\mathbf{r} - \mathbf{r}'|} \psi_j^*(\mathbf{r}', \sigma') \psi_i(\mathbf{r},' \sigma') \psi_j(\mathbf{r}, \sigma) = \epsilon_i \psi_i(\mathbf{r}, \sigma). \end{aligned} \tag{2.21}$$

This is the Hartree-Fock equation, featuring an extra term on the left side compared to the Hartree equation, which is called the exchange or Fock operator. This operator is a manifestation of purely quantum mechanical principles. Notably, the exchange term encompasses all wavefunctions of the same spin, including the self term ($i = j$), which cancels the unphysical self-term embedded in the direct Coulomb interaction.

Nonetheless, an unaddressed energy component is to consider: the electron correlation energy. The Coulomb interaction not only introduces a direct energy term in the Hamiltonian but also features a dependence between electron movements. While we approximated the interaction of one electron with the others as an interaction with a smoothed-out, averaged electron density, in reality, electron positions also display correlations - a crucial factor omitted in the Hartree-Fock approximation. Mathematically, this discrepancy is reflected in the inequality

$$|\psi(\mathbf{r}_1, \sigma_1, \ldots, \mathbf{r}_N, \sigma_N)|^2 \mathrm{d}\mathbf{r}_1 \ldots \mathrm{d}\mathbf{r}_N \neq |\psi_1(\mathbf{r}_1 \sigma_1)|^2 \mathrm{d}\mathbf{r}_1 \ldots |\psi_N(\mathbf{r}_N \sigma_N)|^2 \mathrm{d}\mathbf{r}_N. \tag{2.22}$$

Hence, the difference between the Hartree-Fock energy and the actual ground-state energy E_0 is termed correlation energy and is defined as

$$E_{\text{corr}} = E_0 - E_{\text{HF}}. \tag{2.23}$$

Although the Hartree-Fock approximation overlooks electron-electron correlation effects, it offers a reasonable description of molecular and solid-state systems. It is a starting point for advanced techniques incorporating electron correlation effects, such as DFT.

2.2 Density Functional Theory

We understand that solving the many-body Hamiltonian poses a big challenge. On the other hand, single-particle theories that employ a mean-field approximation offer a more tractable approach. While the Hartree-Fock method is one example, it falls short in accounting for correlation energies. We require a single-particle theory that encompasses all interactions, extending beyond the scope of Hartree-Fock in a single-particle potential.

Density functional theory (DFT) is one very common tool for this and can be systematically derived based on the Hartree-Fock approximation. The fundamental concept underpinning DFT is a departure from treating the many-body wavefunction as the central descriptor of a system. Instead, we focus on the electron density

$$n(\mathbf{r}) = \langle \Psi | \sum_i \delta(\mathbf{r} - \mathbf{r}_i) | \Psi \rangle = \sum_\sigma \sum_i |\psi_i^\sigma(\mathbf{r})|^2, \tag{2.24}$$

an essential quantity that encapsulates all the relevant information for the ground state.

2.2.1 Hohenberg-Kohn Theorems and Kohn-Sham Map

Modern DFT rests upon two foundational theorems put forth by Hohenberg and Kohn [48], which underpin its framework:

Hohenberg-Kohn Theorem I: The external potential V_{ext} governing a system of interacting particles is uniquely determined from the ground state density $n_0(\mathbf{r})$, up to a constant. This theorem implies that every property of the system can be derived from its ground-state density. This theorem is visually represented in Fig. 2.1.

Hohenberg-Kohn Theorem II: The total energy can be calculated with a functional $E[n]$, dependent on the electron density. The global minimum of this functional defines the exact ground-state energy. Conversely, the density that minimizes the functional corresponds to the exact ground-state density.

At present, our understanding of how to obtain the ground state density or energy remains incomplete. As a result, we substitute the initial complex many-body problem with an auxiliary, independent-particle system. This transition is facilitated

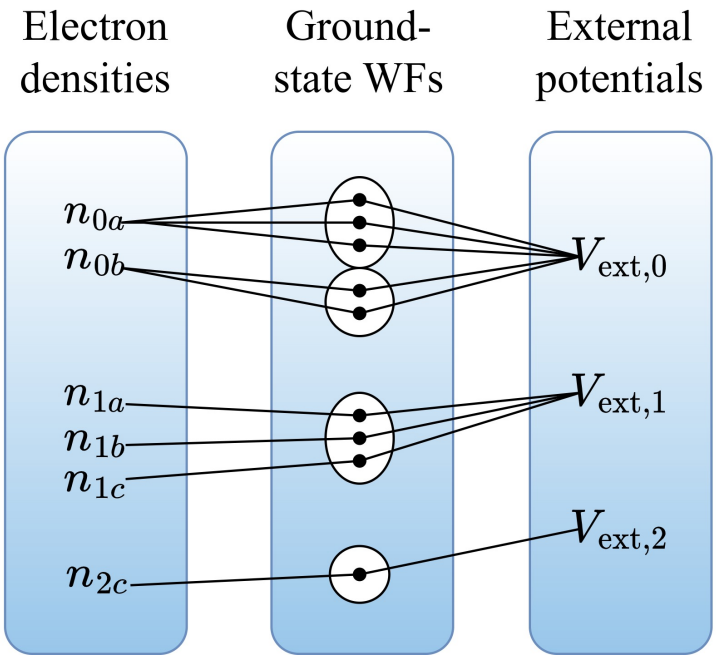

Figure 2.1: Schematic visualizing the Hohenberg-Kohn Theorem I. An external potential can generate different ground-state wavefunctions with different densities; however, two different potentials can never have the same ground-state density.

by utilizing the Kohn-Sham map, as introduced by Kohn and Sham [49]. The Kohn-Sham map transforms the intricacies of the fully interacting system into those of a non-interacting counterpart while conserving identical density attributes. This transformation has the advantage that we can tackle a simplified equation with independent particles while maintaining the accuracy of the ground-state-density representation.

The kinetic energy in this framework of independent particles is expressed as

$$T_s[n(\mathbf{r})] = \frac{1}{2}\sum_{\sigma}\sum_{i}\int \mathrm{d}\mathbf{r}\,\psi_i^*(\mathbf{r})\nabla^2\psi_i(\mathbf{r}). \tag{2.25}$$

Note that $T_s[n] = T_s[\{\psi_i(n)\}]$ represents an explicit orbital functional. At the same time, it serves as an implicit density functional because of its reliance on the density through the wavefunction's dependence. Additionally, the classical Coulombic repulsion corresponds to the familiar Hartree energy

$$E_{\mathrm{H}}[n(\mathbf{r})] = \frac{1}{2}\int \mathrm{d}\mathbf{r}\,\mathrm{d}\mathbf{r}'\frac{n(\mathbf{r})n(\mathbf{r})'}{|\mathbf{r}-\mathbf{r}'|}. \tag{2.26}$$

For the interaction energy arising from the nuclei, it can be written in the form of $E_{\text{ext}}[n(\mathbf{r})] = \int \mathrm{d}\mathbf{r}\,\hat{V}_{\text{ext}}(\mathbf{r})n(\mathbf{r})$. Consequently, the complete Kohn-Sham energy is given by

$$E_{\mathrm{KS}} = T_s[n(\mathbf{r})] + E_{\text{ext}}[n(\mathbf{r})] + E_{\mathrm{H}}[n(\mathbf{r})] + E_{\mathrm{XC}}[n(\mathbf{r})]. \tag{2.27}$$

The terms related to exchange and correlation energy, as well as the remaining discrepancies between the noninteracting and real system, are summarized in E_{XC} (with $\hat{V}_{\mathrm{XC}}$ denoting the respective operator). Therefore, it can be formulated as

$$E_{\mathrm{XC}}[n] = \left\langle \hat{T} \right\rangle - T_{\mathrm{s}}[n] + \left\langle \hat{V}_{\mathrm{int}} \right\rangle - E_{\mathrm{H}}[n]. \tag{2.28}$$

Here, $\left\langle \hat{T} \right\rangle$ and $\left\langle \hat{V}_{\mathrm{int}} \right\rangle$ signify the expectation values of the respective operators of the genuine, fully interacting system. Analogous to the Hartree and Hartree-Fock theories, a solution to this equation is attainable through the variation principle

$$\frac{\delta E_{\mathrm{KS}}}{\delta \psi_i^*(\mathbf{r})} = \frac{\delta T_{\mathrm{s}}}{\delta \psi_i^*(\mathbf{r})} + \left(\underbrace{\frac{\delta E_{\mathrm{ext}}}{\delta n(\mathbf{r})}}_{\hat{V}_{\mathrm{ext}}(\mathbf{r})} + \underbrace{\frac{\delta E_{\mathrm{H}}}{\delta n(\mathbf{r})}}_{\hat{V}_{\mathrm{H}}(\mathbf{r})} + \underbrace{\frac{\delta E_{\mathrm{XC}}}{\delta n(\mathbf{r})}}_{\hat{V}_{\mathrm{XC}}(\mathbf{r})} \right) \frac{\delta n(\mathbf{r})}{\delta \psi_i^*(\mathbf{r})} = 0. \tag{2.29}$$

This leads to Schrödinger-like equations, famously known as the Kohn-Sham equations [49]:

$$\left[-\frac{\hbar^2}{2m_{\mathrm{e}}} \nabla^2 + \hat{V}_{\mathrm{ext}}(\mathbf{r}) + \hat{V}_{\mathrm{H}}(\mathbf{r}) + \hat{V}_{\mathrm{XC}}(\mathbf{r}) \right] \psi_i^{\mathrm{KS}}(\mathbf{r}) = \varepsilon_i^{\mathrm{KS}} \psi_i^{\mathrm{KS}}(\mathbf{r}). \tag{2.30}$$

These three potentials can be consolidated into what is referred to as the Kohn-Sham potential: $\hat{V}_{KS} = \hat{V}_{\mathrm{ext}}(\mathbf{r}) + \hat{V}_{\mathrm{H}}(\mathbf{r}) + \hat{V}_{\mathrm{XC}}(\mathbf{r})$. If we possessed a precise, universal way to calculate E_{XC}, we could directly determine the exact ground-state density and energy of the many-body problem by solving the KS equations. Yet, this remains elusive, necessitating the formulation of useful and sophisticated approximations. Some of these approximations will be explored in the subsequent sections.

Nevertheless, up to this stage, the utility of the KS equations might not be readily apparent. After all, our focus is on the ground-state density, which, in turn, is required to solve the KS equations. In practice, a refined estimation of the charge densities is needed as a starting point, and subsequently, these are used to solve the KS equations and calculate updated charge densities. These newly calculated densities then serve as inputs for the procedure. Only when these iterated densities hardly differ (i.e., converge) are they utilized to extract further system properties through post-processing calculations. This iterative and self-consistent process is depicted in Fig. 2.2.

2.2.2 Spin-Orbit Coupling in DFT

The presence of SOC leads to further interaction terms, which we have thus far omitted. It is evident that SOC holds significant relevance for heavy elements, as they can appear in HaPs, exerting a considerable impact on their electronic structures. Hence, we briefly discuss how DFT can be expanded to encompass SOC effects. This expansion holds pertinence not only for our current discussions but also for the subsequent development of our TB model.

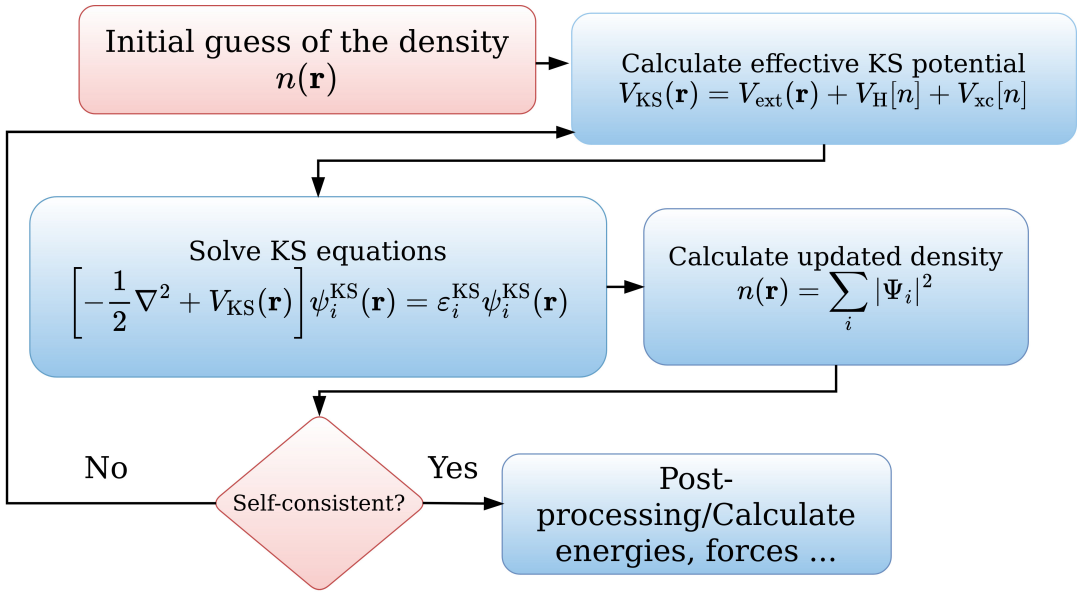

Figure 2.2: Schematic visualizing the self-consistent algorithm for solving the KS equations.

The foundation for elucidating the impact of SOC arises from the relativistic Dirac equation

$$(\mathrm{i}\hbar\gamma^\mu\partial_\mu - mc)\psi(\mathbf{r},t) = 0, \tag{2.31}$$

where γ^μ represent the four Dirac matrices for fermions, and

$$\partial_\mu = \left(\frac{\partial}{\partial ct}, \frac{\partial}{\partial x}, \frac{\partial}{\partial y}, \quad \frac{\partial}{\partial z}\right), \partial^\mu = \left(\frac{\partial}{\partial ct}, -\frac{\partial}{\partial x}, -\frac{\partial}{\partial y}, -\frac{\partial}{\partial z}\right). \tag{2.32}$$

It is important to note that the upper and lower index $\mu = 1,2,3,4$ appearing together in one formula indicates summation. In this context, Ψ is a 4-component spinor. The Dirac matrices are given by

$$\gamma_i = -\gamma_i \begin{pmatrix} 0 & \sigma_i \\ -\sigma_i & 0 \end{pmatrix} \quad \text{for} \quad i = 1,2,3 \quad \text{and} \quad \gamma_0 = \begin{pmatrix} \mathbf{1} & 0 \\ 0 & \mathbf{1} \end{pmatrix}. \tag{2.33}$$

Here, σ_i are the three Pauli matrices, and $\mathbf{1}$ represents the 2×2 unit matrix. To tackle the Dirac equation, a straightforward ansatz can be adopted:

$$\psi(\mathbf{r},t) = e^{-\mathrm{i}Et/\hbar} \begin{pmatrix} \psi(\mathbf{r}) \\ \chi(\mathbf{r}) \end{pmatrix}, \tag{2.34}$$

where $\psi(\mathbf{r})$ and $\chi(\mathbf{r})$ are stationary two-component spinors that characterize both the spatial and spin-related degrees of freedom. In scenarios where electron energies are significantly lower than the rest mass energy, $\chi(\mathbf{r})$ can be treated as a perturbation. As a result, it can be demonstrated that a Schrödinger-like equation emerges for $\psi(\mathbf{r}) = (\psi_\uparrow(\mathbf{r}), \psi_\downarrow(\mathbf{r}))$, featuring an additional SOC contribution, that reads

$$H_{\mathrm{SOC}} = \frac{e\hbar}{4m^2c^2}(\mathbf{p} \times \nabla V) \cdot \boldsymbol{\sigma}. \tag{2.35}$$

In this context, $\boldsymbol{\sigma} = (\sigma_x, \sigma_y, \sigma_z)$ represents the spin vector using the basis of the Pauli matrices. The term ∇V can be understood as an electric field induced by an electron with spin $\boldsymbol{\sigma}$, implying that the expression $(\mathbf{p} \times \nabla V)$ characterizes the interplay between the moving electron and its own spin.

2.2.3 Exchange-Correlation Functionals

As previously indicated, in DFT, the intricacies of the many-body problem are predominantly encapsulated in the exchange-correlation energy $E_{\mathrm{XC}}[n(\mathbf{r})]$. This has led to the development of a broad range of practical and sophisticated approximations, a factor decisive for the immense success of DFT. Among these approximations, two of the simplest yet most widely used are the local spin density Approximation (LSDA) and the generalized gradient approximation (GGA).

In LSDA, we postulate that the electronic behavior of a solid mirrors that of a homogeneous electron gas. This assumption implies that the exchange and correlation energies exhibit pronounced local characteristics, facilitating their computation through

$$E_{\mathrm{XC}}^{\mathrm{LSDA}}[n^{\uparrow}(\mathbf{r}), n^{\downarrow}(\mathbf{r})] = \int \mathrm{d}\mathbf{r}\; n(\mathbf{r}) \left(\epsilon_{\mathrm{X}}^{\mathrm{hom}}(n^{\uparrow}(\mathbf{r}), n^{\downarrow}(\mathbf{r})) + \epsilon_{\mathrm{C}}^{\mathrm{hom}}(n^{\uparrow}(\mathbf{r}), n^{\downarrow}(\mathbf{r})) \right). \quad (2.36)$$

The energies $\epsilon_{\mathrm{X/C}}^{\mathrm{hom}}$ are known analytically for exchange and can be computed with the assistance of quantum mechanical Monte-Carlo methods for correlation [50]. The LSDA functional performs exceptionally well when spatial variations in density are minimal, making it especially suitable for simple crystalline metals. Yet, in real-world solids, conditions frequently deviate from this assumption, thereby leading us to the more intricate realm of GGA.

To extend beyond the local-character LSDA, it is intuitive to incorporate the spatial density variation, quantified by the gradient $|\nabla n^{\sigma}|$. Consequently, the XC energy is expressed as

$$E_{\mathrm{XC}}^{\mathrm{GGA}}[n^{\uparrow}(\mathbf{r}), n^{\downarrow}(\mathbf{r})] = \int \mathrm{d}\mathbf{r}\; n(\mathbf{r}) \epsilon_{\mathrm{XC}} \left(n^{\uparrow}, n^{\downarrow}, |\nabla n^{\uparrow}|, |\nabla n^{\downarrow}|, \ldots \right). \quad (2.37)$$

The function ϵ_{XC} is further divided into a product of the familiar exchange energy $\epsilon_{\mathrm{X}}^{\mathrm{hom}}(n)$ of the homogeneous electron gas and a dimensionless enhancement factor

$$F_{\mathrm{XC}} \left(n^{\uparrow}, n^{\downarrow}, |\nabla n^{\uparrow}|, |\nabla n^{\downarrow}|, \ldots \right) = F_{\mathrm{X}} + F_{\mathrm{C}}, \quad (2.38)$$

incorporating gradient dependence.

In this context, treating exchange is marginally more straightforward than addressing correlation. For the former, a spin-scaling relation proves useful. It reads

$$E_{\mathrm{X}}^{\mathrm{GGA}}[n^{\uparrow}(\mathbf{r}), n^{\downarrow}(\mathbf{r})] = \frac{1}{2} E_{\mathrm{X}}^{\mathrm{GGA}}[2n^{\uparrow}] + \frac{1}{2} E_{\mathrm{X}}^{\mathrm{GGA}}[2n^{\downarrow}]. \quad (2.39)$$

This means that for the exchange energy, we only need to consider the spin-unpolarized factor $F_{\mathrm{X}}(n, |\nabla n|)$. Besides, a dimensionless first-order reduced-density

gradient s is introduced:

$$s = \frac{|\nabla n|}{2k_{\mathrm{F}}n} = \frac{|\nabla r_s|}{2(2\pi/3)^{1/3}r_s}, \tag{2.40}$$

where $k_{\mathrm{F}} = 3(2\pi/3)^{1/3}r_s^{-1}$ denotes the Fermi wavenumber and r_s represents the average electron distance. This gradient informs us about the extent of spatial density change relative to the local Fermi wavelength $2\pi/k_{\mathrm{F}}$. The lowest-order terms of the enhancement factor F_{X} can be analytically computed, resulting in

$$F_{\mathrm{X}} = 1 + \frac{10}{81}s^2 + \dots. \tag{2.41}$$

Similarly, an expression for F_{C} can be derived as

$$F_{\mathrm{C}} = \frac{\epsilon_{\mathrm{C}}^{\mathrm{LDA}}(n)}{\epsilon_{\mathrm{X}}^{\mathrm{LDA}}(n)}(1 - 0.21951s^2 + \dots). \tag{2.42}$$

Notably, higher-order terms in the reduced-density gradient can also be employed. Depending on the physical conditions at the limit $s \to \infty$ and other parameters, numerous forms for the GGA functional are viable. We would like to give a brief overview of the Perdew, Burke, and Ernzerhof (PBE) parameterization [51], which is among the simplest.

In PBE, the enhancement factor F_{X} is chosen to satisfy $F_{\mathrm{X}}(0) = 1$, in line with LSDA, and $F_{\mathrm{X}} = \text{const.}$ for large arguments. It is formulated as

$$F_{\mathrm{X}}(s) = 1 + \kappa - \frac{\kappa}{1 + \frac{\mu s^2}{\kappa}}. \tag{2.43}$$

The parameters κ and μ are determined to fulfill the so-called Lieb-Oxford bound and recover the linear response form of the local density approximation for $s \to 0$. The correlation energy is then expressed in terms of the local correlation energy and an additive term H, leading to

$$E_{\mathrm{C}}^{\mathrm{PBE}}[n^{\uparrow}(\mathbf{r}), n^{\downarrow}(\mathbf{r})] = \int \mathrm{d}\mathbf{r}\, n(\mathbf{r}) \left(\epsilon_{\mathrm{C}}^{\mathrm{hom}}(r_s, \zeta) + H(r_s, \zeta, t)\right). \tag{2.44}$$

Here, $\zeta = (n^{\uparrow} - n^{\downarrow})/n$ denotes spin polarization, $r_s = \left(\frac{3}{4\pi n}\right)^{1/3}$ is the local Wigner-Seitz radius and t is a dimensionless density gradient proportional to $|\nabla n|$. The exact form of $H(r_s, \zeta, t)$ is elaborated in [51].

2.2.4 Plane-Wave Basis and Pseudopotentials

To solve the Kohn-Sham equations, an effective approach is required to describe the electronic wavefunctions in equation 2.30. One commonly used choice is the plane-wave ansatz, which leverages the crystal's cell-periodicity. This selection proves beneficial because plane waves can be efficiently handled using algorithms such as the Fast Fourier Transform, and they lend themselves to the accurate development of pseudopotentials, a concept we will explore later.

We express the wavefunction ψ_i for the i-th electron as an expansion over orthonormal plane waves:

$$\psi_i(\mathbf{r}) = \frac{1}{\sqrt{\Omega}} \sum_{\mathbf{q}} c_{i,\mathbf{q}} \mathrm{e}^{\mathrm{i}\mathbf{q}\mathbf{r}}, \tag{2.45}$$

where Ω denotes a volume used for normalization. Furthermore, the KS potential is expressed in terms of its Fourier components (a possibility for periodic quantities) which are

$$V_{\mathrm{KS}}(\mathbf{G}) = \frac{1}{\Omega_{\mathrm{cell}}} \int_{\Omega_{\mathrm{cell}}} \mathrm{d}\mathbf{r}\, V_{\mathrm{KS}}(\mathbf{r}) \mathrm{e}^{-\mathrm{i}\mathbf{G}\mathbf{r}}. \tag{2.46}$$

Here, Ω_{cell} is the volume of the primitive cell. This in turn yields

$$V_{\mathrm{KS}}(\mathbf{r}) = \sum_{n} V_{\mathrm{KS}}(\mathbf{G}_n) \mathrm{e}^{\mathrm{i}\mathbf{G}_n\mathbf{r}}. \tag{2.47}$$

The vectors $\mathbf{G}$ and $\mathbf{G}_n$ represent reciprocal lattice vectors. Now, we can calculate the matrix elements of the Kohn-Sham Hamiltonian in the plane-wave basis. Substituting this ansatz into the KS equation 2.30, multiplying by $1/\sqrt{\Omega}$, and integrating over the volume Ω leads to the KS equation in Fourier space which reads

$$\sum_{m'} H_{m,m'}(\mathbf{k}) c_{i,m'}(\mathbf{k}) = \epsilon_i(\mathbf{k}) c_{i,m}(\mathbf{k}). \tag{2.48}$$

To derive this equation, we introduced the relationships $\mathbf{q} = \mathbf{k} + \mathbf{G}_m$ and $\mathbf{q}' = \mathbf{k} + \mathbf{G}_{m'}$, where each eigenfunction for a specific $\mathbf{k}$-point is given by $\psi_{i,\mathbf{k}}(\mathbf{r}) = \frac{1}{\sqrt{\Omega}} \sum_m c_{i,m}(\mathbf{k}) \mathrm{e}^{\mathrm{i}(\mathbf{k}+\mathbf{G}_m)\mathbf{r}}$. The matrix elements of the Hamiltonian are described as follows:

$$H_{m,m'}(\mathbf{k}) = \frac{\hbar^2}{2m_{\mathrm{e}}} |\mathbf{k} + \mathbf{G}_m|^2 \delta_{m,m'} + V_{\mathrm{KS}}(\mathbf{G}_m - \mathbf{G}_{m'}). \tag{2.49}$$

This equation illustrates that the kinetic energy part of the expression can be used as a cutoff criterion for the plane-wave basis set. By adjusting this criterion, we are able to systematically improve the accuracy and the convergence of DFT calculations. To be precise, only plane waves with kinetic energies lower than a given threshold are considered, meaning that the condition

$$|\mathbf{k} + \mathbf{G}_m| < G_{\mathrm{cutoff}} \quad \text{with} \quad E_{\mathrm{cutoff}} = \frac{\hbar^2}{2m} G_{\mathrm{cutoff}}^2 \tag{2.50}$$

has to be fulfilled. Nonetheless, a drawback of the plane-wave basis is its demand for a large number of plane waves for tightly bound electrons. In solids (excluding metals) or molecules, chemical bonds form through electron transfer between atoms. For that reason, the wavefunctions representing valence electrons undergo significant changes upon bond formation. In contrast, wavefunctions of core electrons are considerably less affected. If we were to rigorously account for the entire electronic wavefunctions, we might require an extensive set of Fourier components, resulting in a high value for E_{cut}. Instead, we aim to eliminate the degrees of freedom associated

with core electrons in the computation. To achieve this, we introduce pseudopotentials.

A method that effectively addresses the division between strongly localized core electrons and more extensively delocalized valence electrons is orthogonalized plane waves (OPW). This approach also serves as a foundation for constructing pseudopotentials. The expression of electronic wavefunctions in the OPW framework is given by

$$\psi^{\mathrm{OPW}}(\mathbf{r}) = \frac{1}{\Omega}\left(\mathrm{e}^{\mathrm{i}\mathbf{q}\mathbf{r}} - \sum_j \langle u_j|\mathbf{q}\rangle\, u_j(\mathbf{r})\right), \tag{2.51}$$

with

$$\langle u_j|\mathbf{q}\rangle = \int \mathrm{d}\mathbf{r}\, u_j(\mathbf{r})\mathrm{e}^{\mathrm{i}\mathbf{q}\mathbf{r}}. \tag{2.52}$$

Here, the wavefunctions ψ^{OPW} are orthogonal to all (basically arbitrary) core functions u_j. They can be understood as comprising a localized component close to the nucleus (the right term in equation 2.51, where we let the sum $\sum_j$ pertain to the core contributions) and a smoother segment further away from the nucleus, formed by plane waves (the left term in equation 2.51). In this context, we refrain from exploring further details regarding the core functions $u_j(\mathbf{r})$, merely requiring them to be localized around the nucleus. Having this in mind, we can rewrite equation 2.51 as

$$\psi^{\mathrm{OPW,v}}(\mathbf{r}) = \tilde{\psi}^{\mathrm{OPW,v}}(\mathbf{r}) + \sum_j B_j u_j(\mathbf{r}). \tag{2.53}$$

Here, the superscript v indicates the computation of the valence electron wavefunction, with $\tilde{\psi}^{\mathrm{OPW,v}}$ representing the smoother part beyond the core region. The transformation B_j can be derived via a Fourier transform of the original OPWs.

Now, a pseudopotential represents the effective potential pertaining to the Schrödinger-like equation, which exclusively concerns the smooth valence electron wavefunction. Consequently, the corresponding equation reads

$$\left(-\frac{\hbar^2}{2m}\nabla^2 + V^{\mathrm{pseudo}}\right)\tilde{\psi}_i^{\mathrm{OPW,v}}(\mathbf{r}) = \epsilon_i^{\mathrm{v}}\tilde{\psi}_i^{\mathrm{OPW,v}}(\mathbf{r}). \tag{2.54}$$

The construction of pseudopotentials offers a variety of approaches. Assuming that the localized states u_j correspond to core orbitals ψ_j^{c}, an OPW-pseudopotential approach, as developed by Phillips, Kleinman, and Antoncik [52–54], introduces the following equation:

$$V^{\mathrm{pseudo}} = V + V^{\mathrm{R}}. \tag{2.55}$$

Here, V^{R} is a nonlocal operator that acts on the smooth valence wavefunction according to

$$V^{\mathrm{R}}\tilde{\psi}_i^{\mathrm{OPW,v}}(\mathbf{r}) = \sum_j (\epsilon_i^{\mathrm{v}} - \epsilon_i^{\mathrm{c}})\,\langle \psi_j^{\mathrm{OPW,c}}|\tilde{\psi}_i^{\mathrm{OPW,v}}\rangle\,\psi_j^{\mathrm{c}}(\mathbf{r}), \tag{2.56}$$

where $\psi_j^{\mathrm{OPW,c}}$ is the wavefunction concerning core electrons and $\epsilon_i^{\mathrm{v/c}}$ are the respective eigenvalues. Sophisticated pseudopotentials exist that surpass the ones just described, even without relying on the OPW concept. The sole criterion is that the pseudopotentials should yield the same valence band energies as the original potential.

Another relevant category of pseudopotentials is norm-conserving pseudopotentials. In general, the smooth pseudo wavefunctions $\tilde{\psi}^{\mathrm{OPW,v}}(\mathbf{r})$ are not inherently orthonormal. Hamann, Schlüter, and Chiang pioneered the introduction of norm-conserving pseudopotentials [55]. To be precise, they set the requirement that

$$\int_{|\mathbf{r}|<r_\mathrm{c}} \mathrm{d}\mathbf{r}\, |\psi^{\mathrm{PS}}|^2 = \int_{|\mathbf{r}|<r_\mathrm{c}} \mathrm{d}\mathbf{r}\, |\psi|^2. \tag{2.57}$$

This requires that within the sphere of radius r_c, the pseudo wavefunction ψ^{PS} and the actual wavefunction ψ should give the same normalization integral. Fig. 2.3 provides a schematic representation of a normalized and a non-normalized pseudo wavefunction, highlighting their differences.

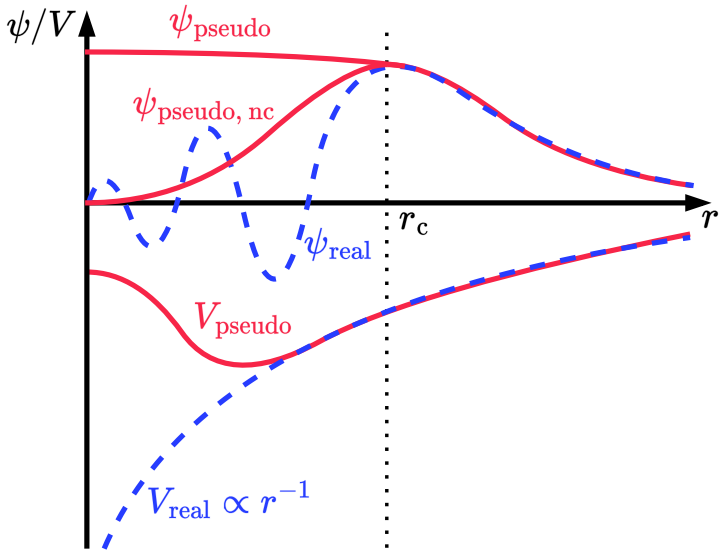

Figure 2.3: Sketch illustrating the principle of pseudopotentials. Both the non-normalized pseudo wavefunction ψ_{pseudo} and the normalized pseudo wavefunction $\psi_{\mathrm{pseudo,\,nc}}$, the latter generated by a norm-conserving pseudopotential, are identical with the real wavefunction ψ_{real} for $r \geq r_c$. This is also the case for the pseudopotential V_{pseudo} and real potential V_{real}.

In the OPW framework, we aim to obtain wavefunction smoothness by constraining the number of Fourier expansion terms used to calculate valence properties with a certain precision. Next to norm-conserving pseudopotentials, there exists an alternative concept known as ultrasoft pseudopotentials. These pseudopotentials require significantly fewer plane waves to achieve the desired precision. They are even smoother and demand less computation time. Yet, this advantage comes with

the trade-off of involving a generalized eigenvalue problem with an overlap matrix.

Lastly, we turn our attention to the method of projector augmented waves (PAWs) [56]. This approach enables us to restore pseudo wavefunctions for all electrons using potentials that are closely related to ultrasoft pseudopotentials, making possible the calculation of all-electron observables. To achieve this, we reframe the transformation from a smooth pseudo wavefunction $|\tilde{\psi}\rangle = \sum_m c_m |\tilde{\psi}_m\rangle$ to the real wavefunction $|\psi\rangle = \sum_m c_m |\psi\rangle_m$ (both expanded in partial waves) as

$$|\psi\rangle = \mathcal{T} |\tilde{\psi}\rangle . \tag{2.58}$$

When we demand linearity in the transformation $\mathcal{T}$, the expansion coefficients c_m can be found using projection operators $\tilde{p}_m$:

$$c_m = \langle \tilde{p}_m | \tilde{\psi} \rangle . \tag{2.59}$$

The key distinction from the previously discussed pseudopotentials is that the transformation $\mathcal{T}$ still encompasses the complete all-electron wavefunction and can be expressed as

$$\mathcal{T} = \mathbb{1} + \sum_m \left(|\psi_m\rangle - |\tilde{\psi}_m\rangle \right) \langle \tilde{p}_m | . \tag{2.60}$$

2.2.5 Van der Waals Corrections

Van der Waals forces, which encompass interactions between transient dipoles, hold particular relevance. The origin of these forces is rooted in the fluctuations of the charge density in atoms or molecules, yielding temporary dipole formations that interact. Unlike ionic or covalent bonds, van der Waals forces exhibit relatively low strength. Nevertheless, they show significant influence in the realm of HaPs [57–61] due to the substantial polarizability of halogens and organic molecules. A plethora of approaches exist for handling van der Waals forces in DFT. Among other noteworthy methods, the Tkatchenko-Scheffler (TS) model [62] will be discussed briefly.

The method's foundation revolves around parameter adjustment to adapt to the van der Waals forces, which customarily decrease with the sixth power of the distance between polarizable atoms or molecules. These parameters encompass polarizabilities, dispersion coefficients, and van der Waals radii, which aim to encapsulate the local electronic environment. The total energy is a simple summation that reads

$$E = E_{\mathrm{DFT}} + E_{\mathrm{TS}}, \tag{2.61}$$

comprising the energy from the DFT calculation (E_{DFT}) and the correction energy E_{TS}. This correction is defined as

$$E_{\mathrm{TS}} = -\frac{1}{2} \sum_{A,B} \frac{C_{6AB}}{R_{AB}^6} f_{\mathrm{damp}}(R_{AB}, R_{0A}, R_{0B}). \tag{2.62}$$

Here, R_{AB} represents the distance between atoms A and B, while R_{0A} and R_{0B} denote the respective van der Waals radii (more precisely, the van der Waals radius is half

the distance between two atoms where the London dispersion attraction balances the Pauli repulsion). Correcting the total energy like this has been demonstrated to notably enhance the accuracy of structural property predictions for materials characterized by substantial dispersive contributions [63, 64].

The unique aspect of the TS method lies in the dependence of the dipole-dipole dispersion C_{6AB} on the local charge density, thereby encapsulating the chemical environment. Additionally, the strength of C_{6AB} is computed as the harmonic mean of one-atom dispersion coefficients C_{6ii} for both atomic species, incorporating effective polarizabilities α_i. Herein, the parameters v_i represent effective atomic volumes, calculated using Hirshfeld partitioning of the all-electron density, which uses the spherically averaged electron density of the free atomic species. These parameters are derived based on the values associated with the unbound atomic species, as described by the following equations:

$$\alpha_i = v_i \, \alpha_i^{\text{free}}, \tag{2.63}$$

$$C_{6ii} = v_i^2 \, C_{6ii}^{\text{free}}, \tag{2.64}$$

$$R_{0i} = v_i^{\frac{1}{3}} \, R_{0i}^{\text{free}}. \tag{2.65}$$

The index i always refers to the atomic species A or B. To curtail the R^{-6} potentials at short range, the function f_{damp} is employed, adopting a Fermi-type damping function. The values of C_{6ii}^{free} are external parameters determined through methods like self-interaction corrected time-dependent DFT, as demonstrated by Ref. [65], or through experimental distributions of dipole oscillator strength.

2.3 The Tight Binding Model

In the introduction, we briefly mentioned that using DFT for large systems poses challenges. While there is no strict constraint on the number of atoms that can be investigated with DFT, practical limitations exist. In practice, DFT calculations can range from a few atoms to hundreds or even thousands of atoms, dependent on factors such as the specific system, computational resources, basis set size, method approximations, and parallelization capabilities. However, for our specific purposes of studying large supercells of hybrid HaPs containing tens of thousands of atoms, standard DFT, as delineated in the previous section, proves impractical. This is why we want to employ a TB model which is parameterized with the help of DFT.

2.3.1 General Derivation of the TB Model

In general, the TB model presents a semi-empirical framework that begins with the postulation that the wavefunction of an electron in a solid can be approximated as a linear combination of atomic wavefunctions localized around each atom constituting the crystal lattice. Frequently, these atomic wavefunctions are chosen to be atomic orbitals. In the context of the TB model, the electron's wavefunction is formulated as a summation over these atomic orbitals. The coefficients in this summation dictate

how much each atomic orbital contributes to the overall wavefunction. This modeling strategy finds its strongest justification when we regard electrons as strongly bound to their respective nuclei, experiencing minimal interaction with neighboring electrons or nuclei. Fig. 2.4 visually outlines this conceptual scenario.

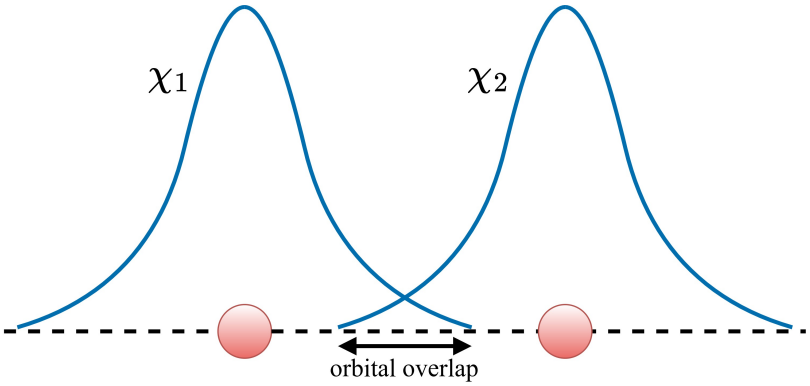

Figure 2.4: Schematic representation depicting localized, overlapping electron orbitals in the TB formalism. The black arrow highlights the overlap between the two orbital functions (drawn in blue) surrounding the two nuclei (drawn in red).

The TB model strongly connects with the linear combination of atomic orbitals (LCAO). We construct the total electronic wavefunction ψ_i in a crystal by summing over localized atomic orbitals using the following expression:

$$\psi_{i\mathbf{k}}(\mathbf{r}) = \sum_n \sum_{\mathbf{R}} e^{i\mathbf{k}\mathbf{R}} c_{i,n}(\mathbf{k}) \chi_n(\mathbf{r} - \mathbf{R} - \boldsymbol{\tau}_n), \tag{2.66}$$

Note that this expression can be normalized by adding a prefactor of $1/\sqrt{N_{\mathbf{R}}}$ (where $N_{\mathbf{R}}$ denotes the number of atomic sites involved), which we omit for simplicity. The coefficients $c_{i,n}(\mathbf{k})$ regulate the influence of each localized atomic orbital χ_n at the position $\mathbf{r}$, adjusted by a lattice translation vector $\mathbf{R}$ ($\mathbf{R} = n_1\mathbf{a}_1 + n_2\mathbf{a}_2 + n_3\mathbf{a}_3$ wit $\mathbf{a}_i$ denoting the primitive lattice vectors). The shift $\boldsymbol{\tau}_n$ denotes the position of the respective atom in a unit cell, accessible through the corresponding translation vector $\mathbf{R}$. The underlying concept of this approach draws upon the Bloch theorem, which asserts that the eigenfunctions of a periodic crystal can be represented as $\psi_{\mathbf{k}}(\mathbf{r}) = e^{i\mathbf{k}\mathbf{r}} u_{\mathbf{k}}(\mathbf{r})$, where $u_{\mathbf{k}}(\mathbf{r}) = u_{\mathbf{k}}(\mathbf{r} + \mathbf{R})$ indicates the periodic behavior of the function.

The TB model, a one-particle model employing the mean-field approximation, gives rise to a Hamiltonian formulated as

$$H = -\frac{\hbar}{2m_e}\nabla^2 + \underbrace{\sum_{\mathbf{R},n} V_n(|\mathbf{r} - \mathbf{R} - \boldsymbol{\tau}_n|)}_{V_{\text{eff}}(\mathbf{r})}. \tag{2.67}$$

In this equation, V_n represents the potential attributed to the corresponding atom. The eigenenergies of this Hamiltonian can be found in the TB basis utilizing the

customary quantum mechanical relation

$$\epsilon_i(\mathbf{k}) = \frac{\langle \chi_m | H | \Psi_i \rangle}{\langle \chi_m | \Psi_i \rangle}. \tag{2.68}$$

By substituting the respective wavefunction expressions, we arrive at the secular equation

$$\sum_n \left[H_{mn}(\mathbf{k}) - \epsilon_i(\mathbf{k}) S_{mn}(\mathbf{k}) \right] c_{i,n} = 0. \tag{2.69}$$

The corresponding Hamiltonian matrix element is given by

$$H_{mn}(\mathbf{k}) = \sum_{\mathbf{R}} \mathrm{e}^{\mathrm{i}\mathbf{k}\mathbf{R}} \int \mathrm{d}\mathbf{r}\, \chi_m^*(\mathbf{r} - \tau_m) H \chi_n(\mathbf{r} - \mathbf{R} - \tau_n), \tag{2.70}$$

which mirrors the overlap matrix

$$S_{mn}(\mathbf{k}) = \sum_{\mathbf{R}} \mathrm{e}^{\mathrm{i}\mathbf{k}\mathbf{R}} \int \mathrm{d}\mathbf{r}\, \chi_m^*(\mathbf{r} - \tau_m) \chi_n(\mathbf{r} - \mathbf{R} - \tau_n). \tag{2.71}$$

The rationale behind introducing the overlap matrix arises from the fact that atomic wavefunctions are not inherently orthogonal to one another. While the conventional TB formalism presumes orthogonality between atomic orbitals, there are scenarios where relaxing this assumption and considering non-orthogonal atomic orbitals yields a more precise description.

Nevertheless, it is feasible to establish an orthogonal basis from a non-orthogonal one, achieved through methods like the Löwdin scheme [66]. In this approach, a transformation matrix T is constructed, composed of eigenvectors associated with the eigenvalues of the overlap matrix. These eigenvectors form the Löwdin orbitals, constituting the new orthogonal basis set. By applying this transformation, an orthogonalized Hamiltonian matrix H' is obtained, given by $H'_{ij} = T^\dagger H_{ij} T$. The eigenvectors of H' correspond to the updated orthogonal wavefunctions. For the purpose of our discussion, however, we adopt the orthogonal TB scheme, where the overlap matrix $S_{mn}(\mathbf{k})$ is treated as the unity matrix I (For non-orthogonal TB, see, e.g., [67]).

In the matrix elements $H_{mn}(\mathbf{k})$, both the orbitals χ_{mn} and the potential V_n are position-dependent. They can be categorized into groups based on the number of atomic sites involved. For simplicity, we denote the localized orbitals as $|\chi_\alpha\rangle$ and the effective potential from the Hamiltonian as $V_{\mathrm{eff},\alpha}$, where the index α now belongs to a specific localized orbital at a particular atomic site. The diagonal matrix elements are then expressed as

$$\langle \chi_\alpha | H | \chi_\alpha \rangle = \underbrace{\langle \chi_\alpha | -\frac{\hbar}{2m_\mathrm{e}} \nabla^2 + V_{\mathrm{eff},\alpha} | \chi_\alpha \rangle}_{\text{one-center}} + \sum_{\gamma \neq \alpha} \underbrace{\langle \chi_\alpha | -\frac{\hbar}{2m_\mathrm{e}} \nabla^2 + V_{\mathrm{eff},\gamma} | \chi_\alpha \rangle}_{\text{two-center crystal field}}. \tag{2.72}$$

Meanwhile, the off-diagonal elements read

$$\langle \chi_\alpha | H | \chi_\beta \rangle = \underbrace{\langle \chi_\alpha | -\frac{\hbar}{2m_\mathrm{e}} \nabla^2 + V_{\mathrm{eff},\alpha} + V_{\mathrm{eff},\beta} | \chi_\beta \rangle}_{\text{two-center electron hopping}} + \sum_{\gamma \neq \alpha,\beta} \underbrace{\langle \chi_\alpha | -\frac{\hbar}{2m_\mathrm{e}} \nabla^2 + V_{\mathrm{eff},\gamma} | \chi_\beta \rangle}_{\text{three center}}. \tag{2.73}$$

We can interpret the different terms as follows:

- One-center matrix elements describe the interactions when both orbitals and the potential are centered at the same site. They encapsulate the onsite energy and hold a critical role in determining the diagonal elements of the Hamiltonian matrix.
- Two-center matrix elements (from equation 2.73) depict interactions when the orbitals are centered on different sites and the potential is located at one of these two sites. They form the off-diagonal elements of the Hamiltonian matrix and account for the electron transfer between distinct atomic sites. Additionally, there is a particular case of two-center matrix elements (as in equation 2.72): Those are influenced by the crystal symmetry and can be seen as an addition to the one-center terms.
- Three-center matrix elements represent the overlap and electron transfer where the two orbitals and the potential are located on three different atomic sites. They account for more complex bonding situations, such as in molecular systems with multiple neighboring atoms. The three-center matrix elements capture the spatial and electronic delocalization effects in these systems.

2.3.2 The Two-Center Approximation

Most TB models typically omit three-center integrals and the two-center crystal field correction, employing what is commonly referred to as the two-center approximation. This approach, initially developed by Slater and Koster [68], constitutes a semiempirical method frequently employed in TB calculations. The remaining matrix elements are denoted as onsite and overlap terms, corresponding to the one-center and two-center terms, respectively. Also, often only the overlap integral between nearest-neighbor atomic orbitals is considered. The TB matrix elements are frequently fitted to experimental or theoretical data, while the interaction between the atomic-like basis functions retains the same symmetry observed between two atoms in free space. For that reason, we can redefine the orbital basis functions as

$$\chi_i(\mathbf{r}) \to \chi_{nlm}(\mathbf{r}) = \chi_{nl}(r) Y_l^m(\mathbf{r}). \tag{2.74}$$

Here, the principal, the angular momentum, and the magnetic quantum numbers are denoted as n, l, and m, respectively. In certain cases, we can replace the spherical harmonics Y_l^m with real spherical harmonics Y_{lm}, which proves advantageous for practical calculations and visualization purposes. The calculation of these real spherical harmonics follows the expressions

$$Y_{lm} = \frac{1}{\mathrm{i}\sqrt{2}} \left((-1)^m Y_l^{-m} - Y_l^m \right) \quad \text{for} \quad m < 0, \tag{2.75}$$

$$Y_{lm} = Y_l^m \quad \text{for} \quad m = 0, \tag{2.76}$$

$$Y_{lm} = \frac{1}{\sqrt{2}} \left((-1)^m Y_l^m + Y_l^{-m} \right) \quad \text{for} \quad m > 0. \tag{2.77}$$

Regarding the overlap matrix element, the quantum number n is irrelevant. We write the overlap between states lm and $l'm'$ as $t_{lml'm'}$. However, these matrix elements are

diagonal in the mm' indices, which means that $t_{lml'm'} = t_{ll'm}\delta_{mm'}$. To facilitate a more intuitive notation, we adhere to the customary conventions of denoting the states ll' as s, p, d, etc., orbitals and representing $m = 0, \pm1, \pm2, \ldots$ as σ, π, δ, etc. This leads to a notation of $t_{ss\sigma}, t_{sp\sigma}, t_{pp\pi}, \ldots$ for the different overlap matrix elements. Fig. 2.5 shows a schematic overview of a selection of overlap integrals visualized with the help of real spherical harmonics.

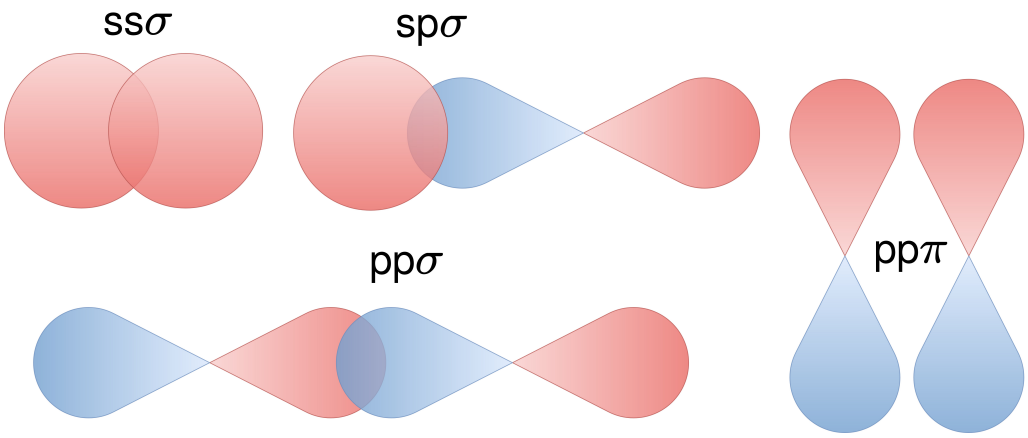

Figure 2.5: Sketch visualizing selected kinds of orbital overlaps. The orbital phases are depicted with blue and red color.

As mentioned earlier, the matrix elements of most semiempirical TB models for specific materials are adjusted based on theoretical data or experimental observations. Slater and Koster provided numerous parameters for matrix elements with the symmetries of s, p, or d states, along with analytic formulas [68]. Nonetheless, there is no universal recipe for deriving TB parameters, as it hinges on the desired quantities to be computed and the complexity of the material under investigation.

Furthermore, for constructing a multi-scale TB model, the symmetry axes of orbitals may not align perfectly, as depicted in Fig. 2.5. Yet, when we rotate a real spherical harmonic, it always results in a linear combination of real spherical harmonics with the same value of l but different values of m. This property enables us to consistently express orbitals as linear combinations aligned with the dimer axis. Another approach to consider overlap matrix elements with a non-aligned dimer axis is to statistically average over numerous configurations and angles. By incorporating a wide range of different orientations, we can account for the variations in alignment and obtain a more comprehensive understanding of the system, which will be discussed in Chapter 3.

Last but not least, writing the one-particle TB Hamiltonian in second quantization is both convenient and straightforward. This is accomplished through the expression

$$H = \sum_{ij} \langle i|H|j\rangle \, c_i^\dagger c_j. \tag{2.78}$$

Here, the states $\{i, j\}$ correspond to TB wavefunctions, while $c_i^\dagger$ and c_j represent the respective electronic creation and annihilation operators. This relationship can be

proven by Fourier transforming the operators according to

$$c_i = \sum_{\mathbf{k}} e^{i\mathbf{k}\mathbf{r}_i} c_{i,\mathbf{k}}, \quad c_i^\dagger = \sum_{\mathbf{k}} e^{i\mathbf{k}\mathbf{r}_i} c_{i,\mathbf{k}}. \tag{2.79}$$

Considering a TB wavefunction as $|\psi_{\mathbf{k}}\rangle = (c_{\mathbf{k}}^1, c_{\mathbf{k}}^2, \ldots, c_{\mathbf{k}}^n)$, it directly follows that

$$\sum_{ij} \langle i|H|j\rangle \, c_i^\dagger c_j = \sum_{\mathbf{k}} \langle \psi_{i,\mathbf{k}}|H|\psi_{i,\mathbf{k}}\rangle \, . \tag{2.80}$$

By separating the summation into one part encompassing diagonal matrix elements and another involving off-diagonal elements only for nearest-neighbor interactions, we can rewrite this as

$$H = \sum_i \epsilon_i c_i^\dagger c_i + \sum_{<i,j>} t_{ij} c_i^\dagger c_j. \tag{2.81}$$

In this equation, ϵ_i represents onsite energies, and t_{ij} signifies the overlap energies.

2.3.3 Application of TB to Graphene and Zincblende Structures

To illustrate the power and functionality of TB, we utilize it in a straightforward textbook example featuring graphene, a material that is both simple and very intriguing. Graphene is a two-dimensional sheet of carbon atoms arranged in a hexagonal lattice. It is one of the thinnest, strongest, and most conductive materials known to date [69]. Its remarkable properties make it fascinating for various applications, such as electronics, energy storage, sensors, and even biomedical devices [69–71]. Graphene's high electrical and thermal conductivity, exceptional mechanical strength, and flexibility open up possibilities for advancements in numerous fields, making it a highly intriguing material for scientific research and technological innovation [69]. The lattice of one graphene monolayer is shown in Fig. 2.6.

It comprises two sublattices with carbon atoms C_1 and C_2. The two primitive lattice vectors for each sublattice are

$$\mathbf{a}_1 = \frac{a}{2}(\sqrt{3}, 1) \quad \text{and} \quad \mathbf{a}_2 = \frac{a}{2}(\sqrt{3}, -1), \tag{2.82}$$

and the nearest-neighbor vectors

$$\boldsymbol{\delta}_1 = \left(\frac{a}{\sqrt{3}}, 0\right), \quad \boldsymbol{\delta}_2 = \left(-\frac{a}{2\sqrt{3}}, -\frac{a}{2}\right), \quad \boldsymbol{\delta}_3 = \left(-\frac{a}{2\sqrt{3}}, \frac{a}{2}\right). \tag{2.83}$$

The electronic configuration of each carbon atom in graphene is represented as $1s^2 2s^2 2p^2$. The bond between two carbon atoms, C_1 and C_2, is formed by an in-plane σ bond, created by the hybridization of sp^2 orbitals (2s, $2p_x$, and $2p_y$). Additionally, there exists an out-of-plane π bond involving the $2p_z$ orbitals, which are oriented perpendicular to the planar structure. In a monolayer of graphene, the conduction and valence bands possess zero band gap due to the half-filled π band, allowing for the free movement of electrons. Moreover, the π bonds facilitate a weak van der Waals interaction between adjacent graphene layers.

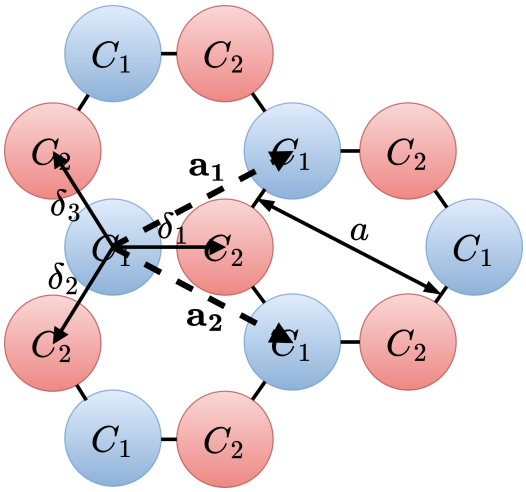

Figure 2.6: Sketch visualizing the structure of a graphene layer. The structure with blue circles forms the first sublattice (A), and the one with red circles the second sublattice (B). The vectors $\mathbf{a}_{1,2}$ are the unit vectors and $\boldsymbol{\delta}_{1,2,3}$ the nearest-neighbor vectors. The lattice constant is denoted as a.

Using the orbitals we have just introduced, we construct a TB electronic wavefunction that reads

$$\begin{aligned}\psi_{\mathbf{k}}(\mathbf{r}) &= \frac{1}{\sqrt{N}}\sum_{ij}^{N}\left[\mathrm{e}^{\mathrm{i}\mathbf{k}\mathbf{R}_{A,i}}c_A\phi_A(\mathbf{r}-\mathbf{R}_{A,i}) + \mathrm{e}^{\mathrm{i}\mathbf{k}\mathbf{R}_{B,j}}c_B\phi_B(\mathbf{r}-\mathbf{R}_{B,j})\right] \\ &= c_A\psi_A(\mathbf{r}) + c_B\psi_B(\mathbf{r}).\end{aligned} \tag{2.84}$$

Here, the sublattices are denoted as A and B, each with their respective p_z orbitals ϕ_A and ϕ_B. The TB matrix elements are calculated as

$$\begin{aligned}\langle\psi_A|H_{\mathrm{TB}}|\psi_B\rangle &= \frac{1}{N}\sum_{ij}^{N}\mathrm{e}^{\mathrm{i}\mathbf{k}(\mathbf{R}_{B,j}-\mathbf{R}_{A,i})}\underbrace{\langle\phi_A|H_{\mathrm{TB}}|\phi_B\rangle}_{=:-t} \\ &\approx -t\sum_{l=1}^{3}\mathrm{e}^{\mathrm{i}\mathbf{k}\boldsymbol{\delta}_l} =: -tf(\mathbf{k}) \quad \text{with} \quad \mathbf{R}_B = \mathbf{R}_A + \boldsymbol{\delta}_l.\end{aligned} \tag{2.85}$$

The simplification from the first to the second line assumes only nearest-neighbor hopping. Similar calculations are carried out for the other matrix elements (with $\langle\phi_{A,B}|H_{\mathrm{TB}}|\phi_{A,B}\rangle =: \epsilon$), leading to a secular equation that is solvable only if

$$\begin{vmatrix}\epsilon - E(\mathbf{k}) & -tf(\mathbf{k}) - E(\mathbf{k})V\cdot f(\mathbf{k}) \\ -tf^*(\mathbf{k}) - E(\mathbf{k})V\cdot f^*(\mathbf{k}) & \epsilon - E(\mathbf{k})\end{vmatrix} = 0, \tag{2.86}$$

where V is a zero parameter if the p_z orbitals are presumed to be orthogonal to each other. From this condition, we calculate

$$E(\mathbf{k}) = \frac{\epsilon \pm t\sqrt{|f(\mathbf{k})|^2|}}{1 \pm V\sqrt{|f(\mathbf{k})|^2|}}. \tag{2.87}$$

The corresponding bands and the density of states (DOS) are shown in Fig. 2.7.

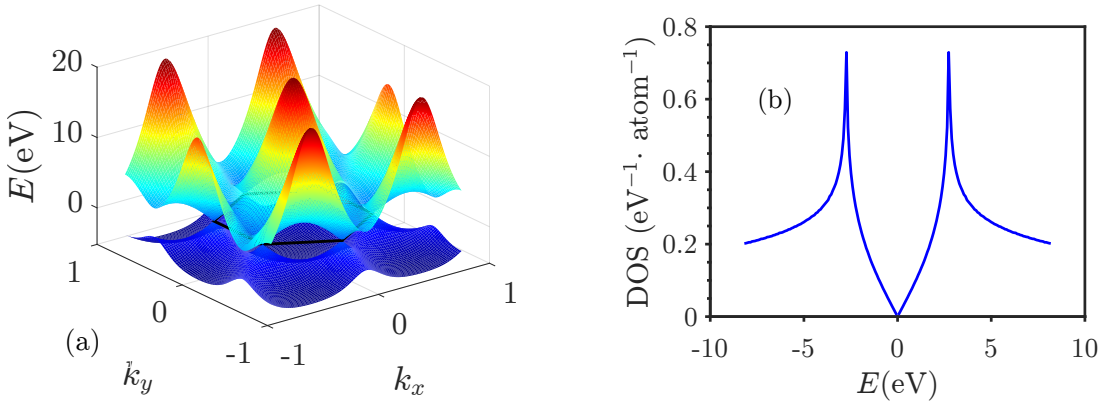

Figure 2.7: Electronic band structure (panel a) and DOS (panel b) for graphene, calculated with TB.

The TB model can also be extended to other, slightly more complicated materials like diamond and zincblende crystals such as C, Si, Ge, GaAs, and ZnSe, which are still straightforward textbook examples. In these materials, each atom is tetrahedrally surrounded by other atoms. They possess a crystal structure with a face-centered cubic Bravais lattice and two atoms in the basis. The respective TB parameters are provided by Ref. [72] and account for all possible nearest-neighbor interactions.

In the context of diamond, a crystal lattice composed of carbon atoms, a proper TB model accounts for the interactions between the valence electrons of each carbon atom and those of its neighboring carbon atoms. The carbon-carbon bonding is described using sp^3 hybrid orbitals. These hybrid orbitals result from combining one 2*s* orbital and three 2p orbitals. The overlap of these hybrid orbitals leads to the formation of robust covalent bonds, which gives rise to a wide band gap and makes diamond an insulating material.

In a compound semiconductor such as GaAs, there are two different types of atoms that form a face-centered cubic lattice. The TB model considers the interaction between valence electrons of neighboring atoms, taking into account specific orbitals. In the case of GaAs, the bonding occurs through hybridizing the Ga 4s, and 4p orbitals with the As 4s, and 4p orbitals. This hybridization leads to the formation of covalent bonds, resulting in a direct band gap semiconductor. The respective TB parameters for all these materials are again provided by Ref. [72] and represent all possible nearest-neighbor interactions. For this case, we can calculate again the electronic structure and the density of states, which are shown in Fig. 2.8.

Until now, we have not considered the effect of SOC in TB. However, for certain materials like hybrid HaPs, it becomes essential to incorporate SOC into the model.

2.3.4 Spin-Orbit Coupling in the TB Model

To incorporate the effects of SOC in the TB model, we can employ Equation 2.35. However, in our specific context, we can further simplify the expression. In real solids,

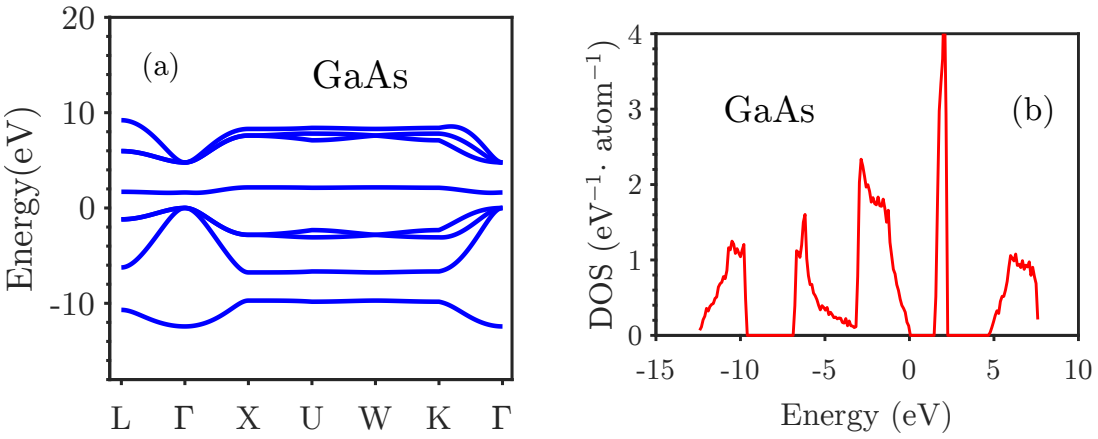

Figure 2.8: Electronic band structure (panel a) and DOS (panel b) for GaAs, calculated with TB.

the most significant SOC interaction occurs near the nucleus, where the gradient ∇V is most pronounced. This interaction can be effectively treated in an atom-like spherical geometry. That allows us to approximate the gradient as $\nabla V = \hat{\mathbf{r}} \mathrm{d}V/\mathrm{d}r$, resulting in a simplified form of Equation 2.35 that reads

$$H_{\mathrm{SOC}} = \frac{e\hbar}{4m^2c^2r}\frac{\mathrm{d}V}{\mathrm{d}r}\mathbf{L}\cdot\boldsymbol{\sigma} =: \alpha\mathbf{L}\cdot\boldsymbol{\sigma}. \tag{2.88}$$

Here, we have combined the prefactor into a parameter α, and the angular momentum operator is denoted as $\mathbf{L} = \mathbf{r} \times \mathbf{p}$. To simplify further, we introduce ladder operators

$$L_\pm = L_x \pm \mathrm{i}L_y \quad \text{and} \tag{2.89}$$
$$\sigma_\pm = \sigma_x \pm \mathrm{i}\sigma_y. \tag{2.90}$$

Using these operators, we can express Equation 2.88 as

$$H_{\mathrm{SOC}} = \frac{\alpha}{2}(L_+\sigma_- + L_-\sigma_+ + L_z\sigma_z). \tag{2.91}$$

Additionally, we can exploit that s orbitals do not exhibit spin-orbit interaction owing to their spherical symmetry and lack of orbital angular momentum. This is evident when considering the total angular momentum j, which combines orbital angular momentum l and spin angular momentum s. In the case of an s orbital, with $l = 0$ and $s = \frac{1}{2}$, we have $j = \frac{1}{2}$, resulting in no splitting of the degenerate s orbitals. In contrast, p orbitals experience spin-orbit interaction arising from the combination of $l = 1$ and $s = \frac{1}{2}$, leading to $j = \frac{1}{2}, \frac{3}{2}$. This energy difference results in a splitting of the p orbital states due to SOC. Consequently, s orbitals do not show SOC, whereas non-spherical orbitals like p, d, or f orbitals exhibit coupling between spin and orbital angular momentum.

In our context, the objective is to evaluate the Hamiltonian from Equation 2.91 in the basis of p orbitals and spin, represented as

$$\{|p_x,\uparrow\rangle, |p_x,\downarrow\rangle, |p_y,\uparrow\rangle, |p_y,\downarrow\rangle, |p_z,\uparrow\rangle, |p_z,\downarrow\rangle\}. \tag{2.92}$$

Furthermore, we can express p orbitals in terms of spherical harmonics as

$$p_x = \frac{1}{\sqrt{2}}(Y_{1,-1} - Y_{1,1}) \quad \rightarrow \quad |p_x\rangle = \frac{1}{\sqrt{2}}(|1,-1\rangle - |1,1\rangle), \tag{2.93}$$

$$p_y = \frac{\mathrm{i}}{\sqrt{2}}(Y_{1,-1} + Y_{1,1}) \quad \rightarrow \quad |p_y\rangle = \frac{\mathrm{i}}{\sqrt{2}}(|1,-1\rangle + |1,1\rangle), \tag{2.94}$$

$$p_z = Y_{1,0} \rightarrow |p_z\rangle = |1,0\rangle\,. \tag{2.95}$$

The actions of the angular momentum operators on Y_{lm} are given by

$$L_\pm Y_{lm} = \sqrt{(l \mp m)(+ \pm m + 1)}\, Y_{l,m\pm1}, \tag{2.96}$$

$$L_z Y_{lm} = m Y_{lm}. \tag{2.97}$$

Similarly, for spin operators, we have

$$\sigma_+ |\uparrow\rangle = 0, \quad \sigma_+ |\downarrow\rangle = |\uparrow\rangle\,, \quad \sigma_- |\uparrow\rangle = |\downarrow\rangle\,, \tag{2.98}$$

$$\sigma_- |\downarrow\rangle = 0, \quad \sigma_z |\uparrow\rangle = |\uparrow\rangle\,, \quad \sigma_z |\downarrow\rangle = -|\downarrow\rangle\,. \tag{2.99}$$

Using these actions, we deduce the action of angular momentum operators on the corresponding p orbitals:

$$L_+ |p_x\rangle = |p_z\rangle\,, \quad L_+ |p_y\rangle = \mathrm{i}\,|p_z\rangle\,, \quad L_+ |p_z\rangle = -|p_x\rangle - \mathrm{i}\,|p_y\rangle\,, \tag{2.100}$$

$$L_- |p_x\rangle = -|p_z\rangle\,, \quad L_- |p_y\rangle = \mathrm{i}\,|p_z\rangle\,, \quad L_- |p_z\rangle = |p_x\rangle - \mathrm{i}\,|p_y\rangle\,, \tag{2.101}$$

$$L_z |p_x\rangle = \mathrm{i}\,|p_y\rangle\,, \quad L_z |p_y\rangle = -\mathrm{i}\,|p_x\rangle\,, \quad L_z |p_z\rangle = 0. \tag{2.102}$$

This approach allows us to calculate all the matrix elements of H_{SOC}. To illustrate, we calculate

$$\begin{aligned}
\langle p_y,\uparrow| H_{\mathrm{SOC}} |p_z,\downarrow\rangle &= \langle p_y,\uparrow| \frac{\alpha}{2}(L_+\sigma_- + L_-\sigma_+ + L_z\sigma_z) |p_z,\downarrow\rangle \\
&= \langle p_y,\uparrow| \frac{\alpha}{2} L_+\sigma_- |p_z,\downarrow\rangle + \langle p_y,\uparrow| \frac{\alpha}{2} L_-\sigma_+ |p_z,\downarrow\rangle + \langle p_y,\uparrow| \frac{\alpha}{2} L_z\sigma_z |p_z,\downarrow\rangle \\
&= \langle p_y,\uparrow| \frac{\alpha}{2} L_-\sigma_+ |p_z,\downarrow\rangle = \langle p_y,\uparrow| \frac{\alpha}{2} \left[L_- |p_z\rangle\right] \left[\sigma_+ |\downarrow\rangle\right] \\
&= \frac{\alpha}{2} \langle p_y,\uparrow| \left[|p_x,\uparrow\rangle - \mathrm{i}\,|p_y,\uparrow\rangle\right] = -\mathrm{i}\frac{\alpha}{2} \langle p_y,\uparrow |p_y,\uparrow\rangle =: -\mathrm{i}\gamma.
\end{aligned} \tag{2.103}$$

Here, we have grouped $\alpha/2$ into the parameter γ and utilized the orthogonality of both p orbital and spin states. We can similarly evaluate the remaining matrix elements, resulting in the matrix representation

$$H_{\mathrm{SOC}} = \gamma \cdot \begin{array}{c} \\ p_x,\uparrow \\ p_x,\downarrow \\ p_y,\uparrow \\ p_y,\downarrow \\ p_z,\uparrow \\ p_z,\downarrow \end{array} \begin{array}{c} \begin{array}{cccccc} p_x,\uparrow & p_x,\downarrow & p_y,\uparrow & p_y,\downarrow & p_z,\uparrow & p_z,\downarrow \end{array} \\ \begin{pmatrix} 0 & 0 & -\mathrm{i} & 0 & 0 & 1 \\ 0 & 0 & 0 & \mathrm{i} & -1 & 0 \\ \mathrm{i} & 0 & 0 & 0 & 0 & -\mathrm{i} \\ 0 & -\mathrm{i} & 0 & 0 & -\mathrm{i} & 0 \\ 0 & -1 & 0 & \mathrm{i} & 0 & 0 \\ 1 & 0 & \mathrm{i} & 0 & 0 & 0 \end{pmatrix} \end{array}. \tag{2.104}$$

Of course, the parameter γ needs to be parameterized according to the specific material under investigation.

2.4 The Ewald Summation

The onsite energies in the TB model can be approximated by the electrostatic interactions among atoms in a crystal. Yet, this involves a two-particle summation and can become computationally demanding for systems comprising a large number of atoms.

To address this challenge, a practical solution is offered by the Ewald summation method. This technique finds application in computational chemistry and physics to calculate electrostatic interactions between charged particles in a periodic system. Physicist Paul Ewald originally formulated it in 1921 [73]. The core concept underlying the Ewald summation revolves around dividing the overall electrostatic potential into two distinct components: a real-space and a reciprocal-space component. The real-space component tackles short-range interactions and can be computed directly, while the reciprocal-space component handles long-range interactions and is assessed in Fourier space.

To be precise, the contribution from real space is evaluated by summing interactions among charged particles within a specific cutoff distance plus an inversely charged Gaussian distribution. On the other hand, the reciprocal-space component is determined by translating the Gaussian charges into reciprocal space using a Fourier transform which enables the utilization of the Poisson equation to compute the electrostatic potential in reciprocal space. Subsequently, the reciprocal-space potential is converted back into real space through an inverse Fourier transform. This fundamental principle of the Ewald summation is visually represented in Fig. 2.9.

To express these considerations mathematically, we start with the potential field generated by ions residing in a periodic lattice. This potential field is given by

$$\phi(\mathbf{r}) = \sum_{\mathbf{R}} \sum_{j} \int \mathrm{d}\mathbf{r}' \frac{\rho_j(\mathbf{r}')}{|\mathbf{r} - \mathbf{r}' - \mathbf{R}|}, \tag{2.105}$$

Here, ρ_j represents the charge distribution of the j-th particle, and the summation $\sum_{\mathbf{R}}$ encompasses the lattice translation vectors. Correspondingly, the potential attributed to a single particle can be expressed as

$$\phi_i(\mathbf{r}) = \int \mathrm{d}\mathbf{r}' \frac{\rho_i(\mathbf{r}')}{|\mathbf{r} - \mathbf{r}'|}. \tag{2.106}$$

Additionally, we introduce the potential denoted as $\phi_{[i]}(\mathbf{r})$, which resembles $\phi(\mathbf{r})$, excluding the term where $i = j$ in the summation over j if $\mathbf{R} = 0$, indicated as $\sum_j'$. To proceed, we divide the potential of each particle into two components by introducing an additive term of zero. These components are defined as:

$$\phi_i(\mathbf{r}) = \phi_i^{\mathrm{S}}(\mathbf{r}) + \phi_i^{\mathrm{L}}(\mathbf{r}) \quad \text{with} \tag{2.107}$$

$$\phi_i^{\mathrm{S}}(\mathbf{r}) = \frac{q_i}{4\pi\epsilon_0} \int \mathrm{d}\mathbf{r}' \frac{\delta(\mathbf{r} - \mathbf{r}') - G(\mathbf{r} - \mathbf{r}')}{|\mathbf{r} - \mathbf{r}'|}, \tag{2.108}$$

$$\phi_i^{\mathrm{L}}(\mathbf{r}) = \frac{q_i}{4\pi\epsilon_0} \int \mathrm{d}\mathbf{r}' \frac{G(\mathbf{r} - \mathbf{r}')}{|\mathbf{r} - \mathbf{r}'|}. \tag{2.109}$$

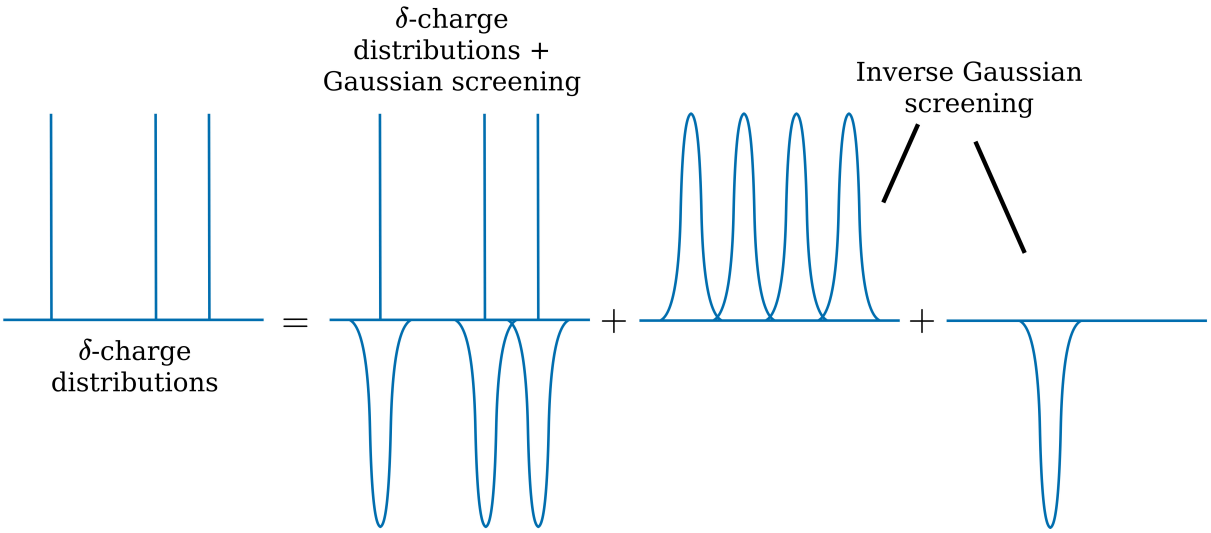

Figure 2.9: Sketch visualizing the principle of the Ewald summation. Computing the electrostatic potential for periodic charges (left-hand side of the equation) is slow but can be divided into three terms: The first term on the right-hand side of the equation exhibits rapid convergence in real space due to the local charge neutrality of the distribution. In the case of the second term, the Poisson equation can be solved in Fourier space, resulting in a Fourier series for the potential that converges quickly. Finally, the third term corresponds to the self-interaction term, which can be directly calculated.

In these equations, $G(\mathbf{r})$ represents a Gaussian distribution characterized by the standard deviation σ. This division permits the interaction energy to be decomposed into short-range (index S), long-range (index L), and self-interaction terms, manifested as

$$E = \underbrace{\frac{1}{2}\sum_i q_i \phi^{\mathrm{S}}_{[i]}(\mathbf{r}_i)}_{E^{\mathrm{S}}} + \underbrace{\frac{1}{2}\sum_i q_i \phi^{\mathrm{L}}(\mathbf{r}_i)}_{E^{\mathrm{L}}} - \underbrace{\frac{1}{2}\sum_i q_i \phi^{\mathrm{L}}_i(\mathbf{r}_i)}_{E^{\mathrm{self}}}. \tag{2.110}$$

By solving the Poisson equation, we can determine the potential generated by the Gaussian distribution. In addition, the self-interaction term can be directly evaluated. The utilization of the Fourier transform

$$\tilde{\phi}^{\mathrm{L}}(\mathbf{k}) = \int_V \mathrm{d}\mathbf{r}\, \phi^{\mathrm{L}}(\mathbf{r}) \mathrm{e}^{-\mathrm{i}\mathbf{k}\mathbf{r}}, \quad \phi^{\mathrm{L}}(\mathbf{r}) = \frac{1}{V}\sum_{\mathbf{k}} \tilde{\phi}^{\mathrm{L}}(\mathbf{k}) \mathrm{e}^{\mathrm{i}\mathbf{k}\mathbf{r}} \tag{2.111}$$

helps us solve the Poisson equation in reciprocal space so that the final expression for the interaction energy reads

$$\begin{aligned} E = &\frac{1}{2}\sum_{\mathbf{R}}\sum_i{\sum_j}' \frac{q_i q_j}{|\mathbf{r}_i - \mathbf{r}_j - \mathbf{R}|}\left(1 - \mathrm{erf}\left(\frac{|\mathbf{r}_i - \mathbf{r}_j - \mathbf{R}|}{\sqrt{2}\sigma}\right)\right) \\ &+ \frac{1}{2V\epsilon_0}\sum_{\mathbf{k}\neq 0} \frac{\mathrm{e}^{-\sigma^2 k^2/2}}{k^2}|S(\mathbf{k})|^2 + \frac{1}{\sqrt{2\pi}\sigma}\sum_i q_i^2. \end{aligned} \tag{2.112}$$

In this context, $\mathrm{erf}(z)$ signifies the Gaussian error function and S is a phase-like geometry factor which reads

$$S(\mathbf{k}) = \sum_i \sum_j q_i q_j \mathrm{e}^{\mathrm{i}\mathbf{k}(\mathbf{r}_i - \mathbf{r}_j)}. \tag{2.113}$$

Notably, as $\lim_{z\to\infty} \mathrm{erf}(z) = 1$, the first term E^{S} is effectively truncated for high distances, rendering it short-ranged in real space. Similarly, the truncation imposed by $\mathrm{e}^{-\sigma^2 k^2/2}$ in the second term E^{L} results in a short-ranged nature in reciprocal space.

Different variations of this formula, with slight parameter variations, exist. The version we employ for potential calculations and the respective parameters [5] are given by

$$\phi = \frac{1}{2} \sum_{i\neq j} \frac{q_i q_j (1 - \mathrm{erf}(\alpha r_{ij}))}{r_{ij}} + \sum_{\mathbf{k}\neq 0} \frac{\pi}{2k^2} |S(\mathbf{k})|^2 \, \mathrm{e}^{-\pi^2 k^2/\alpha^2} - \frac{\pi}{2\alpha^2} \sum_i q_i^2. \tag{2.114}$$

Here, the expression r_{ij} encompasses the distances modified by the lattice translations. For validation purposes, we consider a scenario involving uniformly spaced point charges in a 3D grid, accompanied by a uniformly charged sphere in the background, to ensure charge neutrality. This configuration is illustrated in Fig. 2.10. For the following test calculation, we omit units for simplicity.

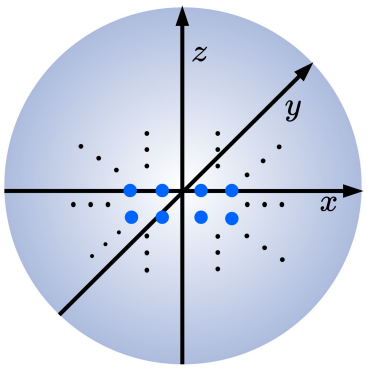

Figure 2.10: Sketch of a test system for the Ewald summation. The blue dots are point charges which are uniformly spaced in a sphere of constant charge distribution.

We assume each point charge possesses a charge of 1. When adopting a distance of 50 between point charges and a sphere radius of 400, the potential calculated through the Ewald summation yields approximately -0.40097, whereas the direct summation results in -0.40066. These values are almost identical. Still, the decisive distinction lies in the efficiency of the Ewald summation method. Our test is implemented in C++ and executed on an HP EliteBook 840 G4 Notebook with an Intel i5 7th Gen 2.5 GHz processor. While the Ewald summation produces that result almost instantly (about 55 microseconds), direct summation demands around 8.2 seconds. This discrepancy in execution time underscores the remarkable efficiency of the Ewald summation technique and renders it a well-applicable method for calculating onsite energies in the context of TB.

2.5 Wannier Functions

Wannier functions constitute a set of localized wavefunctions and serve as a very effective tool for studying the properties of crystalline materials. Named after Gregory Wannier, who pioneered their conception in 1937 [74], these functions furnish an alternative depiction of a solid's electronic states, contrasting with the more conventional Bloch functions. While the Bloch wavefunctions $\psi_{n\mathbf{k}} = e^{i\mathbf{kr}}u_{n\mathbf{k}}$ are the eigenstates of the Hamiltonian for the n-th band and a given wave vector $\mathbf{k}$, they are oscillating and delocalized in real space. However, in the context of the TB model, atomic orbitals are assumed to be localized in real space. Wannier functions address this assumption. Essentially, they are constructed through a superposition of the Bloch functions, and their calculation involves conducting a Fourier transform. Unlike Bloch functions, Wannier functions do not constitute eigenstates of the Hamiltonian and, therefore, exchange reciprocal space and energy localization for spatial localization. This difference is illustrated schematically in Fig. 2.11.

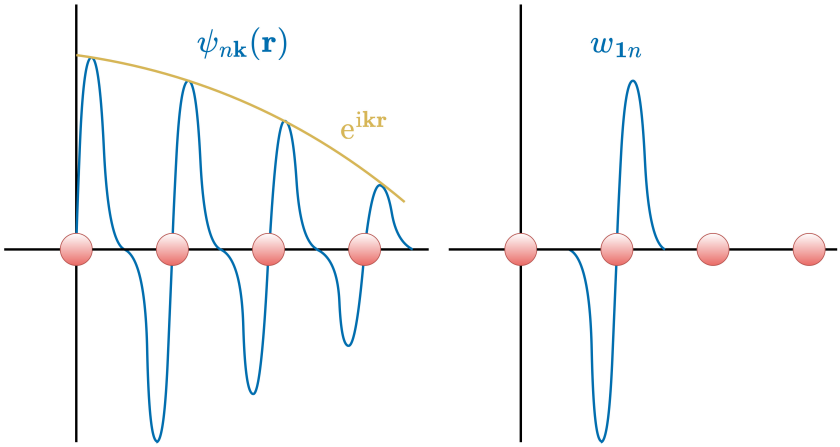

Figure 2.11: Schematic comparison of a Bloch function $\psi_{n\mathbf{k}}$ (left hand side) with specific crystal momentum $\mathbf{k}$ and a Wannier function $w_{\mathbf{1}n}$ (right hand side) centered on the atomic site $\mathbf{1}$. In contrast to the Bloch function, which is delocalized through the envelope function $e^{i\mathbf{kr}}$, the Wannier function is localized in real space.

Nonetheless, just like Bloch orbitals, Wannier functions form an orthogonal and complete basis and can be used to derive TB Hamiltonians from first-principles electronic structure calculations. Mathematically, Wannier functions $w(\mathbf{r})$ can be expressed as a linear combination of atomic orbitals: $w(\mathbf{r}-\mathbf{R}_m) = \sum_n c_n\phi_n(\mathbf{r}-\mathbf{R}_m)$. This establishes them as a foundation for TB wavefunctions. More generally, as mentioned before, they are related to Bloch wavefunctions through a Fourier transform:

$$w_{\mathbf{R}n}(\mathbf{r}) = \frac{V}{(2\pi)^3}\int_{\mathrm{BZ}} \mathrm{d}\mathbf{k}\, \psi_{n\mathbf{k}}(\mathbf{r})e^{-i\mathbf{kR}}e^{i\phi_n(\mathbf{k})}. \tag{2.115}$$

In this equation, a gauge phase factor $e^{i\phi_n(\mathbf{k})}$ is introduced, accounting for the non-uniqueness of Wannier functions. In fact, the gauge can be flexibly chosen already in

the Bloch functions, altering them as

$$\psi_{n\mathbf{k}}(\mathbf{r}) \rightarrow \mathrm{e}^{\mathrm{i}\phi_n(\mathbf{k})}\psi_{n\mathbf{k}}(\mathbf{r}). \tag{2.116}$$

This gauge freedom is mirrored in the transformation of the cell-periodic part of the Bloch functions by a unitary matrix $U^{\mathbf{k}}$ so that

$$u_{n\mathbf{k}} \rightarrow \sum_{m=1}^{N_{\text{bands}}} U^{\mathbf{k}}_{mn} u_{m\mathbf{k}}. \tag{2.117}$$

Consequently, Equation 2.115 can be restructured as

$$w_{\mathbf{R}n}(\mathbf{r}) = \frac{V}{(2\pi)^3}\int_{\text{BZ}} \mathrm{d}\mathbf{k} \left[\sum_{m=1}^{N_{\text{bands}}} U^{\mathbf{k}}_{mn}\psi_{m\mathbf{k}}(\mathbf{r})\right] \mathrm{e}^{-\mathrm{i}\mathbf{k}\mathbf{R}}. \tag{2.118}$$

The flexibility in gauge selection and the transformation U enables tailoring the desired attributes of Wannier functions, such as minimizing their spatial distribution.

2.5.1 Constructing Maximally Localized Wannier Functions

A valuable tool in crafting Maximally Localized Wannier Functions (MLWFs) [75–77] is `Wannier90` [78, 79], which leverages a method pioneered by Marzari and Vanderbilt for generating localized Wannier functions. The core concept is to curtail the spatial extent Ω through a spread minimization approach, quantified by the expression

$$\Omega = \sum_{n=1}^{N_{\text{bands}}} \left(\langle \mathbf{r}^2\rangle_n - \langle \mathbf{r}\rangle_n^2\right). \tag{2.119}$$

Here, $\langle O\rangle_n = \langle w_{n\mathbf{R}}(\mathbf{r})|O|w_{n\mathbf{R}}(\mathbf{r})\rangle$. This spread can be divided into a gauge-independent component Ω_{I} and another component $\tilde{\Omega}$ which is dependent on the selection of $U^{\mathbf{k}}$ so that

$$\Omega = \Omega_{\text{I}} + \tilde{\Omega}. \tag{2.120}$$

Besides, it can be demonstrated that both Ω_{I} and $\tilde{\Omega}$ hinge upon overlap matrices that read

$$M^{(\mathbf{k},\mathbf{b})}_{mn} = \langle u_{m\mathbf{k}}|u_{n,\mathbf{k}+\mathbf{b}}\rangle. \tag{2.121}$$

These overlaps are closely related to a finite-difference expression for the gradient $\nabla_{\mathbf{k}}$ established on a uniform $\mathbf{k}$-point mesh. The vectors $\{\mathbf{b}\}$ link each $\mathbf{k}$-point with its adjacent neighbors. Each level of nearest neighbors corresponds to a so-called shell. The finite-difference formulation following the Marzari-Vanderbilt scheme encompasses N_{sh} shells of nearest neighbors, with the s-th shell containing M_s vectors. The nearest-neighbor vectors must then satisfy

$$\sum_{s=1}^{N_{\text{sh}}} w_s \sum_{i=1}^{M_s} b^{i,s}_{\alpha} b^{i,s}_{\beta} = \delta_{\alpha\beta}. \tag{2.122}$$

Here, w_s signifies associated weights and $b^{i,s}_{\alpha}$ is the i-th nearest-neighbor vector belonging to the s-th shell (α, β are the cartesian coordinates). For an isolated set of bands, such as the valence states in an insulator, the minimization of Ω equates to minimizing $\tilde{\Omega}$. Still, for obtaining MLWFs in entangled energy bands, an additional step of a so-called disentanglement procedure is indispensable.

2.5.2 The Disentanglement Procedure

The first step of this disentanglement process [76] involves delineating an outer energy window encompassing the N bands targeted for MLWF derivation. For that reason, the number of bands $N_{\mathbf{k}}$ within this window matches or surpasses the desired band number N ($N_{\mathbf{k}} < N$ is not allowed). Introducing the $N_{\mathbf{k}}$-dimensional Hilbert space $\mathcal{F}(\mathbf{k})$, constituted by states falling within the window, elucidates the scenario. In the instance of $N_{\mathbf{k}} = N$, no further action is needed. However, when $N_{\mathbf{k}} > N$, our intention is to identify the optimal N-dimensional subspace $\mathcal{S}(\mathbf{k}) \subseteq \mathcal{F}(\mathbf{k})$ that yields the minimal value of Ω_{I}. Once this optimal subset $\mathcal{S}(\mathbf{k})$ is obtained, the subsequent steps echo those adopted for isolated bands, culminating in the minimization of $\tilde{\Omega}$.

It can be shown that Ω_{I} diminishes as $|\langle u_{m\mathbf{k}}|u_{n,\mathbf{k}+\mathbf{b}}\rangle|^2$ increases, signifying substantial overlap between states at neighboring $\mathbf{k}$ points. Thus, the pursuit of minimising Ω_{I} interprets as reducing the mismatch of the Hilbert spaces $\mathcal{S}(\mathbf{k})$ and $\mathcal{F}(\mathbf{k})$ as the $\mathbf{k}$-point varies. In the context of `Wannier90`, this process requires a preliminary approximation for the $\mathcal{S}(\mathbf{k})$ subspace. To do so, N trial orbitals $g_n(\mathbf{r})$ are defined, subsequently enabling the computation of the matrix

$$A_{mn}^{\mathbf{k}} = \langle \psi_{m\mathbf{k}}|g_n\rangle\,, \tag{2.123}$$

yielding an $N_{\mathbf{k}} \times N$ matrix. Next, the expression

$$|\phi_{n\mathbf{k}}\rangle = \sum_{m=1}^{N_{\mathbf{k}}} A_{mn}\,|\psi_{m\mathbf{k}}\rangle \tag{2.124}$$

is calculated, generating Bloch-like orbitals which are subsequently orthogonalized and transformed into cell-periodic functions. It is noteworthy that an inner (or "frozen") energy window can also be defined as supplementary to the discussed outer energy window. The inner window pertains to a narrower energy range where the original bands must be exactly reproduced, thereby ensuring that disentanglement does not alter the band structure.

An indispensable aspect of `Wannier90` is its capacity to compute TB matrix elements. Once MLWFs are derived, a direct computation of these matrix elements is possible:

$$H_{mn}^{\mathbf{R}} = \langle w_{\mathbf{0}m}|H_{\mathrm{TB}}|w_{\mathbf{R}n}\rangle\,. \tag{2.125}$$

To summarize, `Wannier90` relies on the overlap matrices $M_{mn}^{(\mathbf{k},\mathbf{b})}$, the trial projection matrices $A_{mn}^{\mathbf{k}}$ and the eigenvalues $\epsilon_{n\mathbf{k}}$ over the uniform $\mathbf{k}$-point grid. These data can be sourced from electronic structure packages like `Quantum Espresso` or `VASP` or generated through independent calculations.

2.6 Molecular Dynamics

Through the Born-Oppenheimer approximation, we exploited the possibility of decoupling the trajectories of nuclei and electrons, positing stationary nuclei while

electrons move. Still, numerous optoelectronic characteristics of HaPs hinge on ion displacements in the lattice. To comprehend these displacements, we calculate the forces that act on the nuclei, enabling adjustments in their positions. One conceivable way is solving classical equations of motion for ions under the influence of the potential

$$V_{\text{nuc}} = \sum_{I,J} V_{IJ}(\mathbf{R}_I - \mathbf{R}_J). \tag{2.126}$$

In a classical harmonic description, we would expand this potential via a Taylor series about the equilibrium positions of the nuclei and consider only terms up to quadratic order.

However, if our objective involves computing optoelectronic attributes of HaPs with the TB framework, resorting to the harmonic approximation proves inadequate. In contrast, we want to go beyond harmonic motions; therefore, a direct possible way is to use molecular dynamics (MD).

2.6.1 First-Principles MD

The foundation of our approach in deriving the equations of motion in the first-principles MD framework starts with the Schrödinger equation using the full Born-Oppenheimer approximation, given by

$$\left[-\sum_I \frac{\hbar^2}{2M_I} \nabla_I^2 + E_k(\{\mathbf{R}_I\}) \right] \chi_k = \mathrm{i}\hbar \frac{\partial}{\partial t} \chi_k. \tag{2.127}$$

For simplicity, we omit the previously used index s, which denoted the joint state of both electrons and nuclei. In this context, we aim to treat nuclei as classical point particles. Achieving this involves expressing the respective wavefunctions in terms of an amplitude factor A_k, and a phase S_k according to

$$\chi_k(\{\mathbf{R}_I\}, t) = A_k(\{\mathbf{R}_I\}, t) \mathrm{e}^{\mathrm{i}S_k(\{\mathbf{R}_I\}, t)/\hbar}. \tag{2.128}$$

Substituting this into equation 2.127 and partitioning the real and imaginary components yields two equations. The first equation

$$\frac{\partial A_k^2}{\partial t} + \sum_I \frac{1}{M_I} \nabla_I (A_k^2 \nabla_I S_k) = 0 \tag{2.129}$$

ensures local conservation of particle probability density $A_k^2 = |\chi_k|^2$, while revealing the presence of a current density $(A_k^2 \nabla_I S_k)/M_I$. The second equation takes the form

$$\frac{\partial S_k}{\partial t} + \sum_I \frac{1}{2M_I} (\nabla_I S_k)^2 + E_k = 0, \tag{2.130}$$

converging to an equation of motion in the Hamilton-Jacobi formalism (in the classical limit $\hbar \to 0$). Such an equation reads

$$\frac{\partial S_k}{\partial t} + H_k(\{\mathbf{R}_I\}, \{\nabla_I S_k\}) = 0. \tag{2.131}$$

In this context, S_k embodies the Hamilton's principal function, connecting coordinates $\mathbf{R}_I$ and conjugate canonical momenta $\mathbf{P}_I$ through

$$\mathbf{P}_I = \nabla_I S_k. \tag{2.132}$$

Consequently, the equation of motion for nuclei in the classical limit simplifies to

$$\frac{\mathrm{d}\mathbf{P}_I}{\mathrm{d}t} = M_I \frac{\mathrm{d}^2\mathbf{R}_I(t)}{\mathrm{d}t^2} = -\nabla_I E_k. \tag{2.133}$$

This can be interpreted as solving the Kohn-Sham equations for electrons in state k at a specific nuclear configuration, yielding potential energy E_k, which then guides nuclear motion governed by classical mechanics. As the energies E_k are directly derived from the Born-Oppenheimer approximation, this methodology is often referred to as Born-Oppenheimer molecular dynamics (BOMD). We iteratively solve time-independent Schrödinger equations for electrons in a self-consistent way while adjusting nuclear positions. An alternative formulation involves solving time-dependent electronic Schrödinger-like equations, known as the Ehrenfest method. Unlike the BOMD approach, the Ehrenfest method leans on quantum mechanical dynamics for the electronic subsystem. However, these two formulations yield equivalence when the electronic system is confined to its ground state. In this case, equation 2.133 simplifies to

$$M_I \ddot{\mathbf{R}}_I(t) = \mathbf{F}_I = -\nabla_I \min_{\psi_0}\{\langle\psi_0|H_\mathrm{e}|\psi_0\rangle\}. \tag{2.134}$$

Assuming the ground state wavefunction ψ_0 serves as an exact eigenfunction of the respective Hamiltonian, the Hellmann-Feynman theorem facilitates the direct application of the gradient on the Hamiltonian, yielding

$$\mathbf{F}_I = -\langle\psi_0|\nabla_I H_\mathrm{e}|\psi_0\rangle\,. \tag{2.135}$$

2.6.2 Force-Field MD

When employing DFT to compute the forces acting on nuclei, computational constraints limit our MD simulations to a few hundred atoms owing to high computational expenses. An alternative approach is called Force-Field MD (FF MD). It facilitates simulations involving tens of thousands of atoms and involves constructing the potential V_e through a truncated expansion of many-body contributions, commonly known as a force field (FF). This potential adopts the general structure

$$V_\mathrm{e}^\mathrm{FF}(\{\mathbf{R}_I\}) = \sum_I v_1(\mathbf{R}_I) + \sum_{I<J} v_2(\mathbf{R}_I, \mathbf{R}_J) + \sum_{I<J<K} v_3(\mathbf{R}_I, \mathbf{R}_J, \mathbf{R}_K) + \ldots. \tag{2.136}$$

Consequently, the challenge becomes a matter of classical mechanics once the distinct potential contributions v_n are established. While two-body interactions prove sufficient for numerous materials, the Force Fields of $MAPbI_3$ and $MAPbBr_3$ [80, 81] (MA is an abbreviation for the methylammonium molecule CH_3NH_3) account for more complex interactions, incorporating three- and even four-body summations. The complete potential can be expressed as

$$V_\mathrm{e}^\mathrm{FF}(\{\mathbf{R}_I\}) = V_\mathrm{ii}(\{\mathbf{R}_I\}) + V_\mathrm{io}(\{\mathbf{R}_I\}) + V_\mathrm{oo}(\{\mathbf{R}_I\}). \tag{2.137}$$

Here, V_{ii} characterizes interactions in the inorganic PbX_3 component (with X standing for I or Br), V_{oo} pertains to the organic MA molecule and V_{io} accounts for interactions between these two. The term V_{ii} comprises a two-body summation and takes the form of a so-called Buckingham potential, capturing the consequences of the Pauli exclusion principle and van der Waals interactions between bonded atoms like Pb-X. Similarly, V_{io} is a two-body sum encompassing a Buckingham potential - this time for non-bonded atom pairs (e.g., Pb/I interactions with C/N atoms) -, electrostatic interactions and a Lennard-Jones potential to describe Pb or I bonding with H atoms.

Lastly, V_{oo} includes intramolecular and intermolecular interactions of organic cations. A visual depiction of the pertinent bonds, angles, and torsions in an MA molecule can be seen in Fig. 2.12. This component involves two-body sums over parameterized energies dependent on atomic bonds b, three-body sums over parameterized energies dependent on angles θ, and four-body contributions relying on torsion angles ϕ. The term V_{oo} also covers non-bonding atom pairs with distance $\Delta\mathbf{R}_{IJ}$, incorporating electrostatics through Coulomb's law. Dispersion and exchange repulsion forces are modeled using a Lennard-Jones potential.

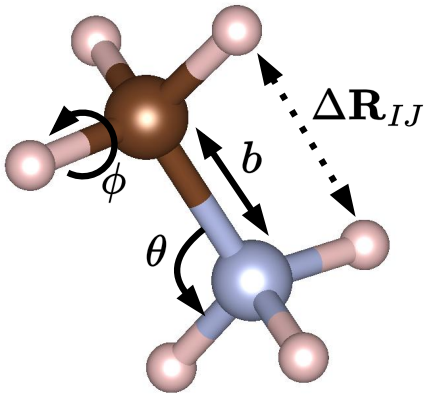

Figure 2.12: Schematic view of force field interactions from the term V_{oo} in an MA molecule. Covalent bonds are indicated by a solid line, and nonbonded interactions by a dashed line.

Once we have obtained the forces acting on each nucleus, whether through DFT or the FF formalism, we can determine their positions at a given time using the Verlet algorithm or an alternative approach. The Verlet algorithm updates the positions of nuclei based on the positions from the two previous time steps, following the equation

$$\mathbf{R}_I(t+\Delta t) = 2\mathbf{R}_I(t) - \mathbf{R}_I(t-\Delta t) + \frac{\Delta t^2}{M_I}\mathbf{F}_I(t). \tag{2.138}$$

Alternatively, one can calculate the next positions using the current positions and

velocities:

$$\mathbf{R}_I(t+\Delta t) = \mathbf{R}_I(t) + \mathbf{v}_I(t)\Delta t + \frac{\mathbf{F}_I(t)}{2M_I}\Delta t^2, \tag{2.139}$$

$$\mathbf{v}_I(t+\Delta t) = \mathbf{v}_I(t) + \frac{\mathbf{F}_I(t) + \mathbf{F}_I(t+\Delta t)}{2M_I}\Delta t. \tag{2.140}$$

However, choosing the timestep Δt appropriately is decisive for accurate and stable simulations. The timestep must be small enough to accurately capture the system's dynamics while avoiding instabilities. A large timestep might lead to unrealistic behavior, such as excessive atomic displacement in a single step or abnormally high energies. Conversely, an excessively small timestep could result in computationally expensive simulations without a benefit. The choice of timestep also depends on the phenomena under investigation. Systems with rapid dynamics, such as bond vibrations, may require a smaller timestep to accurately depict those motions. Conversely, slower processes might be adequately captured with a larger timestep. A general guideline is to ensure that the timestep is not greater than 5% of the vibrational period of the fastest motion in the system [36]. In essence, selecting the right timestep involves balancing accuracy, stability, and computational efficiency.

2.6.3 MD Thermostats and Ensembles

MD simulations can be conducted under various conditions, commonly known as ensembles. An ensemble, in the context of statistical mechanics and thermodynamics, is a hypothetical collection of many systems, each in a different microscopic state while sharing the same macroscopic properties. These properties depend on the degree of separation from the surrounding environment. An MD simulation can, for example, generate a microcanonical ensemble where the number of particles N, system volume V, and total energy E remain constant. This isolated system experiences no heat exchange, and interatomic interactions solely determine its dynamics. While the temperature in this NVE ensemble may fluctuate due to energy exchange among particles, the total energy remains constant.

Still, our interest often lies in scrutinizing materials at finite temperatures while maintaining a constant temperature throughout the simulation. To achieve this, an instantaneous temperature must be defined and compared to a reference temperature associated with a heat bath that the system is connected to. According to the equipartition theorem [39], the average internal kinetic energy, denoted as K, is directly linked to the macroscopic temperature T through the equation

$$K = \frac{1}{2}k_{\mathrm{B}}N_{\mathrm{df}}T = \left\langle \sum_I \frac{1}{2}M_I\mathbf{v}_I^2 \right\rangle. \tag{2.141}$$

Here, k_{B} represents the Boltzmann constant, and N_{df} stands for the number of internal degrees of freedom in the system. An effective method for maintaining temperature involves velocity scaling, accomplished by adjusting velocities with the equation $\mathbf{v}_{I,\mathrm{new}} = \mathbf{v}_I \cdot \lambda$. Solving equation 2.141 for T and incorporating this scaling

leads to

$$\Delta T = (\lambda^2 - 1)T(t) \quad \text{and} \tag{2.142}$$

$$\lambda = \sqrt{\frac{T_0}{T(t)}}. \tag{2.143}$$

In this context, $T_0 = T(t) + \Delta T$ represents the desired temperature. Nevertheless, this straightforward velocity rescaling technique can result in undesired artifacts, such as unrealistic changes in particle positions or inducing unphysical transient dynamics. Such issues could compromise the accuracy of simulations. An alternative approach to maintain a constant temperature is utilizing a canonical NVT ensemble. In this ensemble, the particle number, volume, and temperature remain constant while the total energy is allowed to fluctuate. This is achieved by coupling the system to a heat bath, often called a thermostat, which facilitates energy exchange with the environment to uphold the desired temperature.

A notable example of a thermostat is the Nosé-Hoover thermostat [82, 83], introduced by Nosé in 1984 and further refined by Hoover in 1985 (other thermostats are, e.g., the Andersen [84], the Berendsen [85] and Langevin thermostats [86, 87]). Diverging from simple velocity rescaling methods, which may yield unphysical outcomes, the Nosé-Hoover thermostat adopts a more sophisticated approach. It introduces an additional dynamic variable s referred to as a "thermostat variable" or "Nosé-Hoover chain variable." This variable operates akin to a fictitious particle, possessing its own equations of motion that allow it to interact with the system's degrees of freedom and effectively regulate the system's temperature.

The variable s introduces virtual coordinates $(\mathbf{R}_I, \mathbf{P}_I, t)$ for the system, establishing a connection with the real system $(\mathbf{R}'_I, \mathbf{P}'_I, t')$ through the following relations:

$$\mathbf{R}'_I = \mathbf{R}_I \tag{2.144}$$

$$\mathbf{P}'_I = \frac{\mathbf{P}_I}{s} \quad \text{and} \tag{2.145}$$

$$\mathrm{d}t' = \frac{\mathrm{d}t}{s}. \tag{2.146}$$

The Hamiltonian for the original system, incorporating the thermostat variable, can be written as

$$H = \sum_I \frac{\mathbf{P}_I^2}{2M_I}\frac{1}{s^2} + V(\{\mathbf{R}_I\}) + \frac{p_s^2}{2Q} + gk_\mathrm{B}T_0 \ln s. \tag{2.147}$$

In this context, Q denotes the mass, and p_s is the conjugate momentum of the variable s. The term $p_s^2/2Q$ signifies the kinetic energy related to the thermostat, and the potential $gk_\mathrm{B}T_0 \ln s$ establishes the coupling between the thermostat and the system. The logarithmic form ensures that the algorithm generates a canonical ensemble. Specifically, $g = N_\mathrm{df}$ for real-time sampling (Nosé-Hoover formalism) and $g = N_\mathrm{df} + 1$ for virtual-time sampling (Nosé formalism). Upon applying Hamilton's

equations and transitioning back to the real uncoupled system, we obtain

$$\frac{\mathrm{d}\mathbf{R}'_I}{\mathrm{d}t'} = \frac{\mathbf{P}'_I}{M_I}, \tag{2.148}$$

$$\frac{\mathrm{d}\mathbf{P}'_I}{\mathrm{d}t'} = -\nabla_I V(\{\mathbf{R}'_I\}) - s p_s \frac{\mathbf{P}'_I}{Q}, \tag{2.149}$$

$$\frac{\mathrm{d}s}{\mathrm{d}t'} = s^2 \frac{p_s^2}{Q}, \tag{2.150}$$

$$\frac{\mathrm{d}p_s}{\mathrm{d}t'} = \left(\sum_I \frac{{P_s}^2}{M_I} - g k_\mathrm{B} T_0 \right) \frac{1}{s} - s \frac{p_s^2}{Q}. \tag{2.151}$$

Upon closer examination, Equation 2.149 closely resembles the original equation of motion of the real system, albeit with the addition of an extra velocity-dependent force. This supplementary force can be interpreted as a friction term. Incorporating this friction term into the equations of motion ensures that the Nosé-Hoover formalism dynamically adjusts the thermostat's supplementary degrees of freedom, maintaining the desired temperature of the system. It is important to note, however, that the temperature is not always precisely conserved. In the Nosé-Hoover formalism, the temperature is generally defined as an average over time, and it is expected to fluctuate around the target temperature. These fluctuations emerge due to the inherent dynamical behavior of the system and the manner in which the system and thermostat exchange energy.

An alternative approach to temperature conservation is the Isothermal-isobaric NpT ensemble, which maintains pressure at a constant value instead of volume. Several examples for barostats are listed in Refs. [84, 85, 88, 89]. This ensemble becomes especially useful when studying systems influenced by varying external pressures, such as liquids or solids in contact with gaseous or condensed phases, or when investigating temperature-dependent phase transitions. In the NpT ensemble, the system is coupled not only to a thermostat but also to a barostat, allowing precise control over both temperature and pressure. This coupling of variables results in scaled original variables by the parameter s and the volume so that

$$\mathbf{R}'_I = V^{1/3} \mathbf{R}_I \tag{2.152}$$

$$\mathbf{P}'_I = \frac{\mathbf{P}_I}{V^{1/3} s} \quad \text{and} \tag{2.153}$$

$$\mathrm{d}t' = \frac{\mathrm{d}t}{s}. \tag{2.154}$$

The respective Hamiltonian for the NpT ensemble is then

$$H = \sum_I \frac{\mathbf{P}_I^2}{2 M_I V^{2/3}} \frac{1}{s^2} + V(\{V^{1/3} \mathbf{R}_I\}) + \frac{p_s^2}{2Q} + g k_\mathrm{B} T_0 \ln s + \frac{p_V^2}{2W} + P_\mathrm{ex} V. \tag{2.155}$$

Here, p_V is the conjugate momentum of V, W is a mass for volume motion, and P_ex represents the desired pressure. Similar to the NVT ensemble, equations of motion can be derived for the NpT ensemble as well.

Whether opting for the NVT or NpT ensemble, a general procedure of an MD simulation [37, 90] is summarized in Fig. 2.13. Initially, an atomic configuration is obtained through total energy minimization, and initial velocities are randomly generated. An equilibration run follows, serving as a crucial step before meaningful analysis or production runs. This step allows the system to achieve equilibrium and reach a state where properties of interest stabilize over time. The goal is to obtain a stable and representative system configuration, ensuring the properties remain consistent. After the equilibration run, the production run takes place, generating a trajectory that serves as the basis for calculating optoelectronic properties or further analysis.

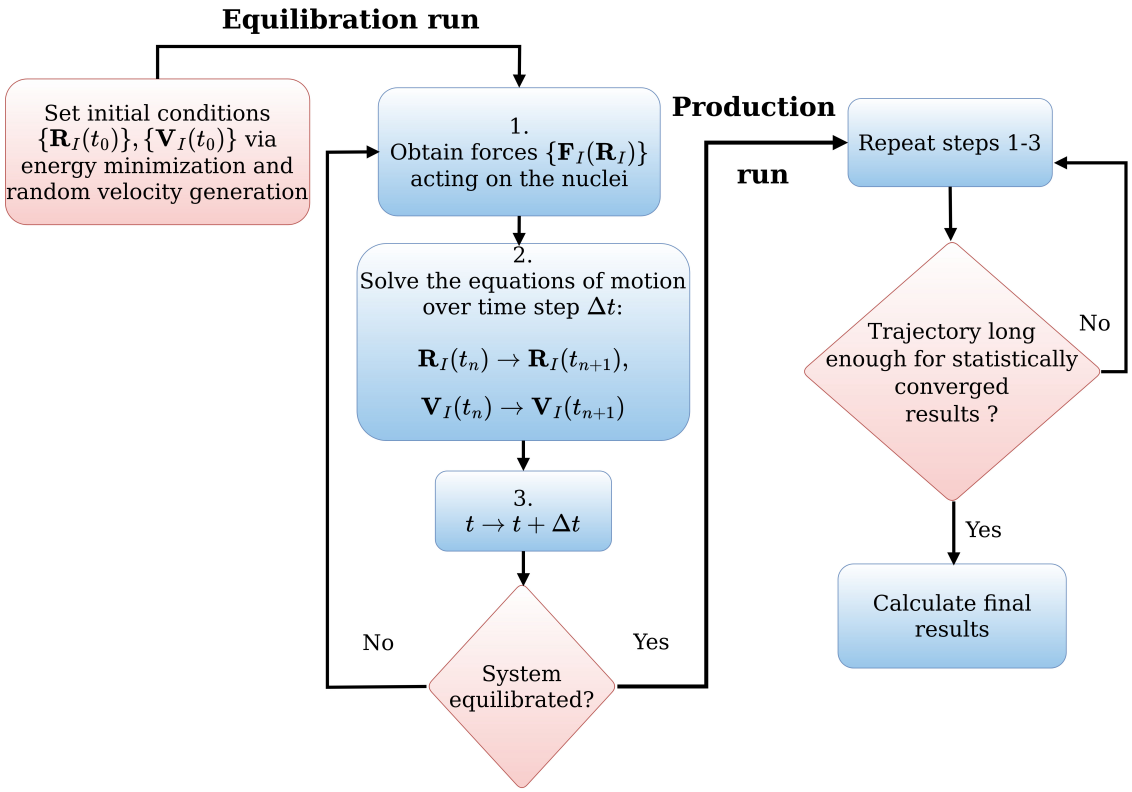

Figure 2.13: Flowchart describing the procedure of an MD simulation.

2.7 Correlation Functions

When we utilize MD, we can either conduct direct statistical analysis on the output data or perform post-processing (using tools like TB) and analyze it subsequently. Regardless of the chosen approach, there exist many tools for conducting statistical analysis. Among these, correlation functions prove especially valuable.

Correlation functions play a decisive role in unveiling relationships between random variables. They enable us to quantify the degree of statistical correlation between different data sets. Positive correlation coefficients indicate a direct proportionality, where variables increase or decrease together. Conversely, negative correlation coeffi-

cients imply an inverse relationship, where one variable increases while the other decreases. A correlation function of zero implies that quantities are uncorrelated.

The correlation function of two observables, A and B, that depend on space and time is defined as

$$C(r,\tau) = \langle A(R,t) \cdot B(R+r,t+\tau) \rangle \,, \tag{2.156}$$

where the average is computed over space and time. In the context of this work, we are mostly interested in autocorrelation functions with respect to either time or space. An autocorrelation function with respect to time is a function that computes the correlation coefficient between a data point and its lagged values at different time intervals. It helps identify any repeating patterns or dependencies in the time series. The autocorrelation function values range from -1 to 1, where 1 indicates a perfect positive correlation, -1 indicates a perfect negative correlation, and 0 indicates no correlation. The corresponding formula reads

$$C_{AA}(\delta t) = \langle A(t) \cdot A(t+\delta t) \rangle \,. \tag{2.157}$$

Accordingly, the spatial autocorrelation function is used to assess the degree of spatial correlation or clustering of values in a dataset so that

$$C_{AA}(\delta \mathbf{r}) = \langle A(\mathbf{r}) \cdot A(\mathbf{r}+\delta \mathbf{r}) \rangle \,. \tag{2.158}$$

2.7.1 The Spectral Density

The spectral density is an important tool in signal processing and Fourier analysis to analyze the frequency content or power distribution of a signal or time series data. The spectral density offers insights into the relative strength of distinct frequency components of a signal. It grants us the ability to comprehend how the energy or power of the signal is spread across various frequencies. In our context, this proves highly beneficial for establishing connections between MD quantities such as lattice vibrations and other properties such as TB energies. The spectral density, denoted as $\Phi(\omega)$, can be computed through an autocorrelation approach as

$$\Phi_A(\omega) = \int \mathrm{d}t \, \langle \delta A(t+s) \delta A(s) \rangle_s \, \omega \cdot \mathrm{e}^{-\mathrm{i}\omega t}. \tag{2.159}$$

In this equation, δA represents the deviation of the quantity A from its mean value.

2.7.2 The Vibrational Density of States

Another crucial quantity in correlation functions is the vibrational density of states (VDOS), which characterizes the distribution of vibrational frequencies or modes in a material. When a solid or molecule undergoes vibrations, it can be conceptualized as an assembly of harmonic oscillators, each corresponding to distinct vibrational modes. These modes represent various frequencies at which the constituent atoms or molecules oscillate around their equilibrium positions. The vibrational density of states captures the number of vibrational modes within a specific frequency interval.

Mathematically spoken, the VDOS, here denoted as $g(\omega)$, is a function that describes the number of vibrational modes within a frequency range $[\omega, \omega + \mathrm{d}\omega]$ and as such it can be calculated as

$$g(\omega) = \frac{V}{2\pi^3} \sum_{\nu} \int \mathrm{d}\mathbf{k}\, \delta(\omega - \omega_\nu(\mathbf{k})), \tag{2.160}$$

where the summation $\sum_\nu$ encompasses all feasible phonon modes, with $\omega_\nu(\mathbf{k})$ denoting their respective frequencies. Additionally, we introduce the velocity autocorrelation function

$$\mathrm{vacf}(\Delta t) = \langle \mathbf{v}(t) \cdot \mathbf{v}(t + \Delta t) \rangle \,. \tag{2.161}$$

Moreover, a relationship exists between the power spectrum of the velocity autocorrelation function and the vibrational density of states. This connection allows us to write

$$g(\omega) = \frac{N}{V} \int \mathrm{d}t\, \frac{\mathrm{vacf}(t)}{\mathrm{vacf}(0)} \mathrm{e}^{\mathrm{i}\omega t}, \tag{2.162}$$

where N represents the number of atoms in the investigated system, and V signifies its volume [43].

2.8 Time Evolution of Charge Carriers

In Section 2.6.1 about first-principles MD, we employed the complete Born-Oppenheimer approximation to derive equations of motion for the nuclei. Specifically, we solved the time-independent Schrödinger equations for the electrons. Still, an alternative approach known as the Ehrenfest method allows us to incorporate quantum mechanical time evolution for the electrons. Instead of utilizing the ansatz presented in Equation 2.128, we consider a total wavefunction defined as

$$\Psi(\{\mathbf{r}_i\}, \{\mathbf{R}_I\}, t) \approx \psi(\{\mathbf{r_i}\}, t) \chi(\{\mathbf{R}_I\}, t) \mathrm{e}^{\frac{\mathrm{i}}{\hbar} \int_{t_0}^{t} \mathrm{d}t'\, \tilde{E}_\mathrm{e}(t')}, \tag{2.163}$$

In this equation, the phase factor $\tilde{E}_\mathrm{e}$ is defined as

$$\tilde{E}_\mathrm{e} = \langle \psi\chi | H_\mathrm{e} | \psi\chi \rangle \,. \tag{2.164}$$

By substituting this ansatz into the time-dependent Schrödinger equation 2.1, we can follow a procedure akin to the one delineated in Section 2.6.1. This process leads us to derive an equation of motion for the nuclei that closely resembles the one presented in Section 2.6.1. Nevertheless, there exists a distinction in that the time evolution of the electrons still encompasses the complete quantum-mechanical nuclear wavefunction $\chi(\{\mathbf{R}_I, t\})$, rather than being limited to just the positions $\{\mathbf{R}_I(t)\}$. In the classical limit, the time-dependent equation governing the behavior of the electrons adopts the following form:

$$\mathrm{i}\hbar \frac{\partial \psi}{\partial t} = \hat{H}_\mathrm{e}(\{\mathbf{r}_i\}, \{\mathbf{R}_I(t)\}) \psi(\{\mathbf{r}_i\}, \{\mathbf{R}_I\}, t). \tag{2.165}$$

Here, H_e implicitly depends on time through the classical nuclear positions at time t. We can rewrite this equation using a TB Hamiltonian, yielding

$$i\hbar \frac{d\psi}{dt} = H_{TB}\psi(t). \tag{2.166}$$

This equation can be numerically solved using an exponential approach:

$$\psi(t+\Delta t) = e^{-iH_{TB}(t)\Delta t/\hbar}\psi(t) \approx \left(\sum_{n=0}^{C} \frac{(-i\Delta t/\hbar)^n}{n!} H_{TB}^n(t) \right) \psi(t). \tag{2.167}$$

In this expression, we expand the exponential function using a Taylor series. The cut-off parameter C must be chosen properly to obtain the desired accuracy. An insightful quantity for understanding electron behavior is the charge carrier mobility. This refers to the capability of charge carriers, like electrons or holes, to move through a material under the influence of an electric field. It is a fundamental property that characterizes charge transport in semiconductors, metals, and other conductive materials. The charge carrier mobility determines the speed at which charges can move, impacting the efficiency of electronic components. For instance, higher mobility is desirable for swifter switching and enhanced device performance in transistors. In materials used for solar cells or photodetectors, higher mobility facilitates efficient charge transport and collection.

The charge carrier mobility can be defined as

$$\mu = \frac{e}{k_B T} \lim_{t\to\infty} \frac{\mathrm{MSD}(t)}{6t} = \frac{e}{k_B T} D. \tag{2.168}$$

In this equation, D represents the diffusion coefficient, and $\mathrm{MSD}(t)$ corresponds to the mean squared displacement of the charge carriers. The mean squared displacement is mathematically expressed as

$$\mathrm{MSD}(t) = \langle \psi(t)|\delta r^2|\psi(t)\rangle = \langle \psi(t)| \left(r - \langle \psi(t)|r|\psi(t)\rangle\right)^2 |\psi(t)\rangle . \tag{2.169}$$

Alternatively, it can be numerically computed using

$$\mathrm{MSD}(t) = \mathrm{Tr}\left(\rho \cdot \delta r^2(t)\right). \tag{2.170}$$

Here, $\rho = |\psi\rangle\langle\psi|$ denotes the density operator of the electron (or hole) wavefunction.

2.9 Effective Masses

Closely connected to the movement of electrons or holes are their effective masses. Denoted as m^*, the effective mass of a particle refers to the mass it appears to have in the semiclassical model of transport in a crystal. In most situations, electrons and holes in a crystal exhibit responses to electric and magnetic fields that closely resemble those of free particles in a vacuum, albeit with a different mass. This means the effective mass accounts for the influence of a periodic potential on the charge carrier's mass and characterizes its response to external forces, ultimately affecting

its mobility in the solid.

According to this theory, the mobility of charge carriers is inversely proportional to their effective mass. This means electrons with lighter effective mass exhibit higher mobility, while those with heavier effective mass experience lower mobility. In general, the effective mass of charge carriers can vary in different directions due to a crystal's lattice structure. Therefore, the effective mass becomes a tensorial quantity, taking into account the anisotropic nature of materials, and we can write Newton's law as

$$\mathbf{a} = M^{-1} \cdot \mathbf{F}. \tag{2.171}$$

Here, M represents the effective mass tensor, which can be calculated as

$$M_{ij}^{-1} = \frac{1}{\hbar^2} \frac{\partial^2 E}{\partial k_i \partial k_j}. \tag{2.172}$$

It is common to compute effective masses for a specific path and starting point in $\mathbf{k}$-space, such as at the valence band maximum (VBM) for holes or at the conduction band minimum (CBM) for electrons in the case of semiconductors. Equation 2.172 can then be simplified to

$$m^* = \hbar^2 \left(\frac{\partial^2 E}{\partial k^2} \right)^{-1}. \tag{2.173}$$

A possible way to perform this calculation is to apply a parabolic fit of the form $a \cdot k^2 + c$ to the relevant dispersion relation. By obtaining the second derivative (which is equal to $2a$), the respective effective mass can be directly computed.

2.10 Skewed Gaussian Distributions

A tool that has proven effective in describing temperature-dependent band gap distributions in HaPs is skewed Gaussian distributions. A skewed Gaussian distribution is a variant of the standard Gaussian distribution in which symmetry is broken, leading to the stretching or shifting of the curve towards one side. This asymmetry arises when underlying factors influence the data more in one direction than the other. Skewed distributions can exhibit either positive skewness (right-skewed) or negative skewness (left-skewed).

The skewness of a distribution for a random variable X is quantified by its third standardized moment $\tilde{\mu}_3$ which is calculated as

$$\tilde{\mu}_3 = \mathrm{E}\left[\left(\frac{X - \mu}{\sigma} \right)^3 \right] = \frac{\mu^3}{\sigma^3} = \frac{E[(X - \mu)^3]}{(E[(X - \mu)^2])^{3/2}}. \tag{2.174}$$

Here, μ represents the mean and σ the standard deviation. To formulate a skewed version of a simple Gaussian distribution $\phi(x) = \frac{1}{\sqrt{2\pi}} \mathrm{e}^{-\frac{x^2}{2}}$, the cumulative distribution function $\Phi(x)$ comes into play:

$$\Phi(x) = \int_{-\infty}^{x} \phi(t)\, \mathrm{d}t = \frac{1}{2} \left(1 + \mathrm{erf}\left(\frac{x}{\sqrt{2}} \right) \right). \tag{2.175}$$

The skewed Gaussian distribution is achieved by multiplying the Gaussian with its cumulative distribution function, where a parameter a determines the extent of skewness. Its expression is given by

$$f(x) = \frac{2}{\sigma}\phi\left(\frac{x-\mu}{\sigma}\right)\Phi\left(a\frac{x-\mu}{\sigma}\right). \tag{2.176}$$

To visually demonstrate this concept, Fig. 2.14 shows how the parameter α influences the skewness of Gaussian distributions in both directions.

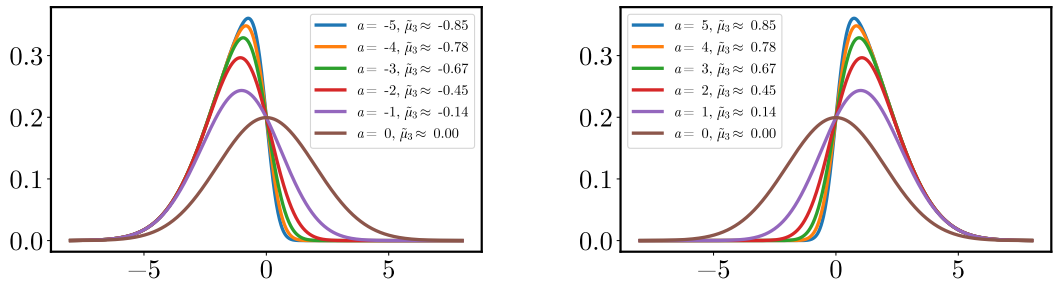

Figure 2.14: Examples of left (left panel) and right (right panel) skewed Gaussian distributions visualizing the concept of skewness.

Note that we can use either the general third standardized moment $\tilde{\mu}_3$ or the parameter a for quantifying the skewness of skewed Gaussian distributions. However, there is no linear relationship between these two. For any other skewed distribution, we can use the third standardized moment $\tilde{\mu}_3$.

3 Results and Discussion

3.1 Introduction to Hybrid HaPs

As was described in the introduction, hybrid HaPs offer significant potential to drive technological progress in energy science. They are relevant to developing cutting-edge applications, including highly efficient and cost-effective solution-processed solar cells, light-emitting diodes (LEDs), lasers [91, 92], and various other innovative devices [17, 18, 21, 93–95].

We also briefly mentioned in the introduction that hybrid HaPs are captivating materials owing to their diverse structural and optoelectronic properties. To start, we provide an overview of the composition of HaPs. They adopt a crystal structure with an $A^+B^{2+}X_3^-$ stoichiometry. In the context of hybrid HaPs, the elements are defined as follows: A represents a molecular organic cation, often an organic ammonium; X signifies a halide anion (such as iodide, bromide, or chloride); and B corresponds to a divalent metal cation (for instance, lead, tin or other metals). The ideal cubic structure of perovskite entails the B cation occupying a 6-fold coordination, surrounded by an octahedral arrangement of anions. Meanwhile, the A cation adopts a 12-fold coordination in a cuboctahedral configuration.

However, the stability of the cubic structure is subject to stringent requirements with respect to the relative ion sizes. As a result, even marginal buckling and distortion can give rise to several lower-symmetry versions, leading to a reduction in the coordination numbers of either the A or the B cations or both. Therefore, many perovskites exhibit lowered symmetry, transitioning to orthorhombic, tetragonal, or trigonal structures at lower temperatures. The existence of the cubic perovskite structure for a given combination of chemical elements A, B, and X is ascertained through the utilization of the empirical Goldschmidt tolerance factor [96].

Closely related to that, HaPs represent a class of materials known for their remarkable ionic tunability. This tunability pertains to the possibility of manipulating the chemical composition and arrangement of the A, B, and X ions in the ABX_3 stoichiometry. Notably, this holds true even for high-symmetry phases, where the ionic composition has a significant impact on the electronic, vibrational, and dielectric characteristics of HaPs [11, 97, 98]. For example, through compositional variations, it becomes feasible to fine-tune the fundamental bandgap. This parameter is of critical importance in optimizing their performance in solar cells, as it dictates the range of wavelengths of light they can efficiently absorb. Consequently, this fine-tuning enhances the power-conversion efficiencies of tandem solar cells utilizing HaPs [99]. In general, even subtle modifications in their structure can exert a profound influence on their properties [98, 100].

In the context of this work, our attention is directed towards two prototypical hybrid HaPs, namely, $MAPbI_3$ and $MAPbBr_3$. In these compounds, the *A* site is occupied by a methylammonium (CH_3NH_3 abbreviated as MA) molecule, the *B* site is taken by the metal lead, and the *X* site hosts either iodine or bromine as the halide cation. The cubic unit cells of these materials are illustrated in the top row of Fig. 3.1, while a larger representation of the periodic crystal lattice for both materials is shown in the bottom row of Fig. 3.1. It is important to note that in the unit cell of $MAPbI/Br_3$, there are always three iodine or bromine atoms. The additional three I/Br atoms visible in the cells in the top row of Fig. 3.1 are periodic duplicates of the initial I/Br atoms. In the case of the MA molecule, we have included both atoms in the unit cell and periodic duplicates to provide a more appealing depiction of the actual appearance of the MA molecule.

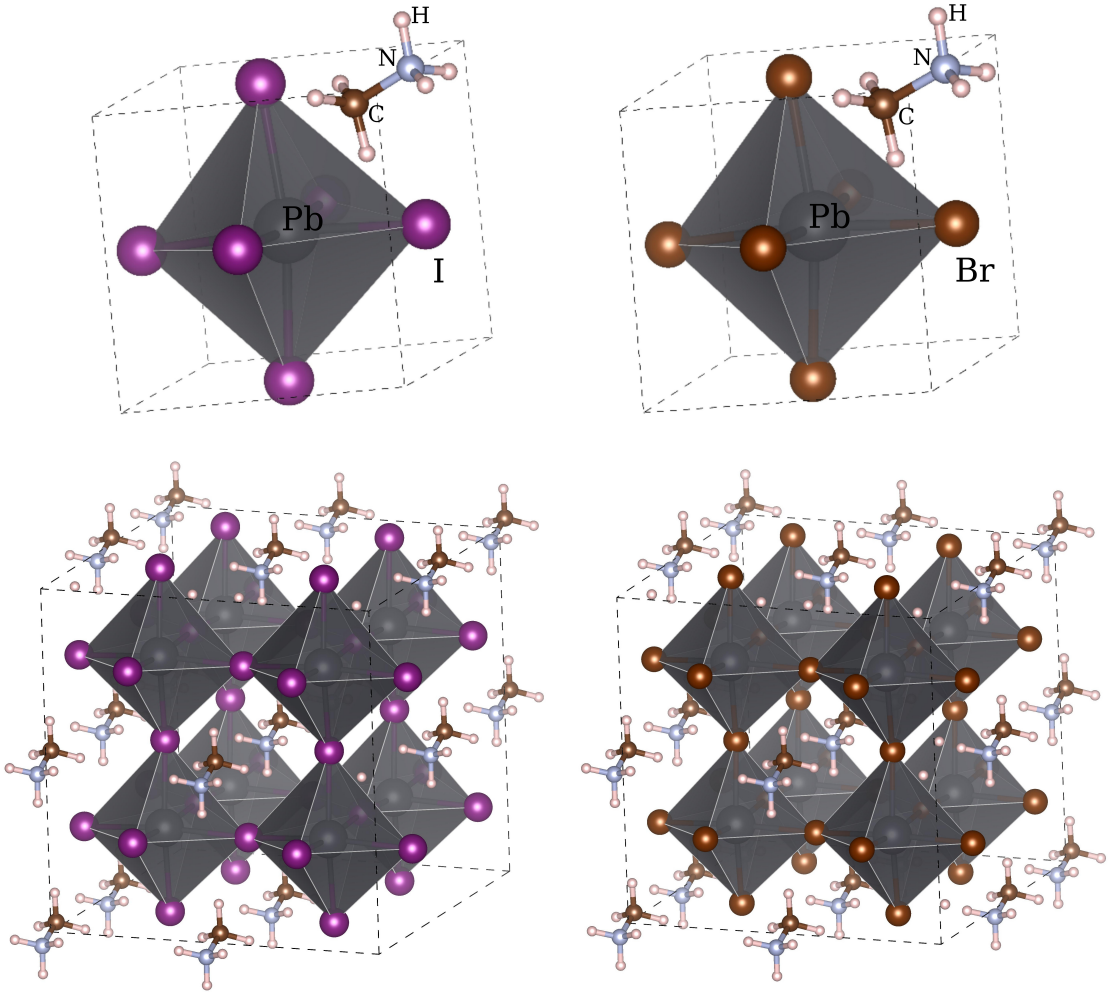

Figure 3.1: Schematic depictions of the unit cells for $MAPbI_3$ (top row, left) and $MAPbBr_3$ (top row, right), along with representations of their periodic crystal structures (bottom, left for $MAPbI_3$ and bottom, right for $MAPbBr_3$).

3.1.1 Optoelectronic Properties

HaPs demonstrate optoelectronic characteristics similar to those found in the most advantageous high-quality inorganic bulk semiconductors, as extensively documented in previous research [11, 22, 97, 101]. In addition, many HaPs, such as $MAPbI_3$, have ideal characteristics to absorb sunlight efficiently. The energy necessary to create free charge carriers (i.e., electrons or holes) matches the intensity distribution of the sun well. This can be observed since HaPs, such as $MAPbI_3$, have sharp optical absorption edges and steep optical absorption rise at energies that correspond well to the solar radiation on earth [26].

Another particularly noteworthy feature of HaPs lies in the presence of highly dispersive electronic bands and the manifestation of small effective carrier masses. These attributes have been conclusively validated through a combination of computational simulations and experimental investigations. What this essentially means is that charge carriers in HaPs possess a remarkable degree of mobility, allowing them to move with relative freedom while experiencing rapid energy changes in relation to their momentum. These qualities are highly advantageous for facilitating the transport of charge carriers. Specifically, the effective masses of holes and electrons in HaPs typically fall within the range of 0.15 to 0.25 times the electron mass. These values have been derived from a multitude of diverse experimental and theoretical studies for various compositions of HaPs [102–107].

Furthermore, HaPs have a band gap that is either direct or very close to being direct (the Rashba effect can influence it [108, 109]). Coupled with exciton binding energies smaller than thermal energy at ambient conditions in several of the prototypical HaPs [11, 97], this unique combination allows for swift separation of electrons and holes and efficient absorption of sunlight in HaP thin films. The emergence of the band edges is attributed to the Pb-*X*-structure, indicating that the *A*-site cation does not significantly influence the electronic states near the band gap. Conversely, this leads to a debate about whether the *A*-site cation merely serves as a structural stabilizer [60]. Furthermore, the substantial masses of the atoms forming the band edges result in a pronounced impact of SOC. Another notable property is the low density of states at the VBM [110].

Moreover, low non-radiative recombination rates of photo-generated carriers have been reported [111], a key factor for substantial lifetimes and extended diffusion lengths. Several hypotheses have been proposed to explain this phenomenon [24], including the potential influence of the Rashba effect [108, 109, 112, 113], the low density of deep intrinsic defects because of their high formation energies [114] or the presence of unconventional polaronic effects [115].

Also, charge carrier transport in HaPs shows intriguing phenomena, as both the calculated and measured effective masses, as well as the temperature dependence of the mobility μ in HaPs, bear similarities to those observed in inorganic PV materials. Specifically, experimental investigations consistently indicate that HaPs exhibit mobilities one to two orders of magnitude lower than those found in other inorganic PV materials, as evidenced by Refs. [116, 117]. Notably, the temperature-

dependent mobility in HaPs can be described by the relationship $\mu \propto T^x$, particularly around room temperature, where the exponent x for HaPs is approximately -1.5. This suggests that carrier scattering primarily arises from temperature-induced lattice vibrations rather than scattering caused by charged defects. The latter scenario would result in a positive temperature-dependent exponent for μ [24]. This peculiar mobility behavior challenges conventional semiconductor models, owing to the extraordinary softness of the HaPs lattice. This topic will be explored further in Section 3.9.

3.1.2 Structural Properties

Already HaPs with no organic parts show interesting structural properties such as sharp X-ray diffraction peaks, which hints at a high degree of crystalline order at unusually large length scales [118, 119]. Notably, the lattices of HaPs exhibit mechanical softness, typically 3-10 times softer than those of common inorganic semiconductors [24, 120, 121]. The term "soft lattice" signifies that atoms in the crystal lattice can easily deviate from their equilibrium positions due to the lattice's dynamic and flexible nature. One consequence of this behavior is the presence of low phonon energies [117, 120–122]. Additionally, the soft lattice significantly influences the previously mentioned structural phase transitions as temperature changes.

Among the factors contributing to this softness, the relatively large and polarizable organic cation on the A-site plays a key role. It can move and rotate in the crystal lattice, causing temporary distortions in the positions of the X anions [123]. Experimental evidence, such as neutron diffraction experiments, supports these observations [124]. The presence of the A-site cation also has a substantial impact on the coexistence of different compositions [125, 126] and the phase segregation into multiple crystalline phases [127]. The softness of the lattice in HaPs is a critical determinant of their unique properties and behaviors, setting them apart from common inorganic semiconductors [24]. Most importantly, the soft lattice leads to anharmonic effects, especially around room temperature [122, 128–145]. These anharmonic effects have significant implications for the material's properties and play an important role in understanding the characteristics of HaPs.

The anharmonicity in HaPs is closely connected to phonon mean free paths. Phonons are quantized vibrational modes in a crystal lattice, describing collective lattice excitations and transmitting lattice vibrations. Anharmonicity affects how phonons scatter and interact with the crystal lattice, which, in turn, influences their mean free paths. For HaPs, we observe phonon mean free paths that are less than half a unit cell [136, 137]. Thus, they are shorter than the structure's characteristic length, and the phonons cannot propagate freely over long distances. Instead, they become localized, which means their vibrations are confined to specific regions in the material. This is a characteristic difference compared to conventional semiconductors like Si and GaAs. Furthermore, since HaPs have a crystal structure characterized by positively charged cations (such as MA) and negatively charged halide ions (such as iodide or bromide), the ionic arrangement inherently creates a polar structure. When atoms in the HaP lattice are displaced from their equilibrium positions, this changes the distribution of charges. For example, suppose a positively charged MA cation

is displaced away from a negatively charged halide ion. In that case, it creates an electric dipole moment, also resulting in the generation of large electric fields [146]. This effect is rare in semiconductors and photovoltaic materials and has been called "local polar fluctuations" [122].

Another signature of anharmonic effects is intrinsic rattlers which also appear in lead-free HaP variants [147]. The term "intrinsic rattlers" refers to specific atomic or molecular sites in a crystalline structure that exhibit pronounced vibrational or thermal motion relative to the rest of the atoms or molecules in the material. These atomic sites are loosely bound within the lattice and can rattle or move more freely. The arrangement of many of these weak bonds in a remarkably well-coordinated network effectively maintains thermodynamic stability despite the material's inherent softness. As a result, HaPs exhibit unique electron-lattice interactions created by a broad spectrum of low-energy vibrations.

3.2 State of Research and Challenges in HaP Charge Transport

According to experimental observations and theoretical analyses, phonon scattering is one of the most important mechanisms restricting the motion of charge carriers in HaPs [24]. However, despite this consensus, there are several inconsistencies between experimental observations and the predictions made by traditional transport theories, which continue to require clarification [1]. These intricacies make it difficult for conventional theoretical formalisms [1, 148–151] to describe the optoelectronic properties in HaPs, for example, the charge carrier transport. We have already introduced several of the unorthodox finite-temperature key properties of HaPs, namely large amplitude and anharmonic atomic displacements [122, 129, 134, 139, 152–161], inducing large electric fields combined with the presence of dispersive electronic bands [11, 97, 101].

3.2.1 Traditional Transport Theory in HaPs

The traditional band theory of transport [162] is a fundamental concept in condensed matter physics and solid-state electronics. It explains how electrons move through a crystalline solid, such as a typical inorganic semiconductor. Since electronic energies are quantized into bands, we can employ the electronic structure and electron-phonon interaction techniques (such as phonon scattering or energy exchange) together with lattice dynamics to determine charge carrier transport properties [163]. For example, it is possible to evaluate carrier mobilities in bulk Si and GaAs [162].

This procedure relies on several fundamental assumptions. First, the treatment of lattice dynamics is simplified by assuming that deviations of atoms from their equilibrium positions are small. Consequently, the vibrations of atoms around their equilibrium locations are approximated as harmonic oscillations. These vibrational modes are crucial for explaining electron-phonon interactions because they influence

the potential energy experienced by charge carriers. Additionally, this interaction is described using linear electron-phonon coupling, meaning that the relationship between electrons and phonons is modeled as a linear perturbation to the electron's Hamiltonian. The analysis of linear electron-phonon coupling typically employs perturbation theory, a mathematical approach that quantifies how a system's properties change when subjected to a minor perturbing influence. In this case, the perturbing influence arises from the said interaction with small and harmonic lattice vibrations. Lastly, for lattice vibrations to be treated as perturbations to the electronic structure, their impact on the fundamental characteristics of the electronic bands, especially their energy-momentum relationship, must be relatively small and can therefore be disregarded [163]. There are cases - even for simple and well-established materials - in which the applicability of these assumptions is questioned. To be more precise, Ref. [164] suggests that higher-order processes, such as 2-phonon scattering, have a significant impact on electron-phonon scattering in GaAs.

Hence, it is unsurprising that HaPs may not lend themselves well to these conventional treatments, given their substantial lattice distortions. In the traditional framework employed to describe their behavior across a wide temperature range, including room temperature [165], electron-phonon interactions are assumed to be predominantly comprised of interactions between charge carriers and longitudinal optical (LO) phonon modes. These LO phonons are characterized by vibrations in which ions primarily move along the longitudinal axis of the crystal lattice. Additionally, adjacent ions with opposite charges oscillate in opposing directions. Consequently, LO phonons induce changes in the electrical polarization of the lattice, giving them the highest energy among all the vibrations of significance [162]. To illustrate this point, in the case of the typical HaP $MAPbI_3$, the polar phonon modes exhibit energies of approximately 16.5 meV, which is still notably lower than for those in GaAs (36.1 meV) [166]. Nonetheless, the electric fields generated by LO phonons are much greater in HaPs than in GaAs, leading to substantial alterations in the potential energy experienced by electrons. This disparity arises from the greater ionic screening with values of 0.17 ($MAPbI_3$) and 0.016 (GaAs) for $1/\epsilon^*$ ($1/\epsilon* = 1/\epsilon_\infty - 1/\epsilon_0$, where ϵ_∞ and ϵ_0 are the high-frequency and static dielectric constants). The theoretical framework to describe the interactions of charge carriers with LO phonons is referred to as the Fröhlich interaction [162, 163, 167]. This interaction is mathematically encapsulated by the Fröhlich Hamiltonian, which comprises the linear coupling between an electron and the macroscopic Coulomb potential generated by the oscillating polarization. The strength of the Fröhlich interaction, characterized by the coupling constant α, depends on material properties, including the dielectric constant. To be precise, it is proportional to the ionic screening $1/\epsilon^*$ and reads

$$\alpha = \frac{e^2}{\hbar}\sqrt{\frac{m}{2\hbar\omega_{\mathrm{LO}}}}\frac{1}{\epsilon^*}, \tag{3.1}$$

where ω_{LO} is the oscillation frequency of the LO phonon modes [168].

The reason why the Fröhlich interaction is crucial to the band theory of charge carrier transport is that it takes a central role in the Boltzmann transport equation, which serves as the foundation for characterizing how charge carriers move in crystalline

materials in the traditional picture. Next to carrier-carrier and impurity scattering, the Boltzmann transport equation also accounts for the electron-phonon-scattering. By solving it, one can derive equations that characterize the motion of charge carriers in response to external fields. Furthermore, the Fröhlich interaction is linked to the emergence of polarons. A polaron arises when a charge is placed into a polarizable medium, which, in turn, leads to lattice distortions prompting the induction of a polarization field around the charge carrier. This induced polarization essentially tracks the charge carrier's movement as it travels through the medium. The carrier, together with the induced accompanying polarization, is considered a single entity (the quasiparticle) and is called a polaron [163]. In this work, however, we adopt a somewhat flexible interpretation of the term "polaron." We also speak of polaronic effects with respect to polaron-related concepts such as linear electron-phonon coupling and harmonic lattice motion, even if the formation of a bound polaronic state does not actually occur. Polarons come in two main types: small polarons and large polarons [169]. The differentiation between these two categories depends on the degree of the electron-phonon coupling strength and the scale of the surrounding lattice distortion. In a small polaron, the electron-photon interaction is short-ranged, resulting in a localization of the charge carrier. The polaron radius, i.e., the size of the lattice distortion, is confined to approximately the lattice parameter. Conversely, long-range electron-phonon interactions characterize large polarons, and the polaron size is much greater than the lattice parameter. Furthermore, while large polarons facilitate coherent motion, small polarons involve incoherent, phonon-assisted motion [169].

Having established a link between the traditional charge carrier transport, LO phonons, and the emergence of polarons, various studies indicate that large polarons do indeed occur in the case of HaPs. Specifically, these polarons have a size of multiple unit cells in a regime of intermediate coupling strength ($\alpha \approx 2$) [166, 170]. In addition, there is an effect called "polaronic mass enhancement". This happens because the charge carrier is effectively screened by its surrounding lattice distortions, which induce a polarization field. As a consequence, the effective mass of the charge carrier increases, making it "heavier" in terms of its response to external forces, such as electric fields. Various calculations suggest that these enhancements fall within the range of 30-50% at approximately room temperature [107, 166, 171].

Several additional studies have provided more evidence for the presence of polaronic effects in HaPs. Fig. 3.2a shows that generating a stress field triggered by light absorption in $MAPbBr_3$ serves as an indicator for polaron formation [172]. Besides, Refs. [173–175] demonstrate that photoinduced compositional segregation in mixed-halide crystals, wherein different halide ions migrate to distinct spatial locations in the sample over long distances, is a footprint of polaron formation (see Fig. 3.2b). These two studies, however, may even have implications that reach beyond the use of harmonic phonons and linear electron-lattice coupling because they do not directly employ the Fröhlich Hamiltonian.

In addition to these evident polaronic effects observed in HaPs, several unresolved internal questions and issues surrounding polarons persist, driving ongoing theo-

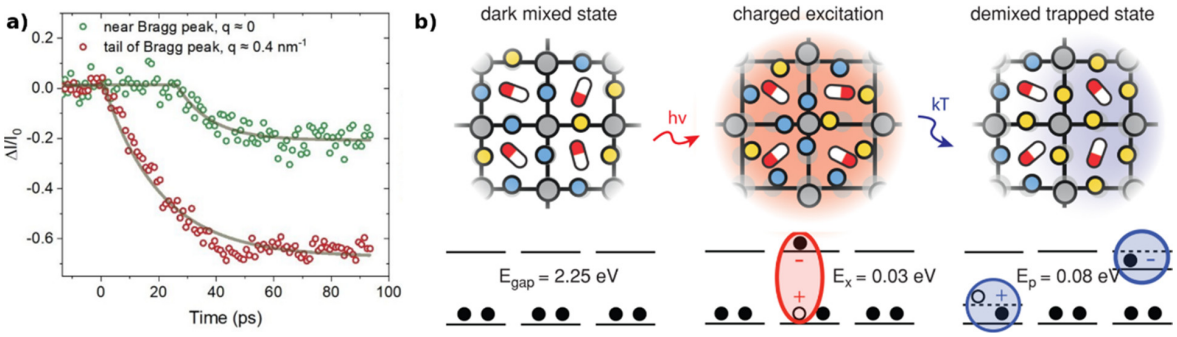

Figure 3.2: (a) Above-gap excitation leads to dynamic local strain fields, which is shown with the help of transient X-ray diffuse scattering techniques. This proves that there is a structural response of $MAPbBr_3$ as a manifestation of polaronic effects: Reprinted with permission from Ref. [176], published under a CC BY 4.0 license. (b) Local phase separation in mixed-halide HaPs at approximately room temperature arises due to polaron trapping, which, in turn, is triggered by light illumination. The figure shows blue and yellow circles, signifying distinct halide species, while also presenting the energy scales associated with polaron formation and phase separation. Reprinted with permission from Ref. [173]. Copyright 2017 American Chemical Society.

retical advancements in first-principles polaron calculations [177, 178]. We would like to briefly highlight some of these outstanding matters. First, it is noteworthy that hybrid and all-inorganic HaPs may exhibit strikingly similar polaronic behavior, which is not necessarily expected. This similarity arises from experimental findings that indicate the band masses of $MAPbBr_3$ and $CsPbBr_3$ to be quite comparable [106, 107]. Furthermore, the formation of polarons can lead to a reduction in charge carrier recombination rates. This phenomenon arises from the increase in the effective mass of charge carriers, as previously discussed, rendering them less mobile and less likely to encounter each other for recombination. Refs. [179–181] propose that polaronic effects can indeed prevent charge carriers from recombining. This contrasts with the concept of multiphonon recombination, which involves the simultaneous emission or absorption of multiple phonons during the recombination process. In this framework, polaronic effects are found to increase non-radiative recombination rates [182].

In summary, unquestionable evidence of polaronic behavior exists in HaPs. Nonetheless, the applicability of the Fröhlich interaction as a conceptual framework for describing charge transport remains uncertain due to severe disparities between experimental observations and theoretical predictions, as explained in the following section.

3.2.2 Failures and Open Questions of the Traditional Charge Transport Theory for HaPs

The temperature-dependent behavior of the band gap - and therefore electronic energy levels - is intrinsically linked to thermal vibrations of the lattice, which are

primarily caused by temperature changes. As temperature rises, the lattice vibrations alter the potential energy landscape experienced by electrons. Given the insights from the previous section, it is only natural to once again employ the harmonic approximation and the low-order electron-phonon coupling to calculate this quantity. To this end, the Allen-Heine-Cardona (AHC) theory [183, 184] is a well-established and powerful first-principles tool based on DFT and density functional perturbation theory. It incorporates phonon dispersion relations and the dynamical matrix, which establishes the connection between atomic forces in a crystal and phonon frequencies and modes. Its elements contain the second derivative of the crystal's energy with respect to atomic displacements. Using the AHC theory allows for the determination of the temperature-induced renormalization of the electronic band structure for various typical inorganic semiconductors, with increasing efforts aimed at further improvement [185–188]).

However, a noteworthy theoretical investigation by Saidi et al. [189] has revealed that the temperature dependence of the band gap in HaPs undergoes substantial changes when higher-order terms in electron-lattice coupling are considered. Although the extent to which these terms are relevant in the context of temperature-induced alterations of the lattice structure in real experiments is still a subject of discussion [190], this finding underscores that both the AHC theory and the Fröhlich Hamiltonian have limitations in their applicability to HaPs due to their reliance on low-order electron-phonon interaction terms.

Moreover, inconsistencies in the temperature dependence of HaP properties extend beyond the band gap and also affect the charge carrier mobility μ. In fact, the traditional charge transport mechanism leads to distinct temperature-dependent behaviors based on the phonon type involved. For example, in the case of acoustic phonons, where neighboring ions of opposite charges oscillate in phase, this primarily influences the charge carrier mobility through a phenomenon known as deformation potential scattering. As a result, the temperature-mobility relationship follows a power law, expressed as $\mu \propto T^{-1.5}$. Conversely, when carriers interact with optical phonons, inducing lattice polarization and the formation of polarons, the mobility follows a different trend. In general, the exponent γ in the $\mu \propto T^{-\gamma}$-law is smaller than 1.5, yielding a shallower temperature dependence [162]. To be more precise, several studies have explored various Fröhlich-type models and the concept of large polarons to understand the temperature-dependent mobility in HaPs [148, 166, 170, 191]. Their findings indeed suggest that $\mu \propto T^{-\gamma}$ with $\gamma = 0.5 - 1$. In this context, we emphasize the significance of Ref. [192], as it provides precise numerical mobility values based on the Fröhlich Hamiltonian. Assuming parameters representative of the typical HaP CsPbBr3 ($\alpha \approx 2.4$ and $\omega_{\mathrm{LO}}/T = 0.8$ at room temperature, as described in Ref. [193], with fundamental constants k_{B}, $\hbar$, and e set to 1), a careful examination of Fig. 2 in Ref. [192] reveals that within the temperature range of 200-400 K, the actual temperature dependence of the polaron mobility adheres to $\mu \propto T^{-0.5}$.

The decisive point underlying all these findings is the plethora of experimental studies [116, 194–199] conducted on various HaP samples. They have unveiled a different, somewhat surprising, relationship, namely $\mu \propto T^{-\gamma}$ with $\gamma = 1.5 - 3$. Some

of these experimental studies are shown in more detail in Fig. 3.3. Consequently, it becomes evident that the Fröhlich interaction, rooted in the harmonic approximation and low-order electron-phonon coupling, is not fully capable of accurately predicting charge carrier transport in HaPs.

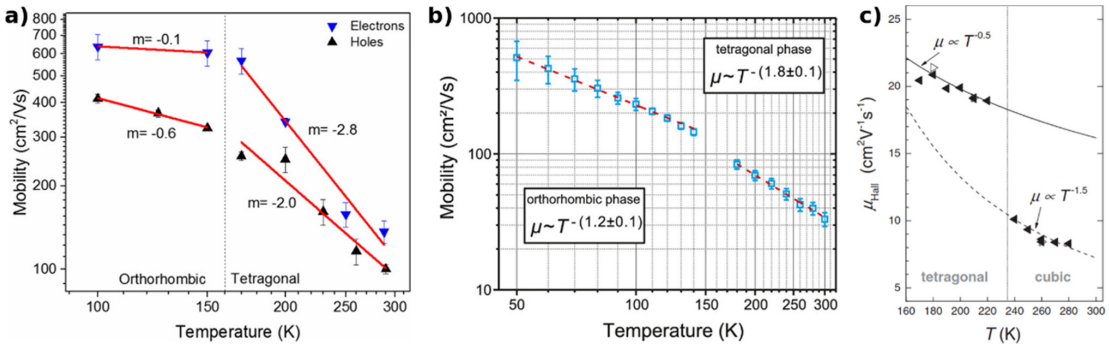

Figure 3.3: Various temperature-dependent mobility measurements conducted on several HaP samples. They firmly demonstrate a relation of $\mu \propto T^{-\gamma}$, with γ falling within the range of approximately 1.5 to 3 around room temperature. (a) Time-of-flight measurements carried out on single crystals of $MAPbI_3$. Reprinted with permission from Ref. [198]. Copyright 2018 American Chemical Society. (b) All-optical measurements performed on large-crystal $MAPbI_3$ thin films. Reprinted with permission from Ref. [199]. Copyright 2019 American Chemical Society. (c) Hall measurements conducted on single crystals of $MAPbBr_3$. Reprinted with permission from Ref. [197]. Copyright 2016 WILEY-VCH Verlag GmbH & Co. KGaA, Weinheim.

Another open question arising from Ref. [192] pertains to the divergence not only of the temperature dependence of carrier mobilities from experimental values but also the potential violation of the Mott-Ioffe-Regel (MIR) criterion [200, 201]. The MIR criterion posits that as the mean free path of a charge carrier decreases to a point where it becomes comparable to or even smaller than the atomic distance in the crystal lattice or its de Broglie wavelength, charge carriers in the material become strongly localized, rendering the material more insulating in nature. This is because the mean free path quantifies the average distance an electron/hole can travel between scattering events. In essence, if the mean free path of charge carriers becomes smaller than their own wavelength, their pronounced localization can disrupt their coherence over longer distances because their wavefunctions no longer extend coherently across the material. In other words, their motion becomes more restricted, and their quantum coherence length decreases; or, to quote Ioffe and Regel, the "electron waves fade out" [200] within the range of their own wavelength.

Returning to the findings presented in Ref. [192], this work demonstrates the violation of the MIR limit for the Fröhlich polaron model in the intermediate coupling regime ($\alpha = 2.5$). This is observed over a wide temperature range spanning $0.2 < {}^{k_B T}/_{\hbar\omega} < 10$, where $\hbar\omega$ represents the energy of an optical phonon [192]. Assuming typical optical phonon energies of $\hbar\omega_{LO} \approx 15\,\text{meV}$ for $MAPbI_3$ [165], this temperature range corresponds to 30-1740 K. Furthermore, these findings gain

additional support from Ref. [202], which employs a path-integral approach for the treatment of Fröhlich polarons. In this study, mobility calculations, based on the Feynman-Hellwarth-Iddings-Platzman linear-response theory, lend support to the violation of the MIR criterion across the specified temperature range. To assess whether this violation holds true for HaPs, we must estimate the time and length scales associated with carrier scattering in HaPs around room temperature.

To achieve this, we can use a well-established relation from the classical Drude theory of electrical conduction, which can be expressed as

$$\mu = \frac{e\tau}{m^*}, \tag{3.2}$$

where τ denotes the average scattering time (also called relaxation time) of the charge carriers. When employing typical values for HaPs at room temperature ($m^* = 0.2\,m_e$ and $\mu = 100\,\mathrm{cm^2/Vs}$), this relation yields remarkably short scattering times of $\tau \approx 5\,\mathrm{fs}$. This estimate finds support in an experimental study that utilizes terahertz photoconductivity measurements of $MAPbI_3$ at room temperature [116], reporting a similar value of $\tau \approx 4\,\mathrm{fs}$. With a thermal carrier velocity of $0.2\,\mathrm{nm/fs}$ [116], this relaxation time translates into a mean free path l of approximately 0.8 nm. Notably, both the scattering time and the mean free path are significantly smaller than those of a canonical high-quality semiconductor like Si ($\tau \approx 60\,\mathrm{fs}$ and $l \approx 10\,\mathrm{nm}$) [203, 204], as depicted in Fig. 3.4. Furthermore, the exceptionally short mean free path corresponds to just one or a few unit cells of HaPs, a conclusion further supported by both experimental and theoretical evidence presented in Refs. [116, 205, 206].

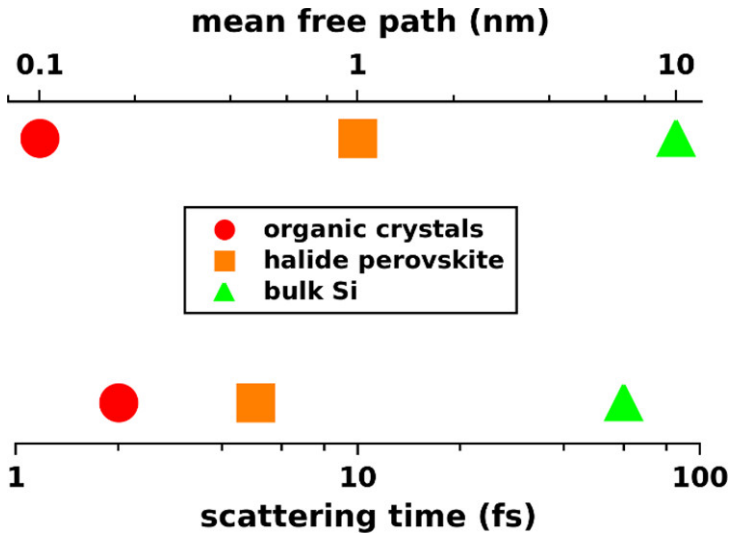

Figure 3.4: Time and length scales pertinent to carrier scattering in HaPs at room temperature. We compare estimates for the carrier mean free path and scattering time with organic crystals and the typical inorganic semiconductor silicon. Reprinted with permission from Ref. [1]. Copyright 2021 American Chemical Society.

This strongly suggests that the MIR criterion is violated in HaPs, implying that carrier transport cannot be adequately characterized by polaronic scattering and

the Boltzmann transport equation. Notably, this issue has also been discussed in the context of the perovskite $SrTiO_3$ which exhibits Fröhlich coupling similar to that observed in other HaPs [207, 208]. To elaborate further, Ref. [209] contends that violating the MIR criterion in this material renders the conventional Boltzmann transport equation inadequate. It suggests that to accurately capture charge transport, one must consider lattice anharmonicity and adopt a dynamic approach that takes into account incoherent processes. In a similar way, we assert the importance of exploring a real-space theoretical approach that transcends the conventional particle-like representation of carriers in momentum space. We refer to this as the dynamic-disorder approach.

3.2.3 The Dynamic-Disorder Formalism

First and foremost, it is important to note that the term "dynamic disorder" in our context should not be confused with its usage in a seminal study by Poglitsch and Weber. In their research, it was used to describe the disordered arrangement of the organic cation in HaPs [123]. Similarly, more previous theoretical investigations have explored the effect of the disordered MA cation on HaP properties [60, 210]. In contrast, the central aspect of the dynamic disorder approach in our discussion revolves around atom or molecule orbital overlaps, an interaction significantly influenced by low-frequency lattice vibrations. This, in turn, gives rise to the transient localization of electrons and holes [211–216].

To illustrate that concept, we provide a more vivid representation, as depicted in Fig. 3.5. In the scenario of a perfectly ordered lattice (Fig. 3.5a, left), we encounter a periodic energy landscape (Fig. 3.5a, middle) in which the charge carriers are placed. This gives rise to distinct orbital overlaps of the carrier wavefunction Fig. 3.5a, right). These overlaps can, for example, originate from the metal s and halogen p states, which hybridize into the valence band. However, in real HaP materials, this well-ordered and time-averaged geometric arrangement can be perturbed at a certain temperature (Fig. 3.5b, left) at a time t, resulting in significant atomic displacements. Consequently, the potential energy landscape undergoes a transformation (Fig.3.5b, middle), which is then reflected in the change of wavefunction overlaps (Fig. 3.5b, right). At a subsequent time $t + \Delta t$, the lattice distortions are further altered (Fig. 3.5c) compared to the previous time step. This, again, leads to substantial changes in the energy landscape and orbital overlaps. In the case of HaPs, the dynamic alterations to the disordered energy landscape occur at a relatively slow rate, primarily attributed to the slow evolution of the lead halide framework. This results in statically disordered landscapes at short time scales. It is worth noting that these distortions can, in general, result in both increased and decreased orbital overlap. However, a decrease is more likely due to the tendency for bond elongation as opposed to bond contraction.

This dynamic disorder approach is closely related to the situation in clean organic crystals such as oligoacenes (molecules that consist of linearly fused benzene rings) and rubrene (a red-colored polycyclic aromatic hydrocarbon), making it widely applicable to these and other organic crystals. Interestingly, they exhibit intriguing

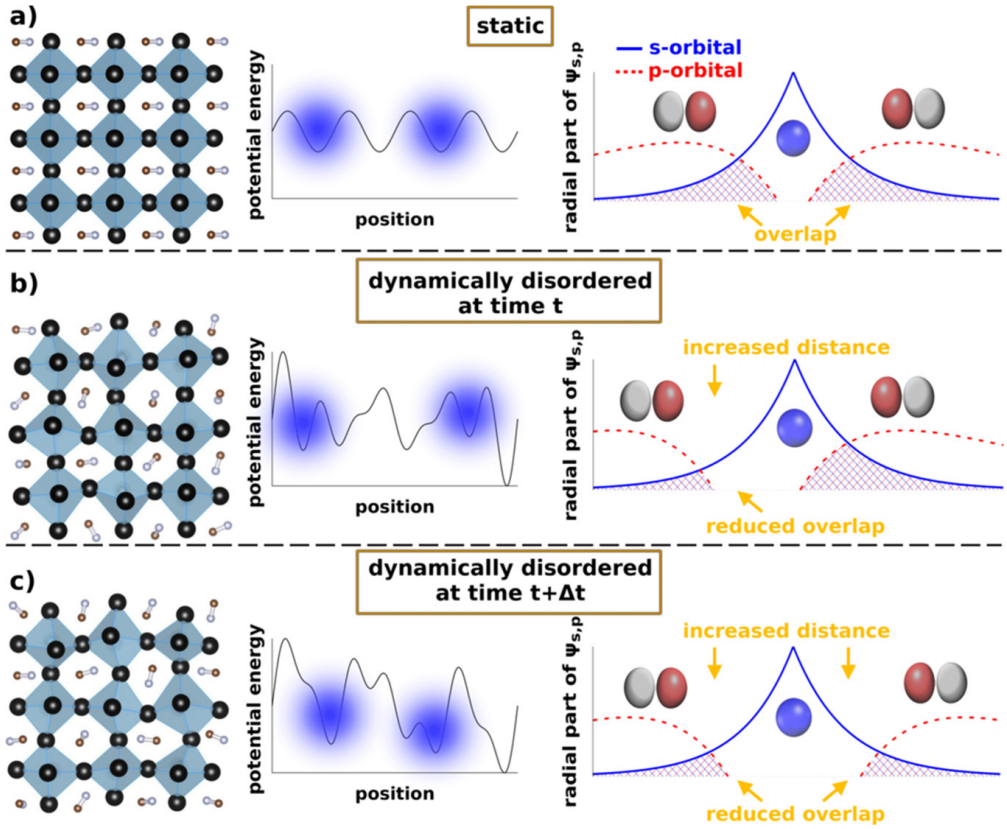

Figure 3.5: Schematic diagram of dynamic disorder resulting from electron-lattice interactions in HaPs.: Comparison of the static scenario (a), the dynamic disorder scenario at time t (b), and at a later time $t + \Delta t$ (c). The orbital overlap is depicted as the area between the radial part of an s-orbital (blue full line) and a p orbital (red-dashed curve). Reprinted with permission from Ref. [1]. Copyright 2021 American Chemical Society.

parallels with HaPs [211, 212, 217, 218]. More precisely, they display characteristics like slow, anharmonic lattice dynamics and relatively low carrier mobilities similar in magnitude to those of HaPs, and their temperature dependencies are also characterized by power-law behavior [211, 212]. Additionally, these materials exhibit incoherent carrier relaxation with short relaxation times and a likely violation of the MIR criterion [219]. Furthermore, their transport properties encompass not only features resembling band-like motion found in inorganic semiconductors but also incoherent hopping motion, which is a distinctive attribute of strongly disordered systems [213]. Last but not least, the mean free path and scattering time of the organic crystal naphthalene (one of the simplest polycyclic aromatic hydrocarbons, made of a fused pair of benzene rings) are notably comparable to those of HaPs, measuring approximately 1 nm and 1 fs [219], respectively (see also Fig. 3.4). These observations reinforce the idea that dynamic disorder may be applicable as a carrier scattering mechanism in both organic crystals and HaPs [220].

Having justified the dynamic disorder formalism as a well-suited concept for HaPs, we believe that it can help elucidate the pronounced anharmonicity in localized lattice dynamics in a real-space model for HaPs [122, 156, 160]. It offers a promising

alternative to the Fröhlich polaron model and the Boltzmann transport equation. The key requirements for its application and implementation are abandoning the conventional momentum-space representation of carriers and a grounding in first principles. Hence, the methodology employed in this work involves the construction of a multi-scale TB model, which is closely aligned with and draws inspiration from the aforementioned model introduced by Mayers et al. [5]. It adopts the dynamic disorder perspective, enabling us to calculate various optoelectronic properties and resolve discrepancies observed in experiments and established theories. To elaborate, Mayers et al. have previously demonstrated that the carrier mobility and its temperature dependence for $MAPbI_3$ are primarily governed by atomic displacements and significant fluctuations in the overlaps of carrier wavefunctions. An alternative approach was expounded by Lacroix et al. [206], who employed a modified version of the Fröhlich interaction designed to incorporate disorder and charge localization. This way, they also address the strongly nonlinear electron-lattice couplings in $MAPbI_3$ [5, 221].

Nonetheless, it is still unclear how vibrational anharmonicity and dynamic disorder are related and how they impact optoelectronic properties in HaPs. This also holds high importance for other organic [30, 213–216, 218, 222–224] and ionic semiconductors, such as $SrTiO_3$ [209]. Particularly, the examination of phonon-induced carrier scattering and its influence on finite-temperature properties, especially around room temperature, has the potential to provide valuable insights. To shed light on these questions, we apply a multi-scale TB model to HaPs that are related yet similar, specifically $MAPbI_3$ and $MAPbBr_3$, and compare them with respect to their scattering mechanisms and optoelectronic characteristics.

Before we delve into the development of a multi-scale TB model and its application to $MAPbI_3$ and $MAPbBr_3$, we first review other existing empirical TB models.

3.3 Empirical TB Models for HaPs

Several semiempirical TB models for HaPs have already been proposed, for example in Refs. [112, 225, 226]. Specifically, the empirical approach presented by Ref. [225] could serve as a starting point for developing a multi-scale TB model. In their TB model for $MAPbI_3$, Boyer-Richard et al. incorporate basis functions associated with the s and p orbitals of the Pb and I atoms, resulting in 16 basis functions. When including SOC, the Hamiltonian becomes 32-dimensional. The TB parameters are then adjusted by fitting them to experimental data, such as photoluminescence measurements at room temperature and magneto-optical measurements, as well as to theoretical data obtained from the quasiparticle self-consistent GW theory. Utilizing these fitted parameters, we can calculate the band structure of $MAPbI_3$ with and without SOC, as illustrated in Fig. 3.6.

A comparable yet subtle different method is outlined in Ref. [112], where different TB hopping parameters are tailored to be fitted to DFT band structures. Additionally, the authors of Ref. [112] introduce modifications to the TB Hamiltonian to account for spatial distortions of the atoms relative to each other. This is based on a geometrical

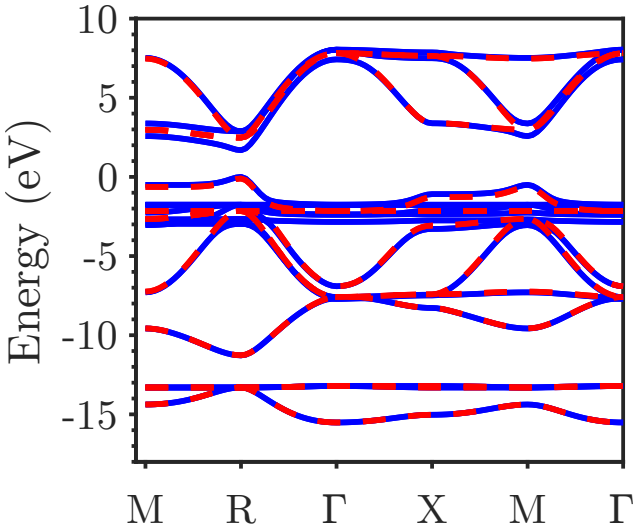

Figure 3.6: Electronic band structure of $MAPbI_3$ calculated with the TB parameters from Ref. [225]. The dashed red line represents a computation conducted without SOC, while the solid blue line represents a calculation that takes SOC into account.

approach, incorporating the angle θ and the shifts Δ_{Pb} and Δ_I, as depicted in Fig. 3.7.

Specifically, when considering hoppings to equatorial iodines (as viewed from the respective Pb atom), the approach of Ref. [112] introduces trigonometric alterations to the Hamiltonian. On the other hand, for hopping between the Pb atom and the apical iodines, an exponential decay is employed. This approach enables us to modify the band structure presented in Fig. 3.6 by accounting for spatial distortions. Nevertheless, it is important to stress that in this approach, the hopping strengths between the Pb and I atoms are altered purely through geometrical observations, lacking a foundation in quantum mechanics or first principles. In conclusion, it remains uncertain whether such models accurately represent the true physics and behavior of hybrid HaPs. Therefore, to tackle this limitation, we opt for a different approach.

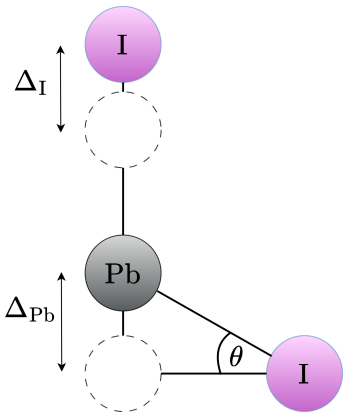

Figure 3.7: Sketch visualizing the geometric approach from Ref. [112] to incorporate distortions of the $MAPbI_3$ lattice into a TB model.

3.4 The Wannier90-TB-Model

To parameterize our TB model, we employ the `Wannier90` code to find onsite, overlap, and SOC energies. Initially, we conduct a DFT calculation at 0 K for both the $MAPbI_3$ and $MAPbBr_3$ cubic unit cells, utilizing `VASP` [227]. The core electron states are described with the help of the PAW method [56]. The DFT calculation employs a Γ-centered grid of **k**-points and a cut-off energy of 300 eV for $MAPbI_3$ and 400 eV for $MAPbBr_3$ (because the total energy in $MAPbBr_3$ is slightly more sensitive to changes of the cut-off energy). The electronic self-consistency loop is terminated when the energy difference between successive iterations is less than 10^{-6} eV. For the exchange-correlation energy, we adopt the PBE functional [51]. We utilize the Tkatchenko-Scheffler method [62], complemented by iterative Hirshfeld partitioning. Yet, it is essential to point out that this does not influence the outcomes of Wannierization. The reason is that Wannierization relies on the electronic structure and wavefunctions, which remain unaffected by the dispersive force corrections brought about by this method. Instead, these corrections solely influence the total energy of the system (which becomes crucial for first-principles MD).

In the first step, a self-consistent DFT calculation is done without SOC, albeit spin-polarized, collinear calculations are performed. This specification is chosen because we can restart a noncollinear magnetic calculation with SOC from the previous spin-polarized, collinear calculation. More precisely, the charge density and wavefunctions serve as the input for a subsequent self-consistent DFT calculation featuring SOC. Lastly, a non-selfconsistent DFT calculation is carried out, complemented by a `Wannier90` calculation [78].

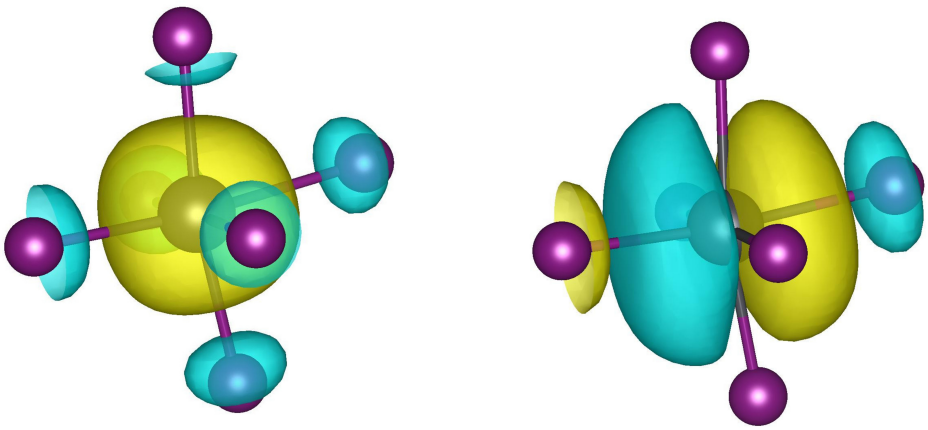

Figure 3.8: Schematic representation of the Wannier functions in the one-shot Wannier-projection scheme without spread minimization for a Pb s and p orbital. Here, the different phases of the orbitals are drawn in yellow and turquoise.

This `Wannier90` computation takes as input 96 Bloch states derived from the previous DFT calculation, and these states are utilized to determine the overlap matrix $M_{mn}^{(\mathbf{k},\mathbf{b})} = \langle u_{m\mathbf{k}} | u_{n,\mathbf{k}+\mathbf{b}} \rangle$. It is noteworthy that the approach here deviates from

the calculation of maximally localized Wannier functions. Instead, we set the number of iterations for the minimization of the spread $\tilde{\Omega}$ to zero. For that reason, `Wannier90` refrains from spread minimization. The resultant Wannier functions are aligned with the projection functions g_n, pivotal in constructing the initial estimate $A^{\mathbf{k}}_{mn}$ for the unitary transformations, achieved through $A^{\mathbf{k}}_{mn} = \langle \psi_{m\mathbf{k}} | g_n \rangle$. For these projection functions, we draw from the s and p orbitals of Pb, alongside the p orbitals of I/Br, C, and N. Fig. 3.8 shows the resulting Wannier functions, which are equivalent to s and p orbitals because there is no spread minimization. In a unit cell of $MAPbI/Br_3$, a total of 19 such orbitals are in play. Taking into account SOC leads us to have `Wannier90` assume that the Wannier functions correspond to individually occupied spinor states. This brings the total number of Wannier functions to 38 when accounting for spin degeneracy. With this in mind, we proceed to compute the matrix elements of the TB Hamiltonian in the basis of these 38 orbitals, which can be expressed as

$$H^{\mathbf{R}}_{mn}(\mathbf{k}) = \langle g_{\mathbf{0}m} | H | g_{\mathbf{R}n} \rangle \, \mathrm{e}^{\mathrm{i}\mathbf{k}\mathbf{R}}. \tag{3.3}$$

The lattice translation vectors $\mathbf{R}$ are given as multiples of the lattice vectors $\{\mathbf{a}_i\}$.

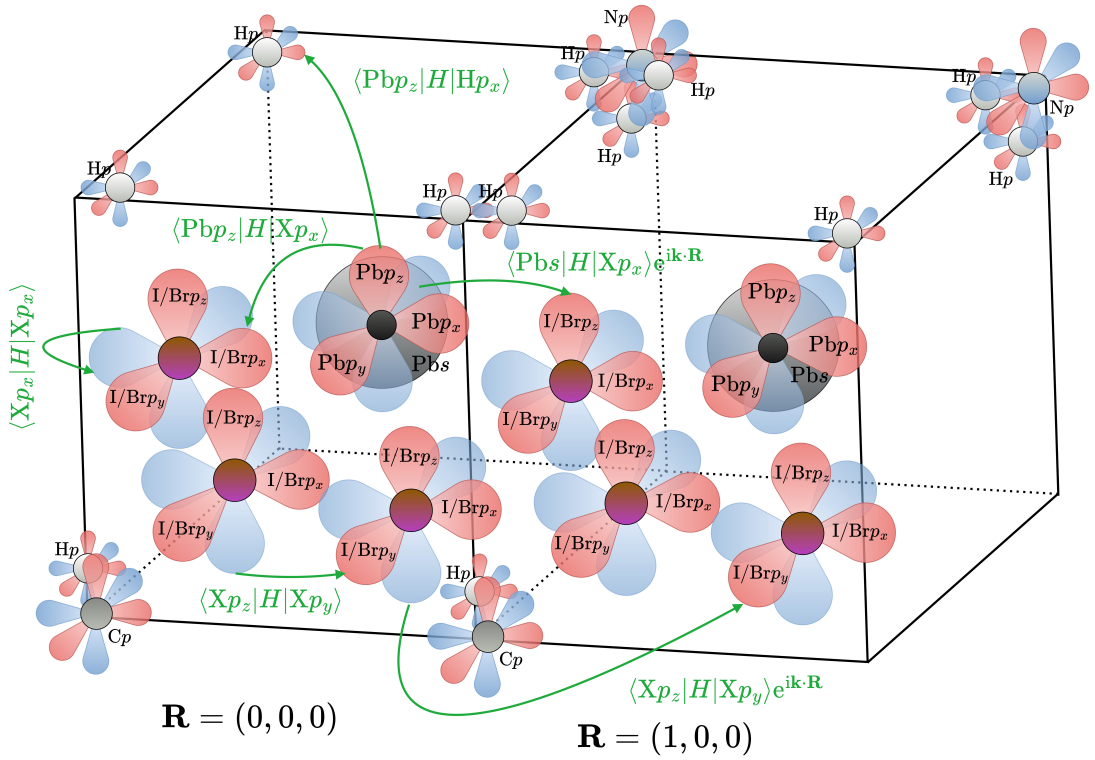

Figure 3.9: Schematic diagram of the orbitals in the $MAPbI/Br_3$ lattice and the respective TB matrix elements. Again, the different phases of the orbitals are depicted with red and blue colors. For better visual distinction, we draw the s orbital in black. Without loss of generality, it belongs to the red or the blue phase.

As an illustration, consider the case where $\mathbf{R} = (1, 2, 0)$. This signifies a translation involving the first lattice vector once and twice the second lattice vector. So, if we consider the onsite or overlap matrix elements in the unit cell at location $\mathbf{0}$, the

respective Bloch phase factor is just one. Otherwise, the respective matrix element has to be multiplied with $e^{\mathbf{k}\cdot\mathbf{R}}$. A sketch describing how to construct the Hamiltonian is shown in Fig. 3.9.

In a broader context, if our **k**-point grid comprises $N_1 \cdot N_2 \cdot N_3$ **k**-points, the Wannier functions manifest periodicity within a Wigner-Seitz supercell defined by dimensions $\mathbf{A}_i = N_i \cdot \mathbf{a}_i$, where the index i ranges from 1 to 3. We denote the supercell lattice translation vectors as $\mathbf{R}_S$. The selection of **R**-vectors, employed in the Fourier sums, includes those within this Wigner-Seitz supercell with its center at the origin. The distance of the selected **R**-vectors to $\mathbf{R}_S = 0$ is then smaller than to any other supercell lattice translation vector $\mathbf{R}_S$. This dictates that the number of **R**-vectors should precisely match the number of **k**-points. Still, a nuance surfaces: there are instances where we encounter **R**-vectors equidistant from both $\mathbf{R}_S = 0$ and one or several adjacent $\mathbf{R}_S$-vectors. In such scenarios, the respective **R**-vectors are incorporated into our set of Fourier sums while we simultaneously record the number of Wigner-Seitz supercells that "share" this specific **R**-vector. This recorded value is denoted as a degeneracy number $n_{\mathrm{deg}}(\mathbf{R})$. In the end, our total number of **R**-vectors stands either equal to or greater than our number of **k**-points, ensuring that the relation

$$\sum_{\mathbf{R}} \frac{1}{n_{\mathrm{deg}}(\mathbf{R})} = \#\mathbf{k}-\mathrm{points}. \tag{3.4}$$

is satisfied. With that, the final equation for the full TB-Hamiltonian reads

$$H_{mn}(\mathbf{k}) = \sum_{\mathbf{R}} \frac{1}{n_{\mathrm{deg}}(\mathbf{R})} \langle g_{\mathbf{0}m}|H|g_{\mathbf{R}n}\rangle \, e^{i\mathbf{k}\mathbf{R}}. \tag{3.5}$$

Both $MAPbI_3$ and $MAPbBr_3$ exhibit entangled bands. Before the process of Wannierization, which in this context yields projected Wannier Functions as opposed to maximally localized ones, we have to choose inner and outer energy windows for the subsequent disentanglement procedure, which involves the minimization of Ω_I. The convergence of this procedure is established when the fractional alteration in the gauge-invariant spread between consecutive steps falls below $4 \times 10^{-5}\,\text{Å}^2$ for 35 successive iterations. The requisite number of target bands for extraction is set to 38. This is again based on the foundation of our projection functions, which consist of a basis size of 19, which has to be doubled owing to the inclusion of spinors.

In an initial computation, we apply the method outlined here to the cubic unit cell of $MAPbBr_3$, yielding a TB band structure. We opt for an $8 \times 8 \times 8$ Γ-centered grid of **k**-points, resulting in a total of 519 **R**-points in the `Wannier90` calculation. The energies chosen for the outer and inner energy window encompass values from -8 to 8 eV and -6.15 to 7.15 eV, respectively. Fig. 3.10 (top panel) compares the band structures obtained through DFT and the Wannier90-TB model.

We observe a good agreement between the bands obtained from DFT and the TB model. Crucially, both methods yield very similar band gaps. This is of utmost significance as semiconductors, when exposed to external energy sources such as light, enable electrons to acquire sufficient energy for crossing the band gap and

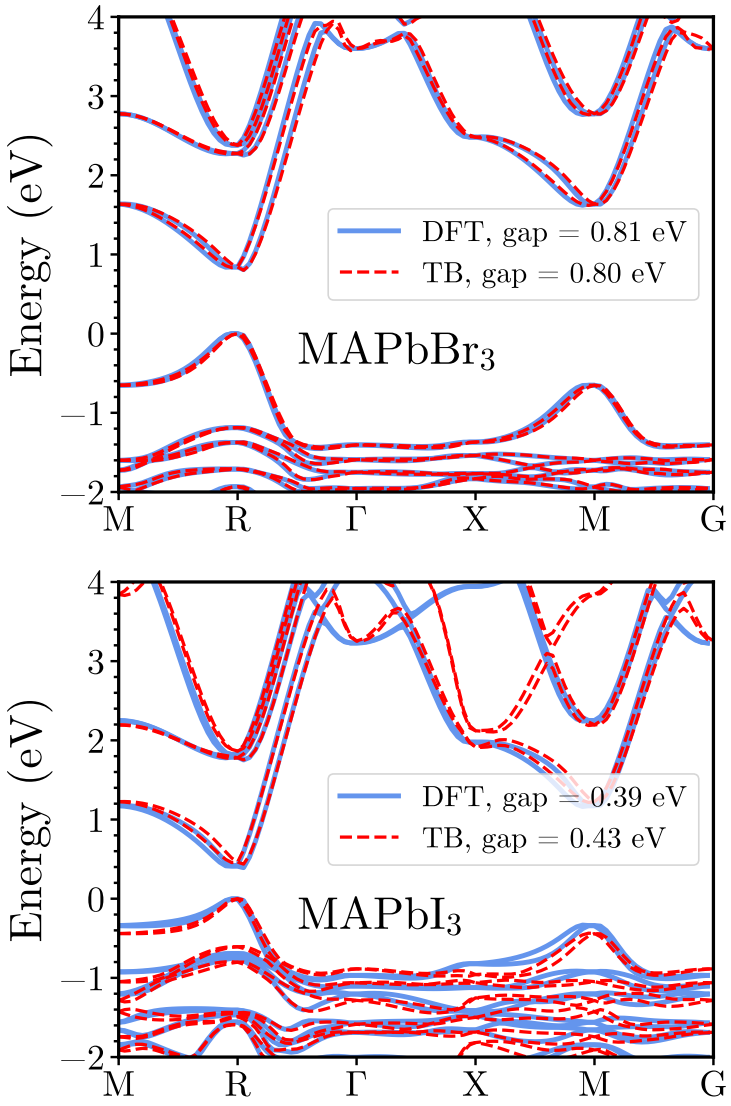

Figure 3.10: Band structures of $MAPbBr_3$ (top) and $MAPbI_3$ (bottom) calculated with the Wannier90-TB-Model and with DFT.

transitioning from the valence band to the conduction band. In this process, electron-hole pairs are generated in the semiconductor, leaving behind positively charged holes in the valence band. These mobile electrons and holes collectively contribute to the material's electrical conductivity.

In a second calculation, we apply the Wannier90-TB scheme to a cubic unit cell of $MAPbI_3$. In that case, the energy ranges for the outer and inner energy windows span from -8 to 8 eV and -5 to 6 eV, respectively. Furthermore, we utilize a $3 \times 3 \times 3$ Γ-centered **k**-point grid, implying that the **R**-vectors solely encompass shifts to unit cells that are directly adjacent to the cell at the origin, totaling 27 **R**-vectors. The resultant DFT and TB band structures are depicted in Fig. 3.10 (bottom panel).

Reducing the number of **R**-vectors is evidently associated with decreased accuracy.

Nevertheless, near the band gap, the agreement between DFT and TB bands remains satisfactory. It is essential to emphasize that in $MAPbI/Br_3$, the VBM and CBM may not necessarily be located exactly at the **R**-point owing to the presence of the Rashba effect. The Rashba effect is a phenomenon characterized by the splitting of spin states in materials with disrupted inversion symmetry at surfaces or interfaces. This splitting results from the interplay between the electron's spin and the electric field generated by the structural asymmetry which leads to potential shifts in the energy positions of the VBM and CBM. This phenomenon can fundamentally reshape the electronic band structure close to the Fermi level with wide-ranging implications, such as substantial impacts on the overall electronic and optical characteristics of the material.

In this context, it is also important to highlight how the careful selection of the inner and outer energy windows for the disentanglement can impact the accuracy of the TB method. As depicted in Fig. 3.11, a comparison of two (suboptimal) window choices is presented. The band structure is calculated for $MAPbBr_3$ without SOC and using a $4 \times 4 \times 4$ Γ-centered **k**-point grid. It becomes evident, however, that while both choices have a certain influence, this is mainly observed in the conduction bands and does not significantly affect the region around the band gap.

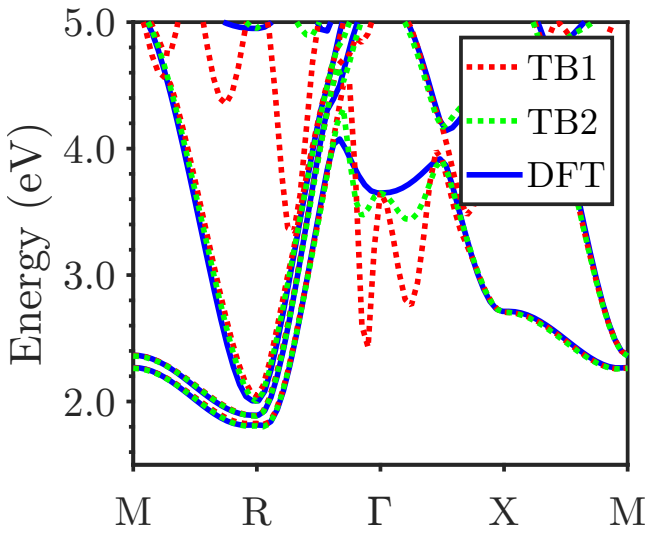

Figure 3.11: Band structure of $MAPbBr_3$ calculated with the Wannier90-TB-Model with varying combinations of inner and outer energy windows. These combinations are denoted with TB1 and TB2. Notably, the dashed green and red lines illustrate how a reasonable selection of these energy windows can enhance the agreement between the TB model and the DFT-derived bands.

Currently, our approach involves overlaps between all the s and p orbitals of Pb, in addition to the p orbitals of I/Br, C, and N. Nevertheless, our ultimate goal is to develop a straightforward and easily applicable TB method. This implies we intend to avoid performing a DFT calculation before a TB calculation. The current methodology is somewhat intricate, and we aim to achieve a higher level of simplicity.

Considering this, our strategy is to minimize the number of considered orbitals and the complexity of overlap matrix elements. Consequently, we decided to limit our focus to only the s and p orbitals of Pb and the p orbitals of I/Br. This choice is reasonable since the orbitals of the methylammonium cation do not substantially contribute to the bands in the band gap region. This way, we can simplify our calculations while still capturing the essential electronic behavior of the system. Furthermore, we choose to exclusively consider overlaps between adjacent Pb and I/Br orbitals, a scheme referred to as nearest-neighbor (NN) hopping. Specifically, this involves the consideration of spσ, ppσ, and ppπ types of overlaps (see also Fig. 2.5). The visualization of this Wannier90-NN-TB model can be found in Fig. 3.12.

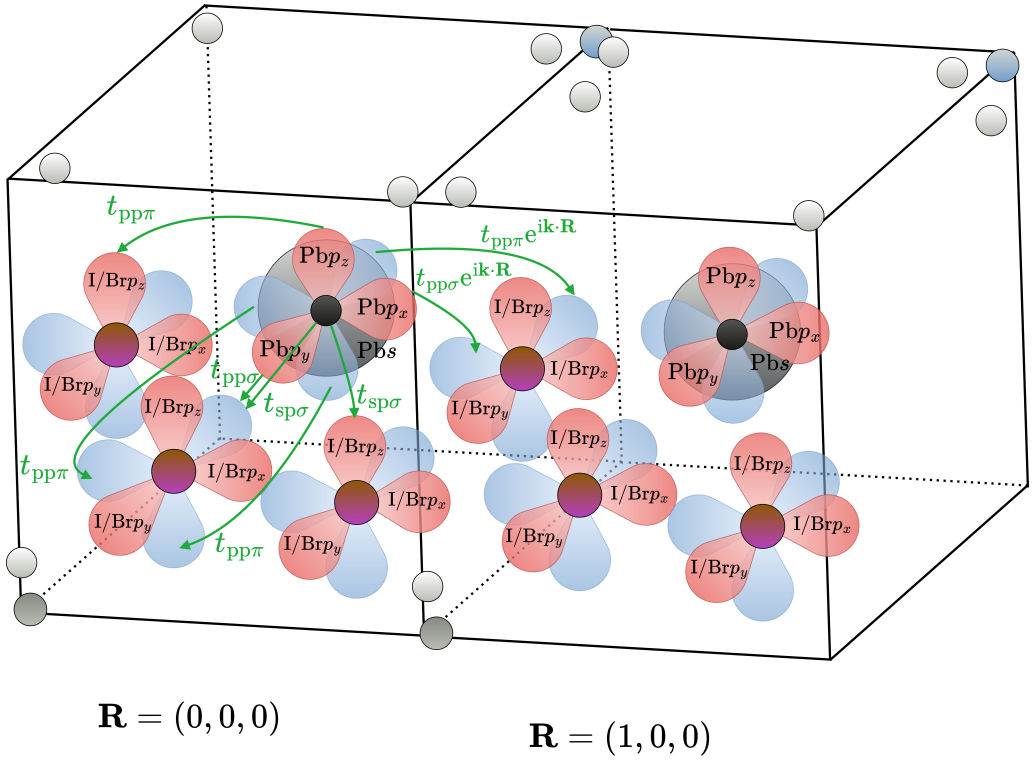

Figure 3.12: Schematic diagram of the orbitals in the $MAPbI/Br_3$ lattice and the respective TB matrix elements. Here, only nearest-neighbor overlap integrals between Pb and I/Br atoms are considered.

Using this method, we proceed to compute the TB Hamiltonians for both $MAPbI_3$ and $MAPbBr_3$ and plot their respective band structures. The outcomes are presented in Fig. 3.13. It becomes evident that there is a more pronounced deviation between the DFT and TB bands compared to our previous approach. Despite this, the overall qualitative behavior of the bands and the band gaps themselves are still accurately captured. As a result, we adopt this nearest-neighbor approach to develop our multi-scale TB model, as it offers a more simplified yet reasonably accurate representation of the electronic structure near the band gap.

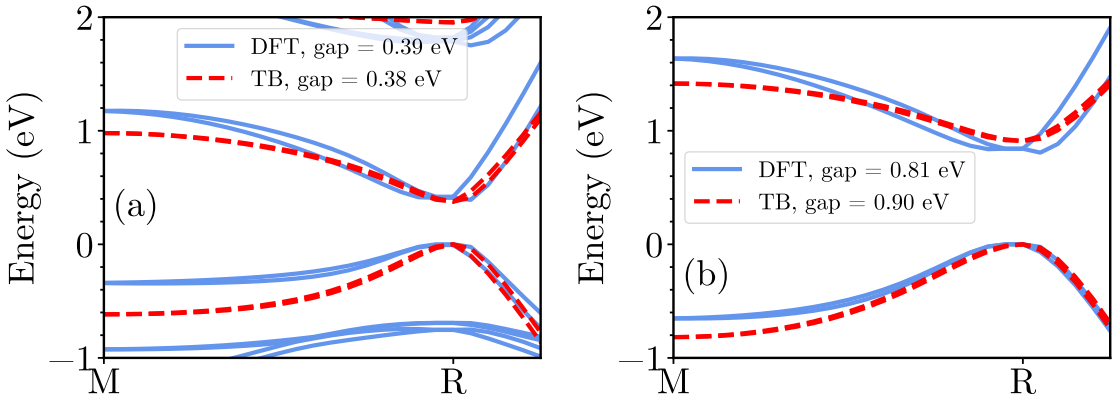

Figure 3.13: TB band structures of $MAPbI_3$ (panel a) and $MAPbBr_3$ (panel b) in the Wannier90-NN-TB-model.

3.5 The Multi-Scale TB Model

To construct the Wannier90-NN-TB model, it is necessary to perform a DFT calculation as well as a `Wannier90` calculation for each atomic configuration $\mathbf{R}(t)$ to determine the $\mathbf{R}(t)$-dependent onsite and overlap energies. However, our objective is to compute realistic and statistically significant optoelectronic properties for many snapshots of large-scale supercells of HaPs with different geometric configurations. Hence, we require a TB model that can operate independently once it has been parameterized by first-principles methods. We call this the "multi-scale TB model" and write it in second quantization as

$$H_{\mathrm{TB}}(t) = \sum_{i,\alpha} \epsilon_i^{\alpha}(\mathbf{R}(t)) c_i^{\alpha\dagger} c_i^{\alpha} + \sum_{\langle ij\rangle,\alpha} t_{ij}^{\alpha\alpha}(\mathbf{R}(t)) c_i^{\alpha\dagger} c_j^{\alpha} + H_{\mathrm{SOC}}. \tag{3.6}$$

Apart from our need for independence, the multi-scale TB model shares the key attributes of the Wannier90-NN-TB model. Specifically, it involves the inclusion of Pb s and p orbitals, as well as the p orbitals of the X atoms (amounting to a total of 13 atomic orbitals per primitive motif, denoted by indices i and j, doubled to 26 orbitals with SOC). It incorporates nearest-neighbor overlap integrals (denoted as $\langle ij\rangle$) between Pb and its neighboring X atoms. These integrals come in three types spσ, ppσ, and ppπ. Besides, the index α specifies the spin orientation.

To calculate the onsite energies $\epsilon_i^{\alpha}(\mathbf{R}(t))$, we utilize the Ewald summation method as described in section 2.4. Besides, SOC contributions arising from the interaction between p orbitals of Pb and I/Br are determined following the procedure outlined in section 2.3.4 so that the respective matrix elements are given as

$$\langle p_x^{\downarrow}|H_{\mathrm{SOC}}|p_y^{\downarrow}\rangle = -\langle p_x^{\uparrow}|H_{\mathrm{SOC}}|p_y^{\uparrow}\rangle = \mathrm{i}\gamma, \tag{3.7}$$

$$\langle p_x^{\uparrow}|H_{\mathrm{SOC}}|p_z^{\downarrow}\rangle = -\langle p_x^{\downarrow}|H_{\mathrm{SOC}}|p_z^{\uparrow}\rangle = \gamma, \tag{3.8}$$

$$\langle p_y^{\uparrow}|H_{\mathrm{SOC}}|p_z^{\downarrow}\rangle = \quad \langle p_y^{\downarrow}|H_{\mathrm{SOC}}|p_z^{\uparrow}\rangle = -\mathrm{i}\gamma. \tag{3.9}$$

Yet, to complete our multi-scale TB model, we still need to determine $t_{ij}^{\alpha\alpha}(\mathbf{R}(t))$ and the SOC-parameter γ. To achieve this, we employ first-principles MD, which enables

us to fully parameterize the multi-scale TB model. Through that, we can obtain the necessary information for accurately describing the overlap energies between neighboring atoms and establishing the SOC parameter.

3.5.1 Finding TB Parameters with First-Principles MD

We conduct first-principles MD simulations using DFT with `VASP` [227]. We expand the cubic unit cells of $MAPbI_3$ and $MAPbBr_3$ into $2 \times 2 \times 2$ supercells, forming the basis for our MD simulations. Notably, we introduce a deliberate rotation of the methylammonium molecules in these supercells, employing random angles and orientations. This rotational manipulation significantly accelerates the equilibration process of the MD simulations.

To ensure precise temperature control, we incorporate the Nosé-Hoover thermostat mechanism. Furthermore, we keep using the PBE functional [51], augmented by the Tkatchenko-Scheffler van der Waals correction [62] with iterative Hirshfeld partitioning. This correction is essential as the forces acting on the atoms critically depend on the overall energy of the system.

In terms of specific parameters, we use a cut-off energy of 400 eV, adopting a Γ-centered grid featuring dimensions of $3 \times 3 \times 3$ **k**-points. The step width in ionic relaxations is 1 fs. Our entire simulation is executed at a temperature of 300 K. This process entails MD runs of the *NVT* type, characterized by maintaining particle number, volume, and temperature. These *NVT* MD runs undergo an equilibration period of approximately 7 ps, after which they transition into production runs spanning roughly 35 ps.

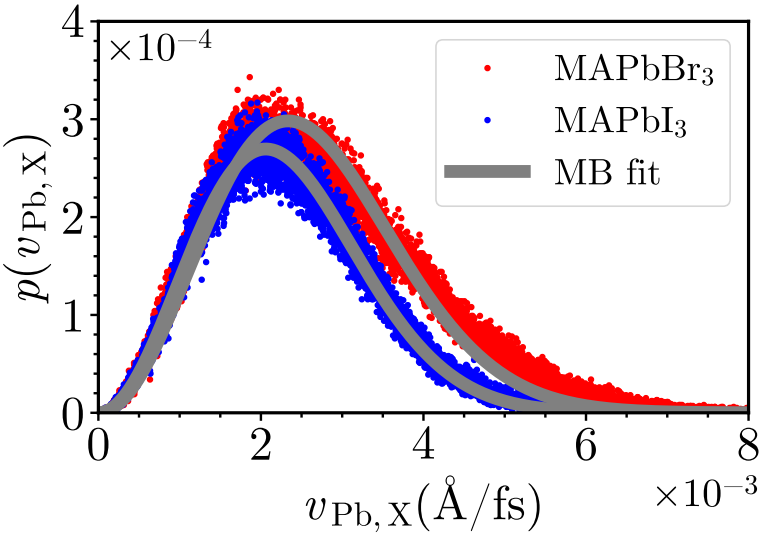

Figure 3.14: Speed distribution of the Pb and I/Br atoms in $MAPbI/Br_3$. The speeds are calculated from the DFT-MD trajectories at 300 K. The gray curves are fits of the respective data using a Maxwell-Boltzmann (MB) distribution.

To assess the validity of these production runs, we evaluate the speeds of the Pb and X atoms. They are calculated based on the outcomes of the production runs. The result of this analysis is presented in Fig. 3.14, which shows the probability distribution of the speeds. The distinctive shape of these distributions aligns with the characteristic pattern of a Maxwell-Boltzmann distribution (although at high velocities, there is a slightly stronger deviation of the $MAPbBr_3$ distribution compared to $MAPbI_3$). This relationship is to be anticipated, given that the Maxwell-Boltzmann distribution provides insight into the speed distribution of atoms in a solid [228]. Additionally, the speed distribution of $MAPbBr_3$ is notably skewed towards higher speeds when compared to $MAPbI_3$. This finding can be attributed to the relatively lighter weight of Br atoms as opposed to I atoms.

Additionally, we can compute the VDOS. As illustrated in Fig. 3.15, the VDOS of the Pb and I/Br constituents in the $MAPbI/Br_3$ supercells exhibit noteworthy contributions in the THz range. Furthermore, a subtle frequency shift is observed in the $MAPbBr_3$ spectrum, aligning well with experimental phonon frequencies as reported by Ref. [166]. These observations confirm the validity of our MD simulations.

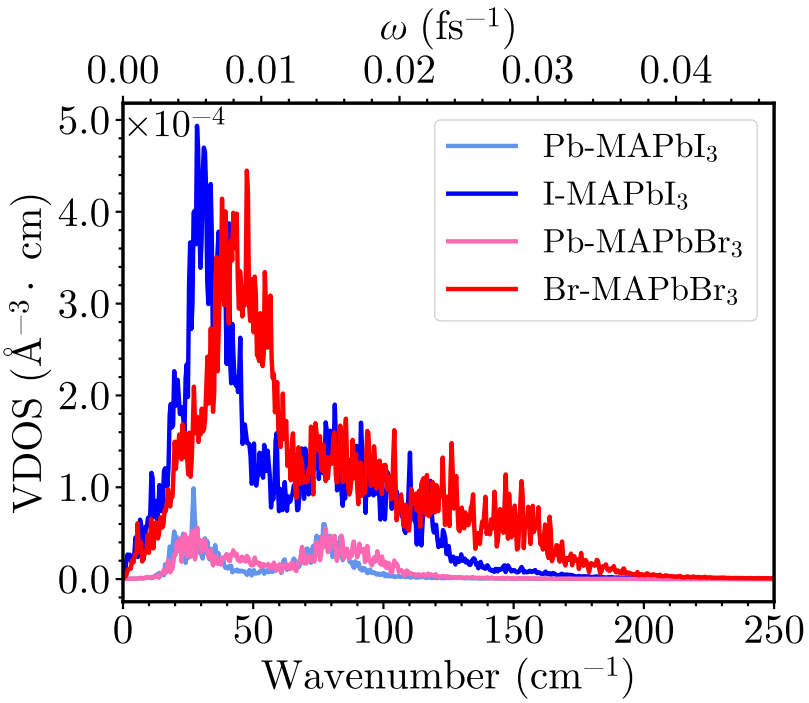

Figure 3.15: The VDOS computed for the $MAPbI/Br_3$ first-principles MD trajectory at 300 K.

Subsequently, the production runs offer an opportunity to derive information regarding the distances separating the Pb atom from its adjacent X atoms. The Pb-X bond distances and their statistical analysis are depicted in Fig. 3.16, showing the probability distribution in the form of histograms. It is not surprising that bromine exhibits greater absolute displacements than iodine owing to its smaller atomic radius, coupled with a correspondingly reduced unit cell size. Nonetheless, it is

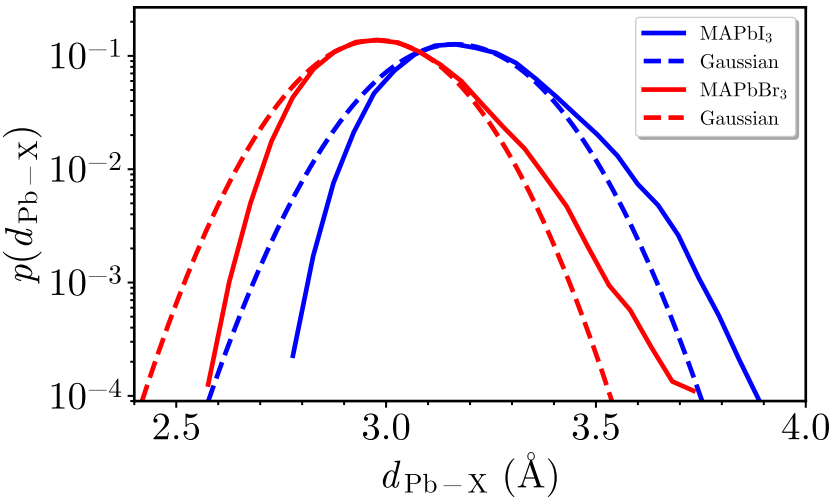

Figure 3.16: Distribution of Pb–I/Br distances, taken from the DFT-MD trajectory at 300 K.

essential to highlight a profound dissimilarity evident between the curves characterizing $MAPbI_3$ and $MAPbBr_3$ and their respective Gaussian fits. This difference serves as a clear indicator of anharmonic lattice dynamics, which will be further investigated in section 3.7, particularly in relation to diverse temperatures.

In the next step, snapshots from the first-principles MD simulations are extracted at intervals of 500 fs. These snapshots are then subjected to DFT calculations using `Quantum Espresso` [229]. The aim is to carry out again one-shot Wannier projections onto the local atomic basis with the help of `Wannier90` [79], as described in Section 3.4. However, it is necessary to make certain parameter adjustments compared to Section 3.4 since both the DFT and `Wannier90` calculations are performed on $2 \times 2 \times 2$ supercells this time.

The number of Wannier functions is determined to be 304, which includes spinors. The energy windows, both outer and inner, are set to the range of -10 to 15 eV, and -5 to 9.2 eV, respectively. Moreover, the number of Bloch functions provided to `Wannier90` from the DFT calculation is 700. Our workflow starts with a self-consistent DFT calculation, employing a $4 \times 4 \times 4$ grid of **k**-points. Subsequently, a non-self-consistent calculation is performed to derive the input matrices M_{mn} and A_{mn}, which are essential for the following `Wannier90` computations. Then, we extract the relevant values from the output files generated by Wannier90. These values pertain to three critical overlap terms spσ, ppσ, and ppπ, as well as the SOC parameter γ for the atomic species Pb and X. This extraction process involves identifying all nearest-neighbor pairs of Pb and X and retrieving the corresponding values from the `Wannier90` one-shot Wannier projections.

The outcome of our analysis reveals distinct samples for each of the three overlap terms, as depicted in Fig. 3.17 (a-c). The gray curves are fitted to the data points using the equation $a \cdot e^{-d/b} + c$, where a, b, and c represent the fitting parameters

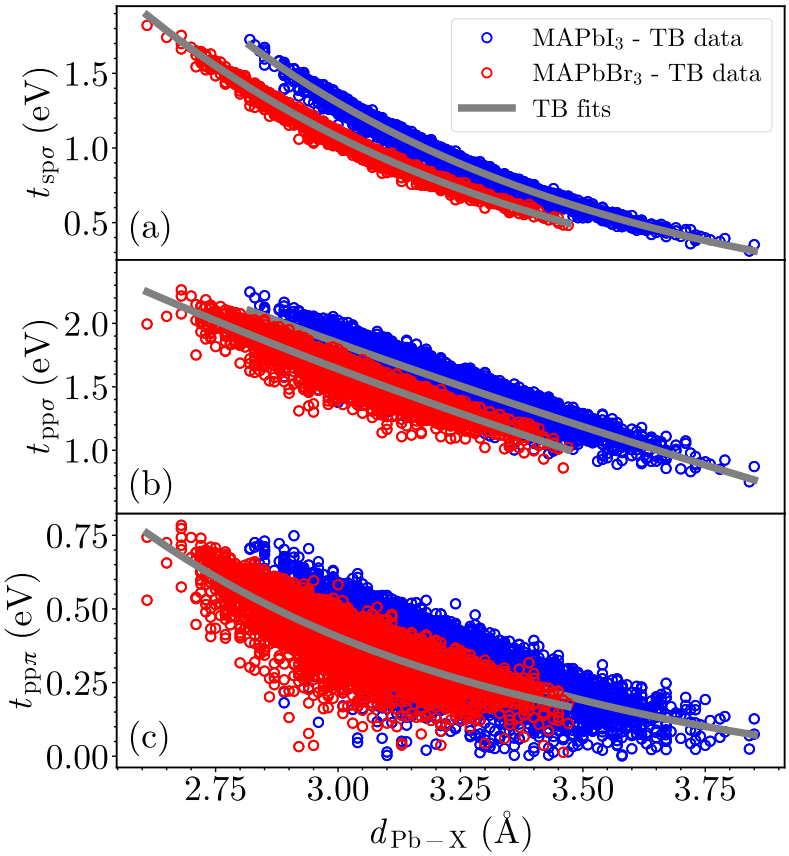

Figure 3.17: Scatter plots illustrating the variation of overlap terms ($t_{sp\sigma}$ in panel a, $t_{pp\sigma}$ in panel b and $t_{pp\pi}$ in panel c) as a function of Pb-X distances in $MAPbI_3$ and $MAPbBr_3$, extracted from one-step Wannier projections onto a local atomic basis applied to the DFT-based MD trajectories at 300 K.

and d indicates the distance between the Pb and X atoms. The extracted fitting parameters are shown in Table 3.1. The average SOC parameters were determined to be $\gamma_{Pb} = 0.52$ eV and $\gamma_I = 0.31$ eV for $MAPbI_3$, and $\gamma_{Pb} = 0.54$ eV and $\gamma_{Br} = 0.15$ eV for $MAPbBr_3$.

Table 3.1: Parameters obtained from fitting the different overlap terms, as depicted in Fig. 3.17.

$MAPbI_3$				$MAPbBr_3$			
TB Term	a (eV)	b (Å)	c (eV)	TB Term	a (eV)	b (Å)	c (eV)
spσ	67.20	0.79	-0.20	spσ	55.12	0.80	-0.223
ppσ	12.24	4.54	-4.47	ppσ	11.91	3.00	-2.74
ppπ	29.87	0.77	-0.13	ppπ	30.62	0.73	-0.09

It is crucial to emphasize that, for a given Pb-X distance, we encounter many distinct overlap energies for every type of interaction. The precise value of this overlap energy hinges on the orientation and distortion that the atoms in a Pb-X pair have with respect to each other, as elaborated upon in section 3.3. In our TB model, however, we employ the fitted function to determine the overlap values of a given structure, relying solely on the Pb-X distance. This approach statistically incorporates various angles and distortions, as the fitting process was conducted across an extensive range of samples.

We have now assembled all the necessary tools for our multi-scale TB model and can test it on the $MAPbI/Br_3$ unit cells.

3.5.2 Applying the Multi-Scale TB Model to HaP Unit Cells

To assess the efficacy of the multi-scale TB model, we use it to calculate the band structures of the unit cells for $MAPbI_3$ and $MAPbBr_3$ (as depicted in Fig. 3.18). These results confirm the anticipated behavior, most notably illustrating that the band gap of $MAPbBr_3$ surpasses that of $MAPbI_3$.

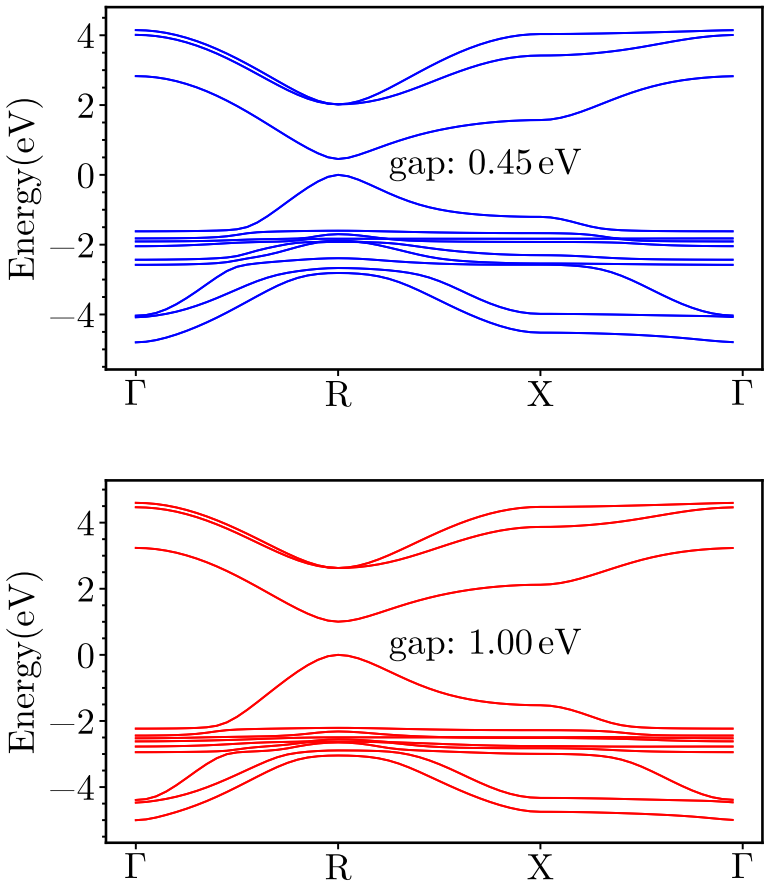

Figure 3.18: Unit cell band structure of $MAPbI_3$ (top) and $MAPbBr_3$ (bottom) calculated with the multi-scale TB model.

Our TB model also enables us to compute the electronic structure of large supercells. As an illustration, Fig. 3.19 shows the band structure of a $2 \times 2 \times 2$ $MAPbI_3$ supercell, which was extracted from an FF MD simulation (for computing FF MD trajectories, see Section 3.6, and for computing supercell electronic structures, see Section 3.8.1). We must keep in mind that a phenomenon named band folding appears when calculating the electronic structure of supercells. Band folding, sometimes called Brillouin zone folding or periodic zone folding, occurs when computing the electronic band structure of a periodic crystal using a supercell that is larger than the unit cell, resulting in a reduced Brillouin zone. This phenomenon arises because as the real-space cell size expands, the corresponding first Brillouin zone in reciprocal space contracts.

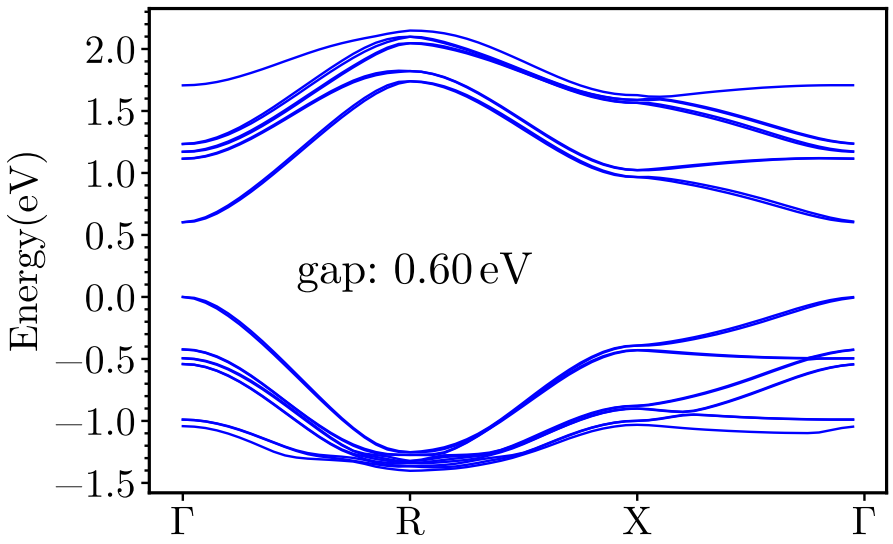

Figure 3.19: Electronic structure of a $2 \times 2 \times 2$ $MAPbI_3$ supercell computed with the multi-scale TB model.

Consequently, the electronic bands calculated in the "standard" Brillouin zone of the unit cell essentially "fold" back into the reduced Brillouin zone of the supercell. For $MAPbI_3$, this phenomenon manifests as a shift in the band gap from the R-point to the Γ-point, as illustrated in Fig. 3.19. Note that the band gap of the $2 \times 2 \times 2$ $MAPbI_3$ supercell differs from the unit cell due to its different atomic configuration obtained from an FF MD simulation.

3.6 Force-Field MD Trajectories

We now possess the tools to scrutinize the optoelectronic properties of large-scale $MAPbI/Br_3$ supercells. Employing first-principles MD for such extensive cells proves infeasible owing to the substantial computational costs that would rapidly escalate. Instead, we utilize `LAMMPS` [230] and previously established force fields [80, 81] to compute MD trajectories. We focus on realistic $MAPbI_3$ and $MAPbBr_3$ supercells, predominantly of dimensions $16 \times 16 \times 16$ (49152 atoms), using a timestep of 0.5 fs.

Our approach consists of the following steps: We start with an energy minimization, followed by *NVT* equilibration at 80 K, employing randomly generated velocities. Subsequently, we conduct several hundred picoseconds of *NpT* equilibration at this temperature. We then perform 20-50 ps of *NVT* and approximately 150 ps of *NpT* equilibration at a series of temperatures ranging from 110 K to 350 K (80 → 110 → 140 → 170 → 200 → 230 → 250 → 300 → 350 K). During this process, the temperature progressively increases, with each calculation restarting from the previous equilibration at a lower temperature. At every temperature, we extract mean values of the lattice constants based on the final 1000 *NpT* steps.

For the temperature range of 200 K to 350 K, we employ these lattice constants to conduct *NVT* equilibration runs, once again starting with energy minimization and random velocity generation, spanning approximately 1 ns. Finally, we execute *NVT*-production runs of varying durations for the diverse datasets with different purposes, as elaborated in the subsequent sections.

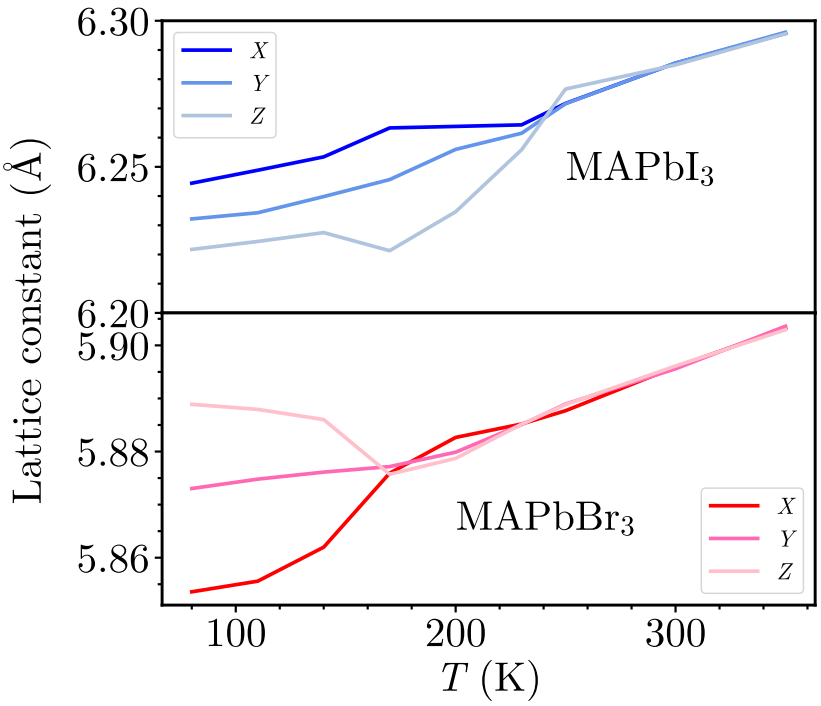

Figure 3.20: Mean values for the lattice constants of $MAPbI_3$ and $MAPbBr_3$ derived from the FF MD simulations, based on the final 1000 *NpT* steps.

The lattice constants derived from our MD simulations are presented in Fig. 3.20 for the $16 \times 16 \times 16$ supercells. It is evident that, for $MAPbI_3$, the transition from the tetragonal to the cubic structure occurs slightly above 300 K. In contrast, for $MAPbBr_3$, this phase transition happens at lower temperatures, around 240 K. These results are in excellent agreement with experimental findings [123]. This correlation can be attributed to the larger ionic radius of iodine, implying that a higher thermal energy is necessary to achieve an overall cubic symmetry in $MAPbI_3$, compared to

$MAPbBr_3$. The successful reproduction of temperature-induced lattice expansion and phase transitions through our force field MD signifies the model's capability to capture anharmonic effects.

We would like to mention that the lattice expansion and phase shifts are observable in the MD simulations conducted for smaller supercells as well ($2 \times 2 \times 2$, $4 \times 4 \times 4$, $6 \times 6 \times 6$ and $8 \times 8 \times 8$). Nevertheless, as the supercell size declines, these observations become less distinct. This underlines the primary rationale behind our preference for the larger $16 \times 16 \times 16$ supercells when computing optoelectronic properties with the help of our TB model. However, before computing these properties, we conduct a more detailed examination of temperature-dependent disorder and anharmonicity in HaPs.

3.7 Temperature-Dependent Disorder and Spatial Autocorrelations

In this section, we want to examine how the structural disorder in both $MAPbI_3$ and $MAPbBr_3$ behaves with temperature. To this end, we conduct 10 ps *NVT*-production runs, utilizing FF MD, across temperatures of 200, 230, 250, 300, and 350 K. During these production runs, snapshots are extracted at 10 fs intervals, resulting in 10000 snapshots. First, we calculate the VDOS for this 10 ps MD as well as for the 50 ps MD run (with snapshots extracted at 50 fs intervals for the latter), in both versions projected onto Pb and I/Br motions. Fig. 3.21 shows the results. We observe a no-

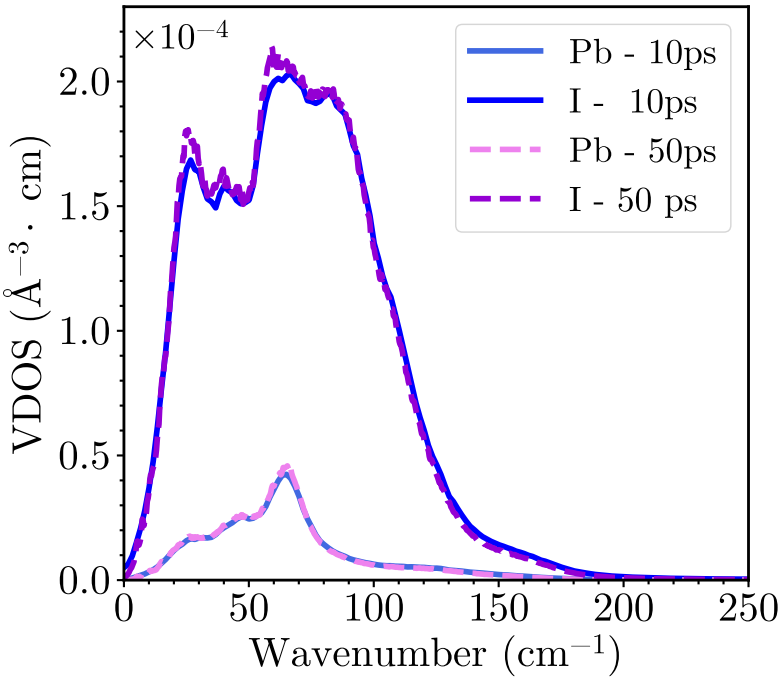

Figure 3.21: VDOS pertaining to the motion of Pb and I atoms in $MAPbI_3$ at 300 K, obtained from FF MD simulations lasting 10 ps and 50 ps (low-frequency region).

table alignment between the frequencies characterizing the VDOS depicted here and those exhibited by the first-principles MD as illustrated in Fig. 3.15. This alignment substantiates the consistency of the ab inito and FF MD. Furthermore, the results highlight an excellent agreement of the 10 ps and the 50 ps MD. This reinforces the assertion that due to the expansive and realistic nature of the supercell, a simulation time of 10 ps adequately captures statistically converged information for the VDOS and other related quantities.

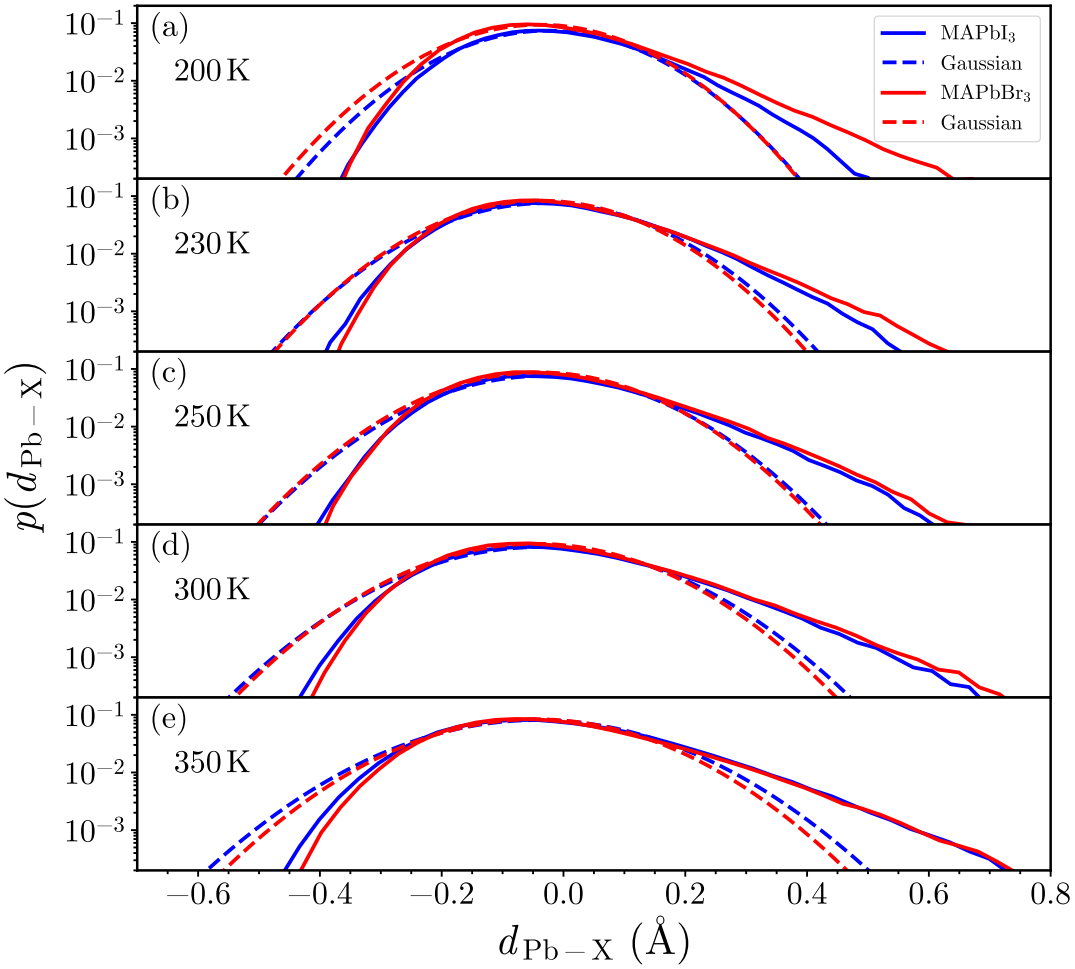

Figure 3.22: Histograms of the Pb-*X* bond-distances in $MAPbI_3$ and $MAPbBr_3$ across a temperature range extending from 200 K (panel a) to 350 K (e), calculated with FF MD calculations.

We now proceed to recalculate the Pb-*X* bond distances across various temperatures for FF MD, revisiting the analysis previously presented in Fig. 3.16 for first-principles MD. The outcomes are displayed in Fig. 3.22. As before, the dashed lines represent Gaussian fits to the corresponding distributions, with deviations from the actual data indicating the presence of vibrational anharmonic effects. The mean value of Pb-*X* bond distances is set to zero in all plots. To normalize the histograms, each value in the plot is divided by the total number of data points (with the number of bins set to 50).

Again, our initial observation highlights a significant departure from Gaussian behavior in the distributions of both $MAPbI_3$ and $MAPbBr_3$. This deviation indicates strong anharmonic behavior, in contrast to Gaussian distributions that signify a system's potential energy being directly proportional to the square of atomic displacement from equilibrium, symbolizing harmonic behavior. Particularly noteworthy is the distinction between $MAPbI_3$ and $MAPbBr_3$, especially at a temperature of 200 K. It is apparent that the Pb-Br bond-distance distributions deviate significantly more from Gaussian, anharmonic behavior compared to their Pb-I equivalents.

This deviation primarily occurs for larger-distance displacements. To quantify this observation, we calculate the ratios of the standard deviations of the respective Pb-X bond-distance distributions and their Gaussian fits. At 200 K, these values are determined to be 1.04 for $MAPbI_3$ and 1.12 for $MAPbBr_3$, validating our earlier statement that $MAPbBr_3$ exhibits a more pronounced departure from harmonic behavior. We can draw a connection between this observation and previous research on $MAPbI_3$. Ref. [137] discovered that this compound exhibits a notably more anharmonic potential surface in its cubic phase than the tetragonal phase. This disparity arises because in the tetragonal phase, anharmonic displacements and octahedral tiltings are confined to only two spatial dimensions. Given that the tetragonal-to-cubic phase transition occurs at significantly lower temperatures for $MAPbBr_3$ (around 240 K) compared to $MAPbI_3$ (approximately 330 K), as discussed in Section 3.6, it further supports our finding of stronger anharmonic behavior in $MAPbBr_3$ at lower temperatures. Moreover, our discoveries are substantiated by Ref. [156]. Through neutron-scattering experiments, this study showed that the disorder correlation length in $MAPbBr_3$ is considerably shorter than in $MAPbI_3$ at lower temperatures.

With these observations in mind, it is reasonable that at higher temperatures, the two compounds exhibit more similar degrees of anharmonicity. This trend towards convergence is visually depicted in Fig. 3.22, where the transition of the Pb-X bond distances from 200 to 350 K is illustrated. We calculate again the standard deviations of the respective Pb-X bond-distance distributions and their Gaussian fits, this time at 350 K when both compounds are in the cubic phase. The results show values of 1.08 and 1.12 for $MAPbI_3$ and $MAPbBr_3$, respectively, indicating a convergence in the degree of anharmonicity between the two compounds. Consequently, when both materials adopt the cubic phase (which is the case beyond the phase-transition temperature of $MAPbI_3$ at 340 K), disparities in bond distance distributions are small, and the anharmonic behavior of the two compounds is comparable.

As mentioned, the strongest non-Gaussian behavior appears for larger-distance displacements. This phenomenon can be described by calculating the third standardized moment $\tilde{\mu}_3$ of these distributions, quantifying their skewness (as described in Section 2.10). Fig. 3.23 shows $\tilde{\mu}_3$ of the respective distributions for $MAPbI/Br_3$. Both distributions display a right-skewed pattern, and the trend we discussed earlier becomes apparent as the skewness parameter of $MAPbI_3$ gradually approaches that of $MAPbBr_3$ as the temperature increases. Once more, this offers evidence for the increasing similarity in anharmonic behavior with rising temperatures.

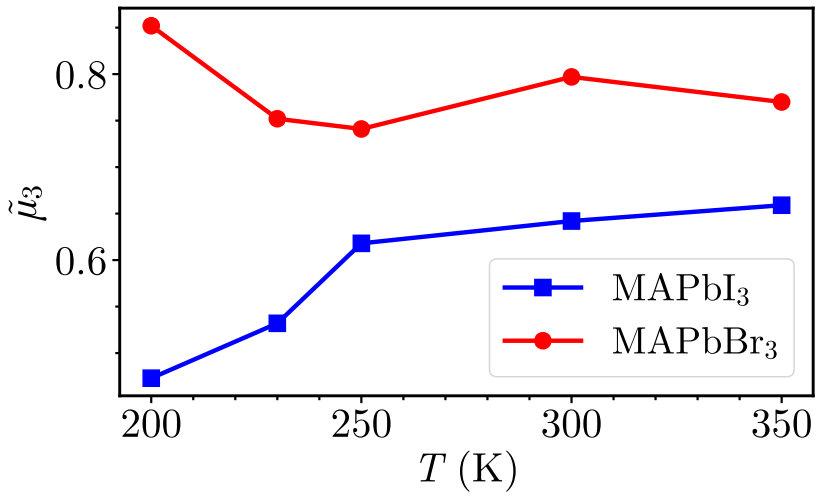

Figure 3.23: Temperature-dependent Skewness parameters of the Pb-X bond-distance distributions of MAPbI/Br$_3$.

To gain further insight into the dynamic disorder mechanism in the two compounds, we can also calculate the spatial autocorrelation function of TB onsite energies with regard to the X-atom in the two compounds. The normalized spatial autocorrelation function is defined as

$$C(\Delta r) = \frac{\langle \delta\epsilon_X(0)\delta\epsilon_X(\Delta r)\rangle}{\langle \delta\epsilon_X(0)\delta\epsilon_X(0)\rangle}. \tag{3.10}$$

Position zero refers to a specific X atom. For a meaningful result, we compute $C(\Delta r)$ for each of the X-atoms in a snapshot of the $16 \times 16 \times 16$ supercells and then determine the mean value. The outcomes for 200 and 350 K are shown in Fig. 3.24. To begin with, we would like to emphasize that the Δr values of the resulting autocorrelation functions are normalized with respect to the lattice parameters of MAPbI$_3$ and MAPbBr$_3$. The correlation lengths for absolute distances are smaller for MAPbBr$_3$ than for MAPbI$_3$, as also seen in Ref. [156]. In general, however, the spatial correlation of the TB onsite energies diminishes noticeably over very short length scales corresponding to atomic bonds in both MAPbI$_3$ and MAPbBr$_3$. This aligns well with the results reported by Gehrmann et al. [136]. Their work demonstrated that the spatial correlation in the so-called disorder potential of CsPbBr$_3$, CsPbI$_3$, and MAPbI$_3$ is also limited to short distances, resembling the correlation observed in classical inorganic semiconductors [231]. Furthermore, it is intriguing that both MAPbI$_3$ and MAPbBr$_3$ exhibit nearly identical (normalized) correlation lengths of TB energies (this holds across the entire temperature span of 200-350 K). This indicates that the (normalized) spatial extent over which disorder-induced variations in the electronic structure influence neighboring atoms is akin in both materials. Consequently, the fundamental mechanisms underpinning disorder exhibit comparability between these two substances, notwithstanding potential differences in the extent of temperature-dependent dynamic disorder, as previously discussed.

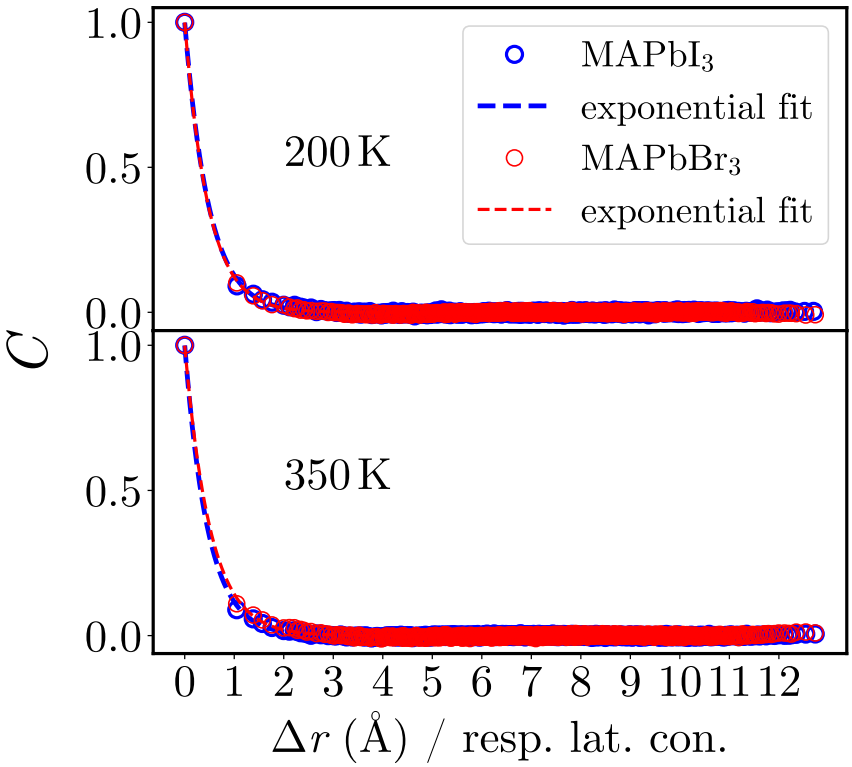

Figure 3.24: Spatial autocorrelation functions of I/Br onsite energies in MAPbI/Br_3 supercells at 200 and 350 K.

To sum up, the contrasting anharmonic vibrational tendencies of $MAPbI_3$ and $MAPbBr_3$ offer an opportunity to assess the influence of this phenomenon on the electronic structure and carrier dynamics at finite temperatures.

3.8 Supercell Band Gap Behavior of HaPs

Having investigated manifestations and connections between dynamic disorder and anharmonicity in $MAPbI_3$ and $MAPbBr_3$, we continue with the calculation of optoelectronic properties with the help of the multi-scale TB model. We begin by analyzing the thermal behavior of the band gap for the MAPbI/Br_3 $16 \times 16 \times 16$ supercells. As elaborated before, the band gap plays an important role in shaping the electronic, optical, and thermal characteristics of semiconductors. For example, it directly influences the functional characteristics of materials used in solar cells, particularly with regard to their efficiency.

3.8.1 Band Gap Distributions

We conduct *NVT*-production runs lasting 50 ps each, using FF MD, across temperatures of 200, 230, 250, 300, and 350 K. During these production runs, snapshots are extracted at 50 fs intervals, resulting in 1000 snapshots for each perovskite type and temperature. For all of these snapshots, we apply our multi-scale TB model. This

delivers us onsite and overlap energies for all the Pb, X atoms, and all the Pb-X bonds, respectively, as well as SOC energies. From these energies, we build a TB Hamiltonian, i.e., a matrix of dimensions $16 \cdot 16 \cdot 16 \cdot 26 \times 16 \cdot 16 \cdot 16 \cdot 26 \approx 10^{10}$ in which we insert the TB energies in the basis of the respective orbitals. A matrix of this dimension can be computationally demanding. However, it is important to emphasize that this matrix is sparse, with only approximately $4 \cdot 10^5$ non-zero entries, which allows for efficient computational treatment (the TB matrix has a sparsity of approximately 99.996 %). Interestingly, the **k**-point dependence of this matrix only emerges from periodic replicas of X-atoms at the border of the supercell, which are projected "outside" the supercell at $\mathbf{R}_S = (0, 0, 0)$, and therefore carry a factor $e^{i\mathbf{kR}} \neq 1$. For computing the electronic structure, this matrix is then diagonalized, and we extract the band gaps at the Γ-point.

The respective probability distributions are shown in Fig. 3.25 together with skewed Gaussian fits, as described in Section 2.10. The first observation is that the distributions of $MAPbI_3$ and $MAPbBr_3$ are relatively narrow (small width), implying that the electrons in the real, distorted material require similar energies for the transition from the valence to the conduction band. This is closely related to the Urbach energy. The Urbach energy, also known as the Urbach tail or Urbach edge, is a parameter used to describe the width of the tail in the absorption edge of a semiconductor material's optical absorption spectrum [232–234]. More technically, the absorption coefficient α can be described by the exponential law

$$\alpha(\hbar\omega) \propto e^{\frac{\hbar\omega - E_g}{E_U(T)}}, \tag{3.11}$$

where $\hbar\omega$ is a photon energy, E_g the band gap energy and $E_U(T)$ the temperature-dependent Urbach energy. A small Urbach energy thus means a steeper increase in the absorption coefficient. As a consequence, a thin layer of the respective semiconductor material is able to absorb a high percentage of incoming photons. Conversely, a broader band gap distribution can result in an increased variety of localized states in the possible band gap energy range, ultimately contributing to a broader Urbach tail in the optical absorption spectrum. This means that a wider distribution of band gaps serves as an indicator of higher Urbach energy. Returning to our observation of narrow band gap distributions in $MAPbI/Br_3$, it is evident that both materials hold promise for use in solar cells. This is because a small Urbach energy signifies that the absorption of photons with energies close to the respective band gap is very precise and efficient.

Yet, we notice that with increasing temperature, the width of the distributions for both compounds increases. This suggests greater disorder and variability in the material's composition, structure, and electronic properties. This agrees well with the dynamic disorder and anharmonicity behavior we investigated in Section 3.7. Besides, a wider band gap distribution can affect the transport of electrons and holes. The broader range of energy levels available for carrier transitions can lead to more frequent scattering events, which, in turn, might reduce carrier mobility and overall conductivity (which will be investigated in Section 3.9).

The biggest difference between $MAPbI_3$ and $MAPbBr_3$ is that for all temperatures,

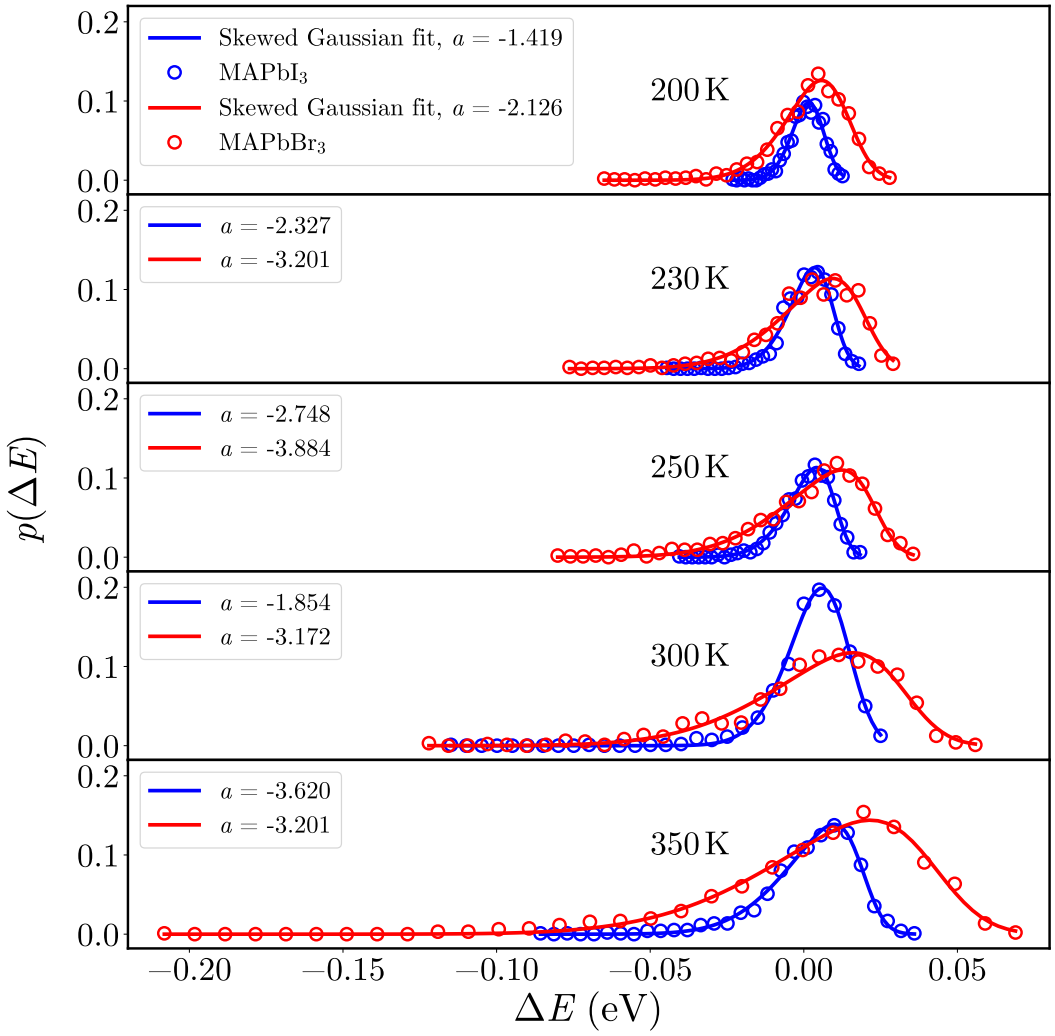

Figure 3.25: Band gap distribution for MAPbI/Br$_3$ 16 × 16 × 16 supercells at various temperatures. The mean value of each distribution is set to zero in all plots for better comparability. To normalize the histograms, we divide each value in the plot by the total number of data points.

the band gap distribution of MAPbBr$_3$ is wider than the one of MAPbI$_3$. Therefore, we can conclude that MAPbBr$_3$ exhibits larger Urbach energies than MAPbI$_3$. This observation aligns well with experimental findings [25]. Furthermore, the observation that the Urbach energy arises from effective vibrational disorder over a short length scale, which increases with rising temperature as seen in our band gap distributions, is in line with findings from Refs. [5, 136, 231].

Since we use skewed Gaussians as fit functions, we also calculate the skewness parameter a (see Section 2.10). The distributions for both compounds display a left-skewed pattern, indicating a higher probability of states with lower-energy band gaps compared to those with higher energies. This observation can have implications for the design of solar absorber devices based on HaPs. Notably, the skewness tends to become more pronounced at higher temperatures for both MAPbI$_3$ and MAPbBr$_3$.

3.8.2 Temperature Dependence of the Band Gaps

Additionally, we have conducted calculations to ascertain the temperature-dependent behavior of the average supercell band gaps. The observed trend is presented in Fig. 3.26. The size of the bars in the plot illustrates the standard deviations of the respective band gap distributions. Evidently, these magnitudes progressively enlarge with rising temperatures, thus corroborating the conclusions drawn in the preceding section. Remarkably, our observations indicate a decline in the band

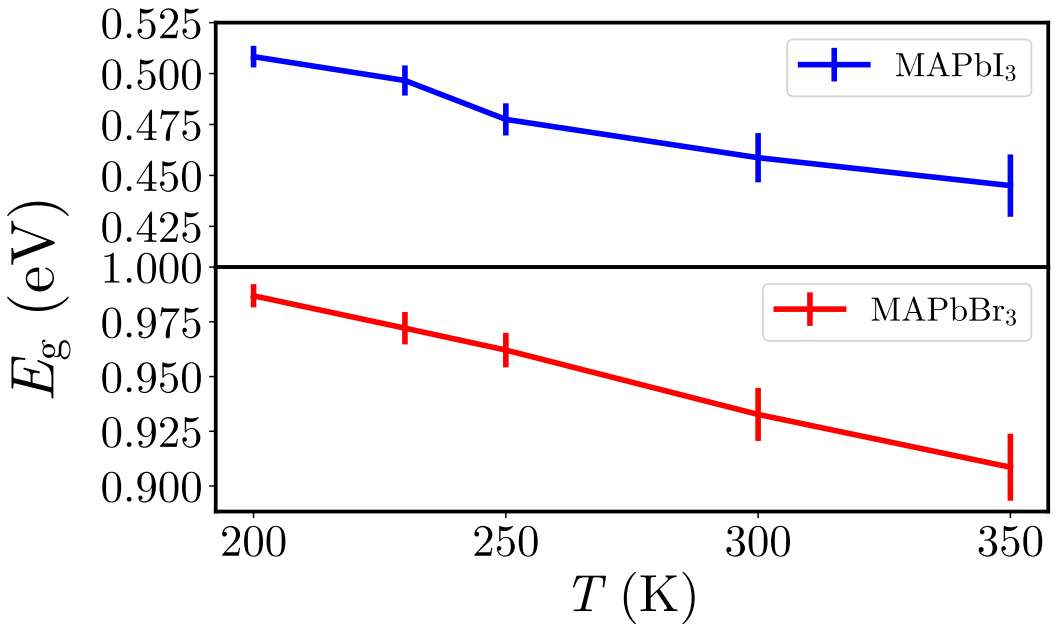

Figure 3.26: Temperature-dependent variations of the band gaps of the $16 \times 16 \times 16$ $MAPbI_3$ and $MAPbBr_3$ supercells.

gap values with increasing temperature for both compounds. This contrasts with experimental [235] and theoretical findings [189]. Still, as previously discussed, significant shifts in the temperature dependence of the band gap can arise when higher-order couplings are introduced in theoretical frameworks. Research by Seidl et al. [151] underscores the key role of anharmonicity in this context. Although their study pertains to the perovskite $CsPbBr_3$, the concept of dynamic disorder applies equivalently. Specifically, Seidl et al. demonstrate an anomalous, non-physical discontinuity in the band gap magnitude during the orthorhombic-to-cubic phase transition (skipping the tetragonal range, which only occurs over a short temperature range) when employing the Monte Carlo method, which lacks the incorporation of higher-order coupling terms. Conversely, they achieve a closer alignment with experimental findings when directly extracting the band gap from first-principles MD, as this method inherently takes into account the effects of anharmonicity.

3.9 Charge Carrier Mobilities

After the investigation of the band gaps, we now aim to establish a link between the dynamic disorder behavior of $MAPbI/Br_3$ and their respective charge transport characteristics across various temperatures. To achieve this, we perform quantum-dynamical simulations using the mixed quantum-classical Ehrenfest dynamics of Ref. [5] as explained in Section 2.8.

We begin with computing initial Wannier functions that represent either holes or electrons. These Wannier functions are generated through our TB model and `Wannier90`. The quantum dynamics are executed with the help of the semiclassical Ehrenfest approach, which conveniently omits the consideration of back-reaction forces exerted upon the lattice. Back-reaction forces emerge when the potential landscape exerts a force on a charge carrier. In response, the charge carrier exerts an equal force on the lattice in the opposite direction. Their neglect is justified because we treat the electronic and nuclear degrees of freedom separately and consider the influence of back-reaction forces on carrier scattering minimal. Our quantum-dynamics calculations are conducted on a $96 \times 96 \times 96$ real-space supercell made of $MAPbI/Br_3$ unit cells at a certain temperature.

The construction of initial Wannier functions requires the computation of the TB Hamiltonian's eigenvectors and eigenvalues at the band edges of $MAPbI_3$ and $MAPbBr_3$ cubic unit cells. This is done for an evenly spaced $8 \times 8 \times 8$ $\mathbf{k}$-point grid. Subsequently, we calculate the overlap matrix $M_{mn}^{(\mathbf{k},\mathbf{b})}$ as well as the projection $A_{mn}^{\mathbf{k}}$ of the eigenvectors onto trial orbitals, as explained in section 2.5. These two inputs are used to compute maximally localized Wannier functions (MLWFs) via `Wannier90`. For this, we first determine the unitary rotation matrix $U_{mn}^{\mathbf{k}}$, the most important component for the subsequent calculation of MLWFs on an $8 \times 8 \times 8$ real-space grid. Mathematically, the MLWFs, $\psi_{n\mathbf{R}}(\mathbf{r})$, are calculated according to the expression

$$\psi_{n\mathbf{R}}(\mathbf{r}) = \frac{1}{(2\pi)^3} \int \left[\sum_m U_{mn}^{\mathbf{k}} u_{m\mathbf{k}}(\mathbf{r}) \right] \mathrm{e}^{\mathrm{i}\mathbf{k}\mathbf{R}} \, \mathrm{d}\mathbf{k}, \tag{3.12}$$

where $u_{m\mathbf{k}}$ are the eigenvectors of the TB Hamiltonian (cf. Equation 2.118) and the integral runs across all $\mathbf{k}$-points of the $8 \times 8 \times 8$ $\mathbf{k}$-points grid. The volume V does not matter here since the Wannier Functions are normalized when propagated in time. Every point $\mathbf{R}$ of the real-space grid contains 26 entries for the Wannier function, encompassing 13 orbitals while accounting for spin. This $8 \times 8 \times 8$ real-space supercell configuration initializes the charge carrier quantum dynamics. For this, we put the MLWFs at the center of the $96 \times 96 \times 96$ real-space grid. This substantial supercell size has been selected to mitigate border effects and undesired reflections, ensuring the accuracy of the simulations. Subsequently, we subject them to propagation using the quantum mechanical time evolution operator, as outlined by Equation 2.167.

To be precise, we use two MLWFs each for $MAPbI_3$ and $MAPbBr_3$: one capturing the valence band characteristics, representing holes, and another for the conduction band, symbolizing electrons. They are propagated in time via the Taylor expansion of the quantum mechanical propagator. The most important tool for the propagation

is TB Hamiltonians, which are computed for a 100 fs FF MD *NVT* production run of the $16 \times 16 \times 16$ supercells. The chosen time step Δt for our quantum dynamics simulations is set to 1 fs. For that reason, we compute 100 distinct TB Hamiltonians for 100 MD snapshots. The parameter C in Equation 2.167 is set to 50.

A schematic visualization of the time evolution of Wannier functions with the help of TB Hamiltonians is shown in Fig. 3.27. For each term of the Taylor expansion of the time propagator, an update is applied to the Wannier function, as described in Equation 2.167. This update involves the multiplication of the corresponding components of the Wannier function, localized on specific orbitals, by the relevant onsite, overlap and SOC energies that influence them. To illustrate, consider adjusting the Wannier function component located on a Pb s orbital. This encompasses adding the product obtained by multiplying the pertinent $t_{\mathrm{sp}\sigma}$ value for the particular bond with the component of the Wannier function located on the adjacent I p orbitals. Furthermore, it is noteworthy that this summation element undergoes a subtraction when the phases of the s orbitals align with the phases of the overlapping lobe of the neighboring p orbital. To make the $16 \times 16 \times 16$ TB Hamiltonian cover the whole $96 \times 96 \times 96$ wavefunction grid, we periodically replicate the TB Hamiltonian.

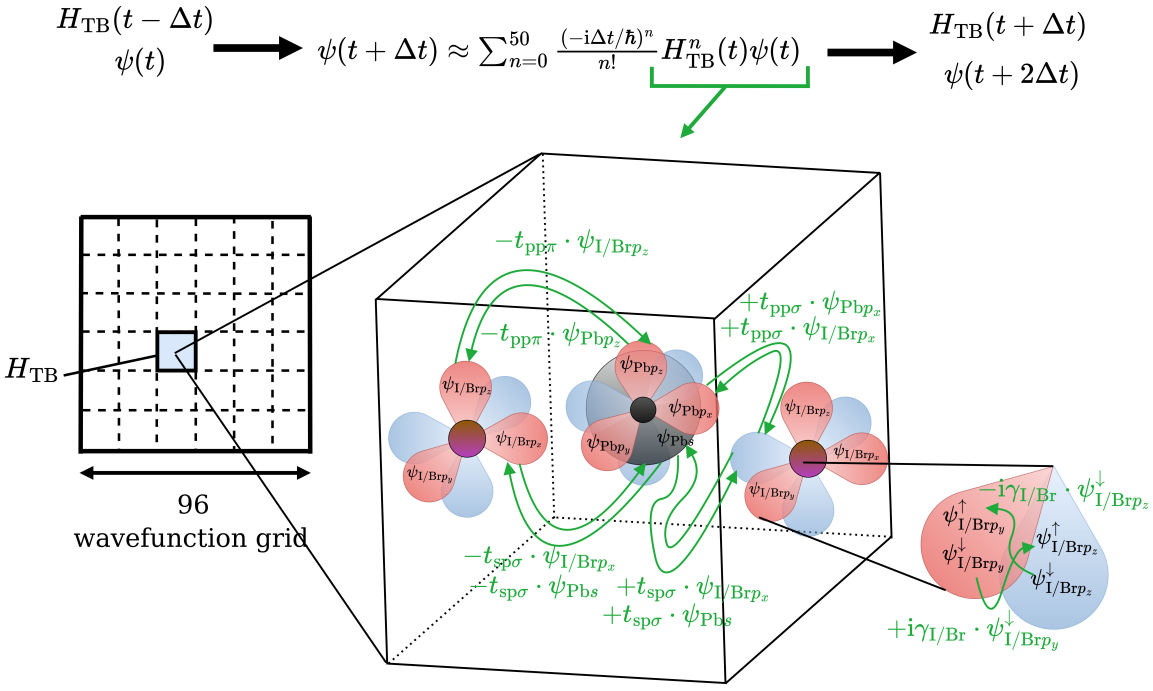

Figure 3.27: Illustration of the temporal evolution of Wannier functions over time using TB Hamiltonians. A Wannier function $\psi(t)$ is provided as input to an algorithm that propagates it through time via a Taylor expansion of the quantum mechanical propagator. The evolution of the Wannier function is achieved by updating it with the corresponding onsite, overlap, and SOC values encapsulated in the product $H_{\mathrm{TB}}(t)\psi(t)$. This concept is visualized for selected overlap and SOC values in an exemplary unit cell.

After propagating electron and hole Wannier functions for 100 fs, we continue with the computation of the MSD of the charge carriers, drawing upon the theory outlined in Section 2.8. This is an important step that ultimately enables us to obtain the charge carrier mobilities. This process is facilitated through the utilization of Equation 2.168, where the expression $D = \lim_{t\to\infty} \mathrm{MSD}(t)/6t$ can be interpreted as the slope of the MSD (under the condition that the time parameter t is selected sufficiently large).

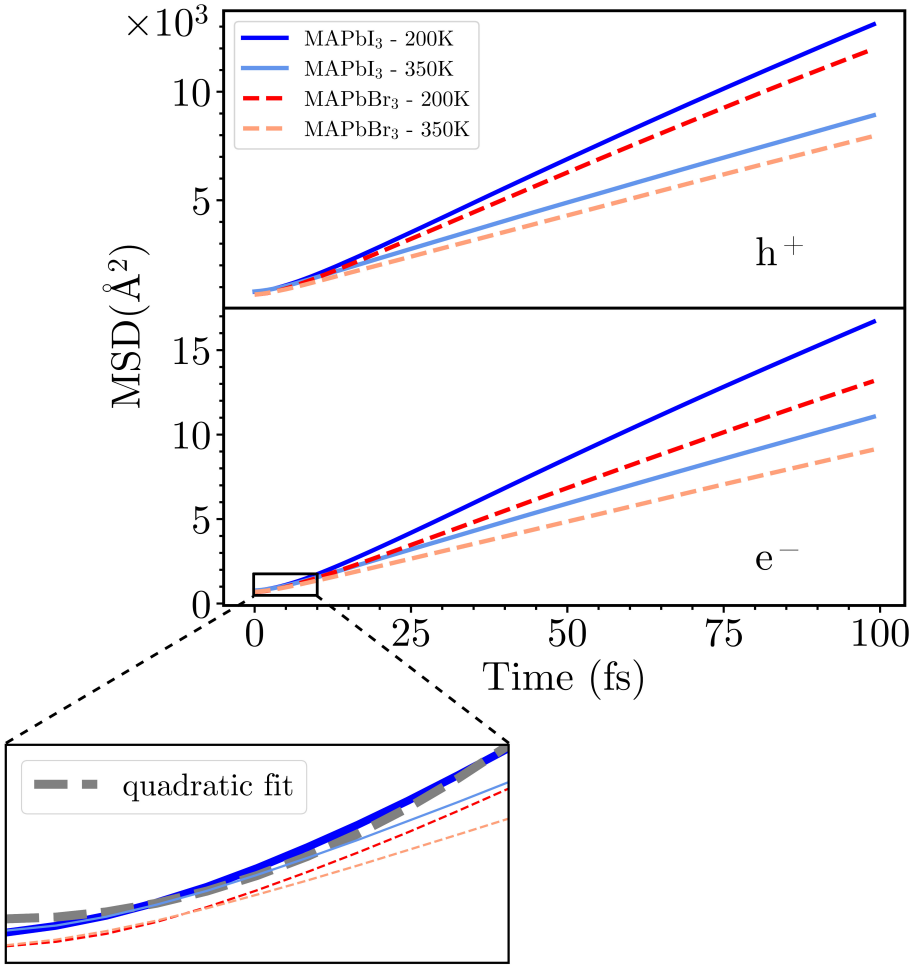

Figure 3.28: Mean-squared displacements of holes (h^+, upper panel) and electrons (e^-, lower panel) for $MAPbI_3$ and $MAPbBr_3$ at 200 K and 350 K. After a brief period of nearly ballistic behavior (where the mean squared displacement increases slightly shallower than quadratically with time for approximately 10 fs, see the inset in the bottom panel, which shows a quadratic fit to the electron transport in $MAPbI_3$), the transport transitions into the regime of diffusive carrier transport, characterized by a linear time dependence.

The computation of the MSD and the mobilities unfolds as follows: A total of 64 positions in the $16 \times 16 \times 16$ sublattice are considered for the TB Hamiltonian (with periodic movement in this sublattice). Subsequently, the mean mobility values are

ascertained by averaging over the 64 outcomes for the MSD at a given temperature. A concrete illustration of one of these 64 quantum mechanical simulations is shown in Fig. 3.28, where we present an exemplary MSD for holes and electrons at temperatures of 200 K and 350 K. In a purely ballistic transport regime devoid of notable scattering, the MSD would follow a quadratic relationship with time, expressed as MSD $\propto t^2$. In fact, for approximately the first 10 fs, we observe a nonlinear behavior of the MSD with time, slightly shallower than quadratic behavior (as exemplified in the inset of the bottom panel of Fig. 3.28 for electron transport in $MAPbI_3$ at 200 K) for both compounds and all temperatures. This suggests that there are some minor scattering events leading to a deviation from ideal ballistic transport. After this initial period of 10 fs, there is a transition to diffusive behavior. In the diffusive regime, the MSD exhibits a linear relationship with time, described by a $\mu \propto Dt$-law. This indicates that random scattering and collisions play a key role in the charge carrier transport. Notably, as the temperature rises from 200 to 350 K, there is an increase in the slope of the respective curves in the diffusive regime.

To provide a more vivid depiction of the spatial propagation of a Wannier function, we present in Fig. 3.29 a two-dimensional projection showing the expansion of a conduction-band Wannier wave packet. Specifically, this projection displays the spatial distribution of the Wannier wave packet at two distinct time points: 5 fs and 90 fs, at a temperature of 200 K. The values for $|\psi|^2$ have been computed for each unit cell within the supercell, involving the summation of density values from the Wannier function components that are localized on the respective Pb s, Pb p and X p orbitals. From this, we can see that the propagation happens isotropic across the material, i.e., the evolution of the wavefunction is uniform in all directions.

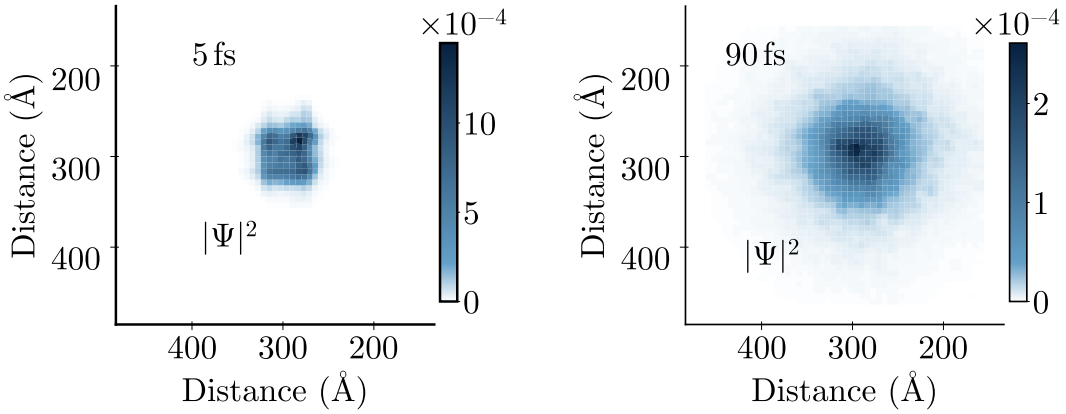

Figure 3.29: Spatial time evolution of the charge carrier probability density in $MAPbI_3$ at a temperature of 200 K at 5 fs (left panel) and 90 fs (right panel). We present a two-dimensional cross-section of the three-dimensional evolving Wannier function. The figure on the title page of this work shows a three-dimensional plot of the right panel with a different color scheme.

Upon completing 64 simulation runs at each temperature from 200 to 350 K, we calculate the average carrier mobilities for both $MAPbI_3$ and $MAPbBr_3$. These calculations specifically pertain to the diffusive regime, and we determine the mobilities by analyzing the slope of the corresponding MSD while disregarding the short-lived ballistic regime. The resulting carrier mobilities are presented in Fig. 3.30, categorized for holes and electrons (Fig. 3.30a and b). For comparability, it is standard practice to calculate the combined mobility by adding the mobilities of both holes and electrons. This summation is depicted in Fig. 3.30c. The combined mobility will also be the focus of our analysis in what follows.

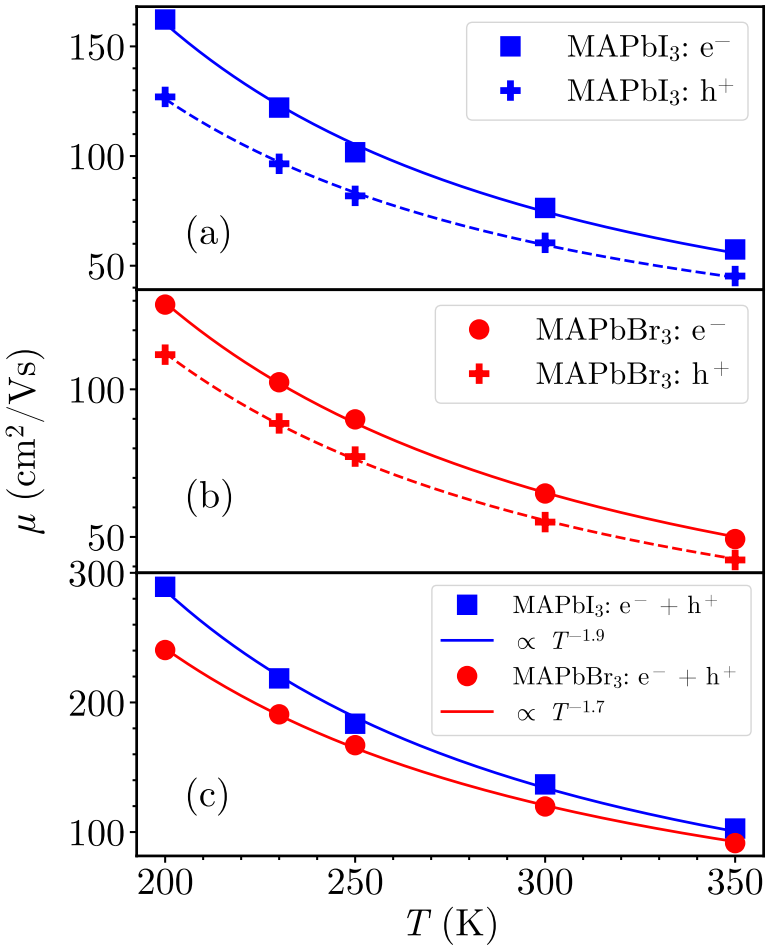

Figure 3.30: Temperature-dependent carrier mobilities of electrons and holes in $MAPbI_3$ (a) and $MAPbBr_3$ (b). Panel (c) shows the sum of hole and electron mobilities for the two compounds. The lines represent the best fit to the respective power-law behaviors.

First, Fig. 3.30a and b confirm the prevalent consensus that electron mobilities exceed hole mobilities in $MAPbI_3$ and $MAPbBr_3$ [101]. Additionally, within the temperature range where $MAPbBr_3$ displays more pronounced anharmonicity compared to $MAPbI_3$ (200-300 K, as shown in Fig. 3.25), the temperature dependence of the $MAPbBr_3$ mobility is flatter than for $MAPbI_3$, with also lower magnitudes. As the temperature rises, resulting in increasingly anharmonic displacements in $MAPbI_3$,

the two curves draw nearer, and the temperature dependencies become more alike. This process culminates at a point at 350 K, where the carrier mobilities of both compounds become comparable owing to their cubic phase nature (at 300 K, $MAPbI_3$ was still in tetragonal phase) and the associated similarly anharmonic atomic dynamics (as illustrated in Fig. 3.22).

The temperature-dependent mobilities can be characterized using a power law, as demonstrated by the fits in Fig. 3.30c. Despite the plethora of methods employed in experimental studies for sample fabrication and characterization, yielding different results, our observed temperature dependencies generally align with experimental findings [101, 116, 194–199, 236, 237]. This agreement also extends to the order of mobility magnitudes, even though exact alignment cannot be expected due to the approximations of our calculations. We would like to draw particular attention to the room-temperature observations: Here, the mobility magnitudes and the greater conductivity of $MAPbI_3$ compared to $MAPbBr_3$, are in good agreement with recent experimental studies [238], underscoring our model's ability to encompass the carrier scattering mechanisms that govern the charge transport behavior in $MAPbI_3$ and $MAPbBr_3$.

We conclude this section by mentioning that there exists a theoretical model from 1977 [239], which marked the first time incorporating both site diagonal and nearest-neighbor off-diagonal dynamic disorder in a system to calculate the motion of a particle and its diffusion constant. This model established a relationship of the form $\mu \propto a + bT^{-2}$, where the constants a and b are material-specific. This relation also aligns well with the diverse behaviors observed in experimental studies of HaPs. In a similar way, a recent study by Lacroix et al. [206] presents a different dynamic disorder model for HaPs. Their research indicates room-temperature mobilities of similar magnitudes to our findings, demonstrating an approximate $\mu \propto T^{-3/2}$ relationship at high temperatures, which once again aligns with experimental observations. Furthermore, their model underscores the significance of static and dynamic disorder, emphasizing that the Boltzmann transport formalism tends to overlook localization effects. Moreover, they highlight that the formation of polarons is mitigated by scattering-induced energy broadening, further emphasizing the limited impact of polaronic effects around room temperature.

3.10 Spectral Analysis

The precise connection between anharmonicity, dynamic disorder, and charge carrier mobilities remains an open question. To address this puzzle, we conduct a statistical analysis of the temperature-dependent atomic and electronic dynamics. A valuable tool for this investigation is the spectral density, which provides insights into the spectral distribution of TB energies. We can compute the spectral densities for both the onsite and overlap terms of the TB model using Equation 2.159. In the context of the TB energies, this equation reads

$$\Phi(\omega) = \int \mathrm{d}t \, \langle \delta t_{ij}(t+s) \delta t_{ij}(s) \rangle_s \, \omega \cdot \mathrm{e}^{-\mathrm{i}\omega t}. \tag{3.13}$$

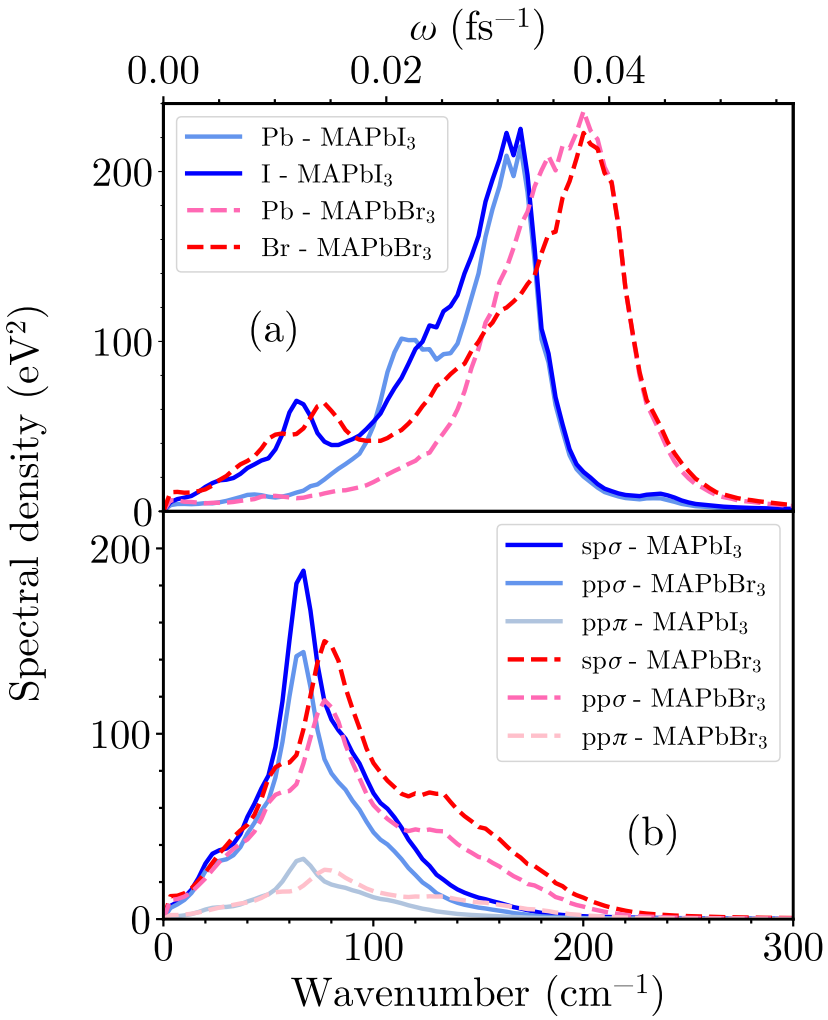

Figure 3.31: Spectral densities of onsite (panel a) and overlap (panel b) terms of the TB model at 300 K for $MAPbI_3$ and $MAPbBr_3$. Both panels show the low-frequency region of the spectra.

Here, δt_{ij} represents the time-fluctuating deviation of an energy contribution from a TB Hamiltonian's mean value. The term $\langle \delta t_{ij}(t+s)\delta t_{ij}(s)\rangle_s$ signifies the temporal autocorrelations of energy fluctuations for a lag time t, with averaging carried out across all possible times s. In Fig. 3.31, we provide the spectral densities for all the onsite and overlap energies, which were extracted from 10 ps FF MD simulations. Particularly noteworthy is the observation that the curves corresponding to different onsite and overlap terms, respectively, exhibit remarkably similar shapes. However, they vary in magnitude, indicating that their behavior aligns in the frequency domain, yet they demonstrate differing degrees of intensity fluctuations over time.

We also compare the spectral densities obtained from the 10 ps MD simulation and those from a 50 ps MD simulation (see Fig. 3.32). The longer 50 ps trajectory produces nearly identical results for the spectral densities, mirroring what was demonstrated for the VDOS in Fig. 3.21. Thus, due to the substantial size of the supercell, a 10 ps simulation duration is sufficient for obtaining statistically converged quantities.

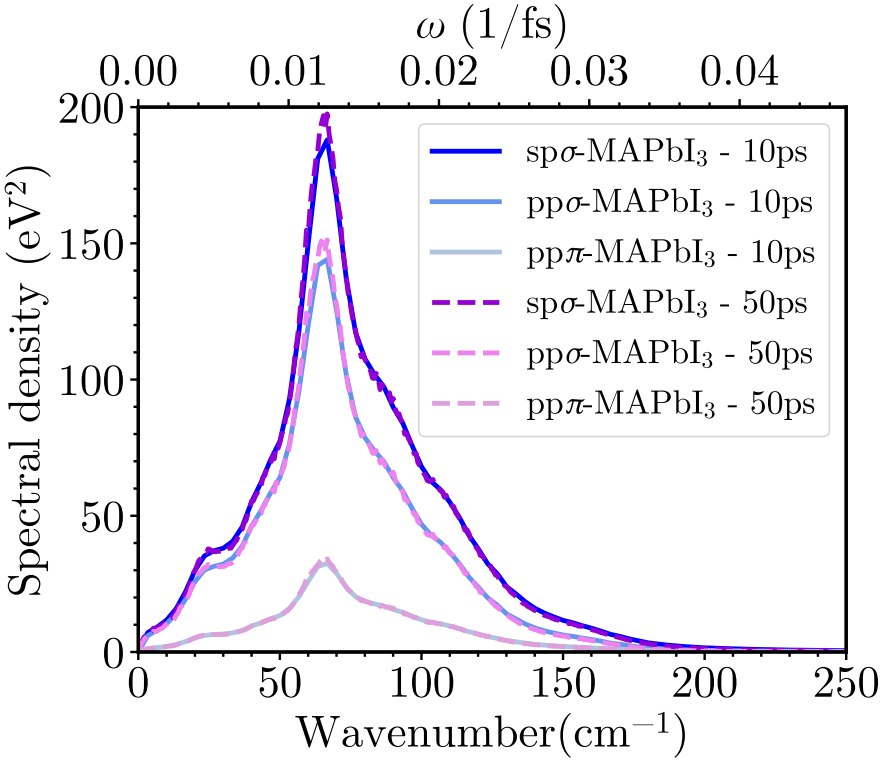

Figure 3.32: Spectral densities of overlap terms in the TB model in $MAPbI_3$ at 300 K, extracted from 10 ps and 50 ps FF MD runs (low-frequency region of the spectra).

Up to this point, we have exclusively presented the low-frequency regions of the spectra. In Fig. 3.33, we revisit the spectral densities of onsite energies for both compounds. Since the onsite energies are also influenced by electrostatic interactions with carbon, nitrogen, and hydrogen atoms, which undergo vibrations at higher frequencies, the spectral densities of the TB energies naturally encompass contributions from these higher frequencies. However, we refrain from investigating these high-frequency contributions since they hardly impact the conduction and valence bands and, thus, the band gap.

It is worth noting that our subsequent analysis will unveil the dominance of the ppσ term concerning carrier scattering. As a result, our primary focus is on this particular parameter. To establish a link between spectral densities, anharmonicity, and dynamic disorder, we directly compare the spectral density of the ppσ term and the onsite energies of the I/Br atoms with the VDOS, as shown in Fig. 3.34. As previously observed in Fig. 3.15 for DFT-based MD and in Fig. 3.21 for FF MD, the VDOS at 300 K (see Fig. 3.34a) exhibits noticeable contributions in the THz range for both compounds. Furthermore, we detect a subtle frequency shift towards higher values in the VDOS spectrum of $MAPbBr_3$.

We proceed to draw a comparison between these observations and the spectral

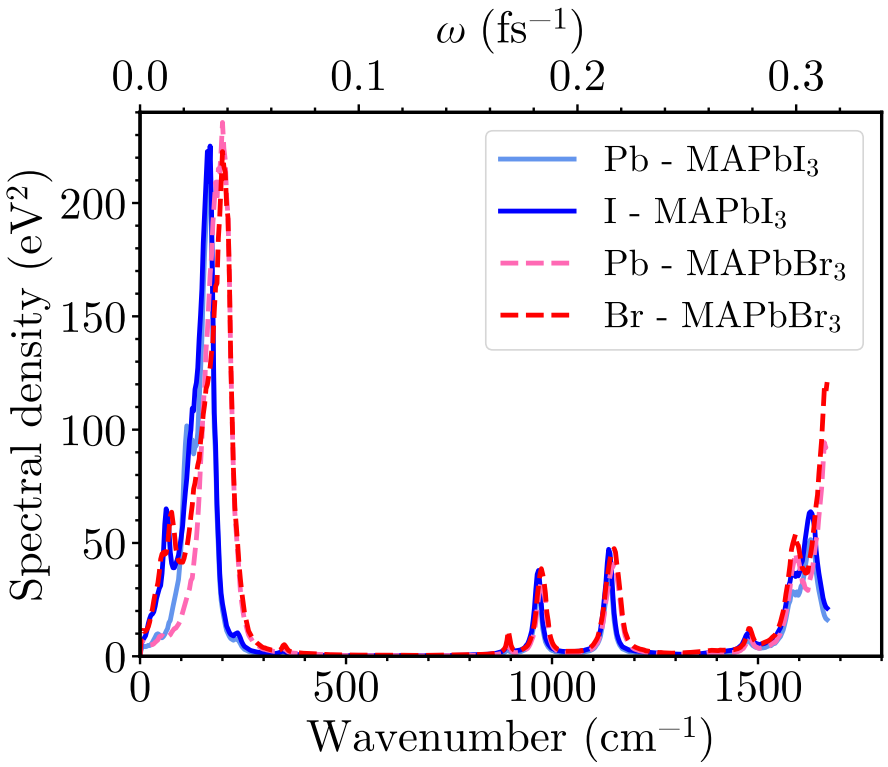

Figure 3.33: Spectral densities of onsite terms of the TB model at 300 K for $MAPbI_3$ and $MAPbBr_3$. The higher frequency contributions arise from the interactions of the Pb and I/Br atoms with the C, N and H atoms.

densities of onsite and overlap fluctuations, as shown in Fig. 3.34b and c. Notably, the fluctuations of the $t_{pp\sigma}$ overlap term occur in a low-frequency range similar to the VDOS (see Fig. 3.34a and c). We also observe a parallel shift towards higher frequencies in the $t_{pp\sigma}$ fluctuations for $MAPbBr_3$, mirroring the trend from the VDOS. Consequently, the fluctuations of the $t_{pp\sigma}$ term closely align with the respective VDOS in both compounds. The standard deviations of these $t_{pp\sigma}$ fluctuations measure 0.21 eV for $MAPbI_3$ and 0.23 eV for $MAPbBr_3$ at 300 K. This suggests that the fluctuations are stronger in the inherently more anharmonic $MAPbBr_3$, further affirming that the increased anharmonicity in $MAPbBr_3$ contributes to heightened dynamic disorder. However, as previously mentioned, it is also important to note a gradual increase in disorder with rising temperatures in both compounds. This phenomenon finds further support in the spectral densities at 200 and 350 K, as illustrated in Fig. 3.35. Here, we observe a noticeable increment in the cumulative area under the respective spectral density curves when transitioning from 200 to 350 K (for simplicity, we omit the gradual progression across intermediate temperatures in Fig. 3.35). This trend indicates increasingly pronounced fluctuations in the TB energies with rising temperatures for both compounds. Consequently, it seems reasonable to infer that heightened fluctuations, signifying increased dynamic disorder and stronger anharmonicity, contribute to the previously discussed reduced mobilities.

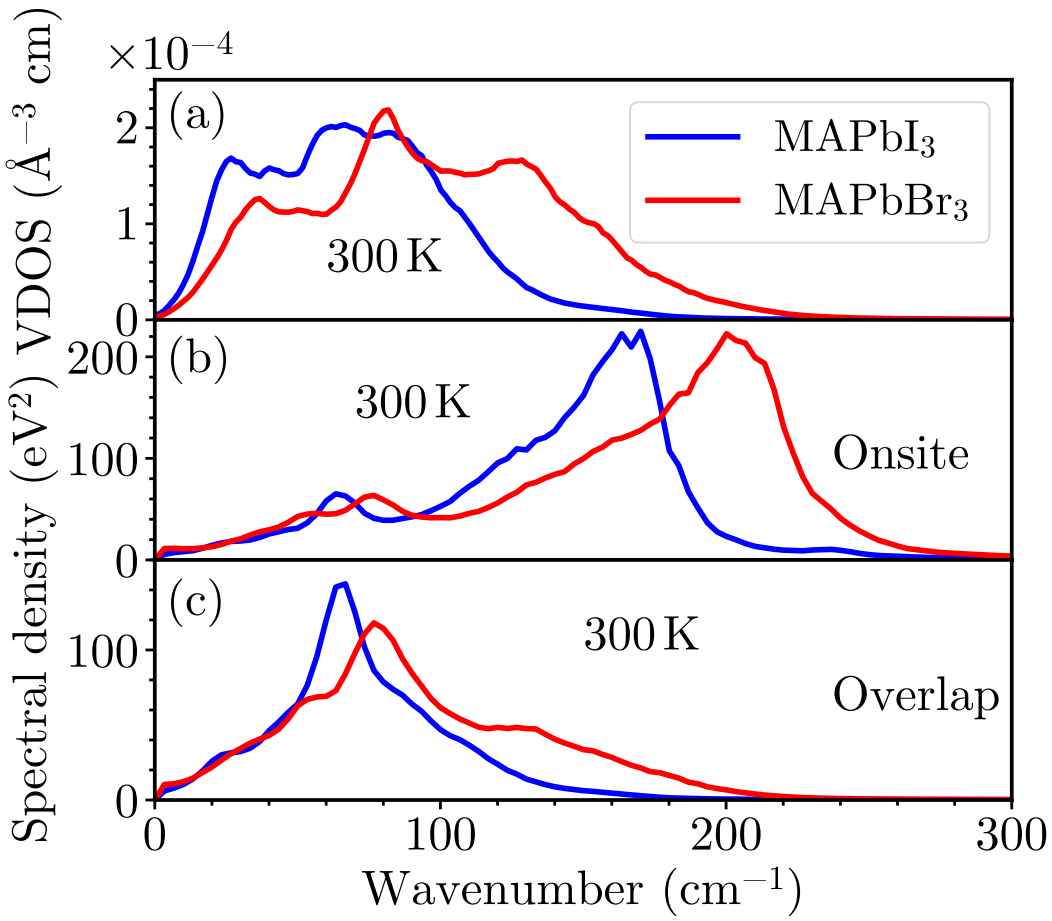

Figure 3.34: VDOS (panel a) and spectral densities of onsite (panel b) and the $t_{pp\sigma}$ overlap-terms (panel c) at 300 K (low-frequency region of the spectra).

An alternative and plausible explanation for the differences in charge carrier mobilities of $MAPbI_3$ and $MAPbBr_3$ may stem from the subtle yet noticeable frequency shift observed in $MAPbBr_3$ compared to $MAPbI_3$. This difference becomes apparent not only in the VDOS but also in the spectral densities, suggesting the need for a more in-depth investigation.

3.11 Influence of Energy Fluctuations on Carrier Dynamics

Before examining the disorder-induced energy fluctuations in more detail, we try to elucidate the temperature-dependent mobility behavior presented in Fig. 3.30c through a purely electronic structure approach, following the principles of the large-polaron model. This involves the traditional momentum-space quasiparticle description of the charge carriers. To achieve this, we compute the static crystal structures and effective masses for both the tetragonal and cubic phases in $MAPbI_3$ and $MAPbBr_3$. Specifically, we again perform DFT calculations using `VASP`, employing 200 **k**-points distributed equally between high-symmetry points. By fitting the band structures at the respective CBM and VBM for both the tetragonal and cubic phases

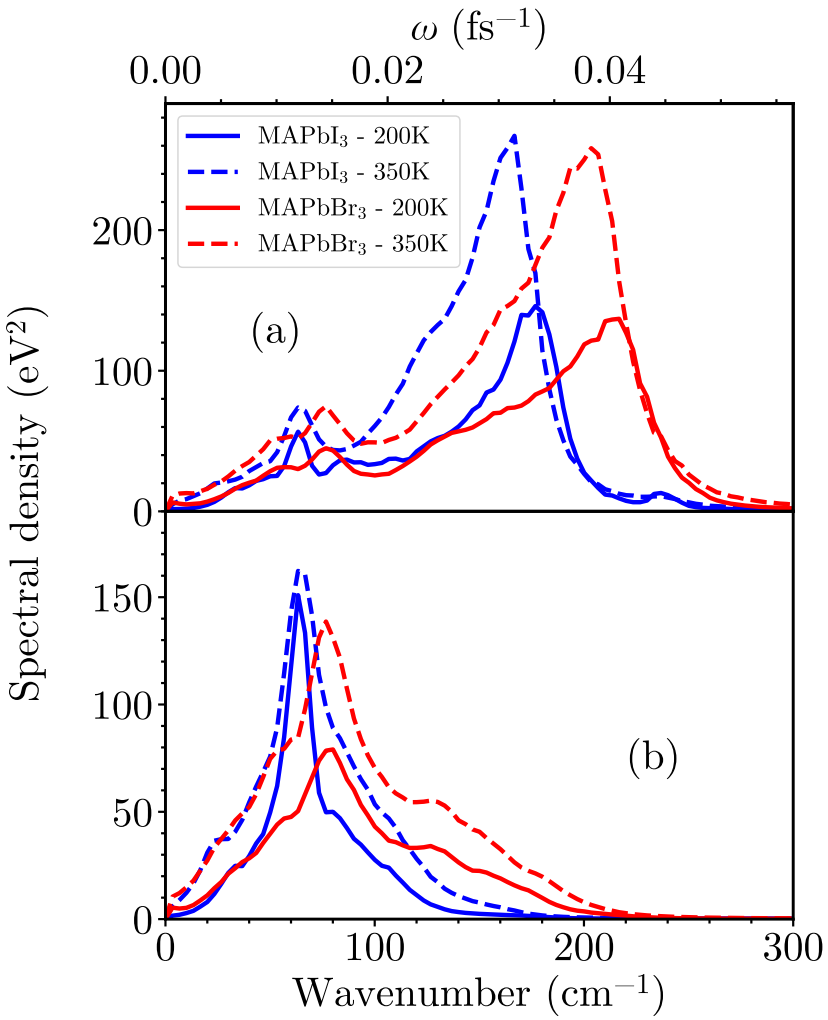

Figure 3.35: Spectral densities of onsite (panel a) and the $t_{pp\sigma}$ overlap-terms (panel b) at 200 K (dashed lines) and 350 K (solid lines). Again, both panels show the low-frequency region of the spectra. As one can see, increasing the temperature leads to a raised area under the respective curve, indicating stronger fluctuations of the respective energy term.

with a parabolic model while excluding the linear term, we obtain effective masses, which are reported in Table 3.2. The cubic-phase masses are assessed along the R $\rightarrow$ Γ-**k**-point path, whereas the tetragonal phases are analyzed in the $\Gamma \rightarrow$ X direction.

As observed, the effective masses of $MAPbI_3$ generally exhibit lower values compared to those of $MAPbBr_3$, in agreement with the findings of previous studies [24, 106, 240–247]. Consequently, this observation provides a plausible explanation for the observed trend of higher charge carrier mobilities in $MAPbI_3$ compared to $MAPbBr_3$ at temperatures up to approximately 300 K. This alignment with the Drude model and traditional transport theory, wherein charge carrier mobility is directly proportional to the effective mass of the charge carriers, lends further support to this explanation.

Table 3.2: Effective masses of electrons and holes in tetragonal and cubic phases of $MAPbI_3$ and $MAPbBr_3$, expressed as multiples of the electron mass (m^*/m_e).

$MAPbI_3$			$MAPbBr_3$		
charge carrier	tetragonal	cubic	charge carrier	tetragonal	cubic
h^+	0.19	0.11	h^+	0.18	0.16
e^-	0.14	0.09	e^-	0.16	0.13

However, an intriguing pattern emerges upon closer examination of the relative differences in effective masses between the two compounds during the tetragonal-to-cubic phase transition. When we sum the effective masses for both holes and electrons and calculate the ratio between $MAPbI_3$ and $MAPbBr_3$ for these sums, we find in the tetragonal phase that

$$\frac{m_{\mathrm{I}}^*}{m_{\mathrm{Br}}^*} = \frac{0.19 + 0.14}{0.18 + 0.16} \approx 0.97 \tag{3.14}$$

and in the cubic phase,

$$\frac{m_{\mathrm{I}}^*}{m_{\mathrm{Br}}^*} = \frac{0.11 + 0.09}{0.16 + 0.13} \approx 0.69. \tag{3.15}$$

Remarkably, this analysis reveals that the relative differences in effective masses between the two compounds are significantly more pronounced in the cubic phase compared to the tetragonal phase. This finding stands in stark contrast to the mobility trend depicted in Fig. 3.30c.

Hence, we conclude the effective masses prove insufficient in explaining the temperature-dependence of the charge carrier mobilities. This again underscores that a purely momentum-space description of the carriers is not a suitable concept for HaPs. This is because the electronic band structures (from which the effective masses are computed) are the main component for well-established electron-phonon models, employing a perturbative approach to account for finite-temperature effects. Moreover, even in this traditional framework, more open questions exist. To elaborate, when employing band theory and the Boltzmann transport equation [148, 193, 248], the temperature dependencies of the charge carrier mobility are more pronounced at lower temperatures in the lower-symmetry phases of hybrid HaPs. This stands in stark contrast to the results of several experimental investigations [116, 197–199] which indicate a different perspective. According to these studies, the temperature dependencies of the mobility are stronger in high-symmetry phases.

Therefore, we return to the dynamic-disorder framework to understand charge carrier dynamics in HaPs since - in contrast to methodologies rooted in a momentum-space framework and relying on perturbative electron-phonon couplings - it encompasses the complete spectrum of carrier-phonon scattering effects inherent to the semiclassical treatment of finite-temperature atomic motion [1, 5]. To assess the

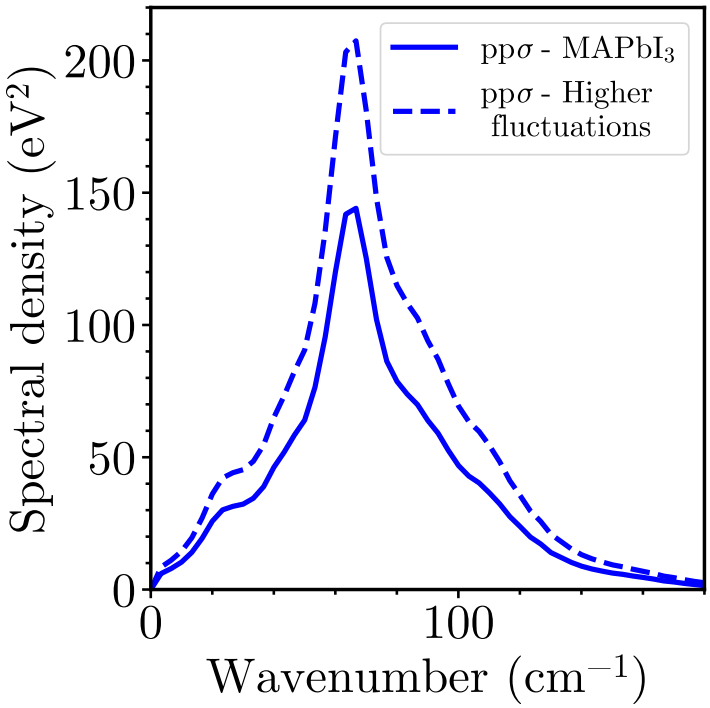

Figure 3.36: Spectral density of $MAPbI_3$ at 300 K ($t_{pp\sigma}$, solid line) compared with an artificial signal (dashed line) for the $t_{pp\sigma}$ spectral density where fluctuations have been manually increased by 20 %. This leads to an increase in the area under the curve.

influence of variations in the strength and frequency of energy fluctuations on charge carrier dynamics, we carry out a series of theoretical experiments, referred to as "gedankenexperiments." Specifically, we create modified on-site and coupling signals that perturb and alter the original TB Hamiltonian. These modifications are applied to the charge carrier dynamics simulations for $MAPbI_3$ at 300 K.

To start, we construct a TB signal with heightened energy fluctuations. To achieve this, we increase the energy values of various TB terms by 0.05 eV when they exceed their mean value and, conversely, decrease them by the same amount when they fall below their mean value. The resulting impact of this manipulation on the spectral density of the ppσ term is illustrated in Fig. 3.36, showing the expected outcome of an increased area under the dashed curve.

We apply this procedure to all the TB terms. For each of them, this results in slightly different relative changes in fluctuations. Interestingly, these changes have a noteworthy impact on the respective mobility values, as illustrated in Table 3.3. Notably, it becomes apparent that enhancing fluctuations consistently results in a decrease in mobility values. This effect is most pronounced in the case of the ppσ energy (a decrease by 20 cm^2/Vs which corresponds to 13 %), underscoring the key role of fluctuations in ppσ interactions for the carrier mobility. The data presented in Table 3.4 corroborates this observation. There, we present mobilities

Table 3.3: Impact of increased fluctuations in the different TB terms on the carrier mobility of $MAPbI_3$ at a temperature of 300 K. Specifically, we report the sum mobilities of electrons and holes.

TB term	Increase of fluctuation	Decrease of mobility
spσ	18 %	4 %
ppσ	20 %	13 %
ppπ	44 %	1 %
Pb s	22 %	1 %
Pb p	22 %	5 %
I p	18 %	7 %

under conditions where we effectively disable energy fluctuations for the respective overlap energies by keeping them constant at their mean values throughout the simulation. Under these conditions, we observe a notable increase in mobility, with the most substantial enhancement occurring in the case of constant ppσ energies.

Table 3.4: Effect of disabling fluctuations in the various TB overlap terms on the carrier mobility of $MAPbI_3$ at 300 K (again sum mobilities of electrons and holes).

Constant TB term	Increase of mobility
spσ	14 %
ppσ	76 %
ppπ	2 %

Equally interesting is the exploration of carrier mobility outcomes when all TB terms, onsite and overlap, are held constant at their respective mean values at the same time. In this scenario, Fig. 3.37 provides an illustrative example of the MSD for electrons in $MAPbI_3$ at 300 K. The quadratic fit aligns remarkably well with the MSD curve, indicating that the charge carrier scattering is rendered completely inoperative. As a result, the electrons exhibit ballistic transport behavior, leading to significantly larger mean square displacements compared to the values from Fig. 3.28. The ballistic transport persists until around the 50 fs-mark, at which point boundary and reflective effects of the $96 \times 96 \times 96$ supercell come into play. This further reinforces the finding that reduced charge carrier scattering has a profound impact on transport, leading to enhanced carrier mobilities. In line with this investigation, we also explore the consequences of deactivating SOC. Upon doing so, the electron mobility at 300 K experiences a noticeable increase of approximately 14%.

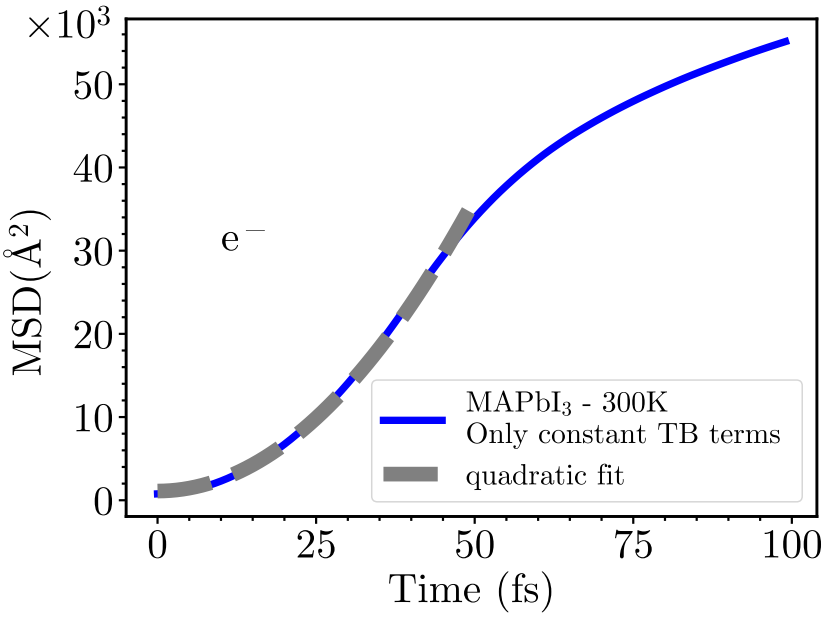

Figure 3.37: Exemplary MSD for electrons in $MAPbI_3$ where all TB energies are kept constant at their respective mean value. The electrons consistently exhibit ballistic transport behavior until approximately 50 fs (seen from the quadratic increase of the MSD with time; see also Fig. 3.28), where border effects start to influence their motion.

After we have investigated the role of energy fluctuations with respect to charge carrier dynamics, we also explore the impact of frequency shifts in the VDOS and ppσ spectral density that arise when comparing $MAPbI_3$ and $MAPbBr_3$. To achieve this, we construct an artificial signal, built as a sum of sinusoidal functions with randomized phases, mimicking the original ppσ spectral density of $MAPbI_3$ at 300 K. This means it preserves the original fluctuations, i.e., reproduces the original standard deviations. We use this artificial signal, whose spectral density is shown in Fig. 3.38a, in a quantum-dynamical computation, leading to a reproduction of the initial mobility value with an accuracy of about 6%. Notably, shifting the artificial signal towards higher frequencies, aligning its characteristics more closely with those of $MAPbBr_3$ (depicted in Fig. 3.38b), does not further alter the mobility. This observation indicates that the frequency shift observed between the two systems has only limited impact on the carrier mobility - as opposed to the different energy fluctuations of $MAPbI_3$ and $MAPbBr_3$.

In summary, we posit that the primary factor distinguishing carrier dynamics in $MAPbI_3$ and $MAPbBr_3$ at lower temperatures is the varying degree of dynamic disorder. This is because increasing the fluctuations in the $t_{pp\sigma}$ couplings of $MAPbI_3$ results in a substantial decrease in the carrier mobility at 300 K. Conversely, alterations to the onsite terms have a comparatively lesser impact, and shifting fluctuations towards higher frequencies results in minimal consequences.

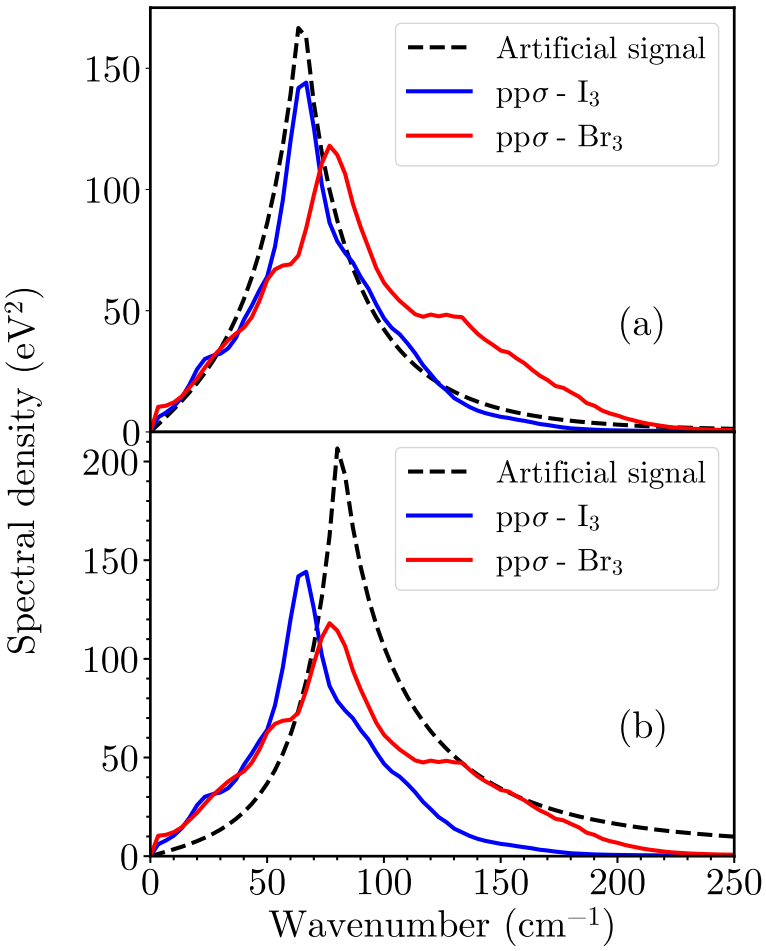

Figure 3.38: Panel a: The initial spectral density data for low-frequency ppσ fluctuations in $MAPbI_3$ (blue line) and $MAPbBr_3$ (red line) at 300 K, alongside an artificial signal (dashed line) designed to resemble the original $MAPbI_3$ curve. Panel b: Similar to the left panel, the artificial signal has been adjusted to a higher frequency to replicate the frequency shift observed when comparing the original spectral density between the two systems.

Building upon this finding, we aim to delve deeper into the temperature-dependent behavior of energy fluctuations, thus establishing a connection with the similarly temperature-dependent anharmonic characteristics in both $MAPbI_3$ and $MAPbBr_3$. In Fig. 3.39, we present the temperature-induced variations in the relative fluctuations of Pb-X bond distances and ppσ overlaps. We observe stronger relative fluctuations in the bond distances of $MAPbBr_3$ compared to $MAPbI_3$, especially at lower temperatures. However, this difference gradually diminishes as the temperature rises. This observation aligns with the heightened anharmonic behavior of $MAPbBr_3$ at lower temperatures and is mirrored in the relative fluctuations of the ppσ overlaps. At lower temperatures, they exhibit more significant magnitudes for $MAPbBr_3$ than for $MAPbI_3$. Nonetheless, as the temperature rises, those of $MAPbI_3$ experience a more pronounced increase, eventually reaching a nearly equal magnitude with $MAPbBr_3$ at 350 K, where both materials assume the cubic phase. This proves a microscopically intertwined relationship between anharmonicity and dynamic disorder, and

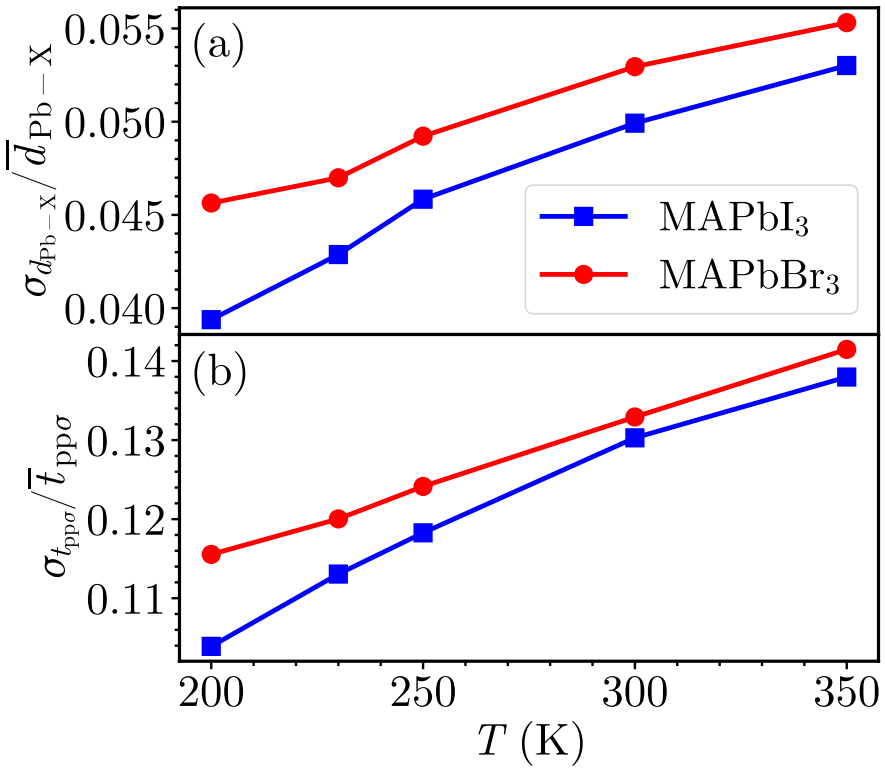

Figure 3.39: Relative fluctuations in Pb-X bond-distances and $t_{pp\sigma}$ overlaps for $MAPbI_3$ and $MAPbBr_3$ as a function of temperature. This data is computed by determining the ratio between the standard deviation ($\sigma_{d_{Pb-X}}$ and $\sigma_{t_{pp\sigma}}$, respectively) and the mean value ($\bar{d}_{Pb-X}$ and $\bar{t}pp\sigma$, respectively).

these two factors are the pivotal determinants of the charge carrier mobility and its temperature dependence in HaPs.

To be more precise, we claim that the heightened anharmonicity and dynamic disorder are responsible for diminishing carrier mobilities. Our findings reconcile the disparities between experimental observations and theoretical models regarding the dominant carrier-scattering mechanisms in HaPs. It is only by considering this anharmonicity, a critical aspect of the lattice dynamics in hybrid HaPs [122, 129, 134, 139, 152–161], that we can adequately explore electronic dynamics, contrasting it with the semi-classical Boltzmann transport approach. Additionally, this advanced treatment incorporates interband effects (i.e., phenomena that occur between different energy bands, such as optical transitions or interband scattering), a crucial aspect often overlooked in other methodologies.

To conclude this section, it is worth noting that there are ongoing efforts to develop effective harmonic potentials to extend the applicability of perturbative momentum-space electron-phonon techniques to anharmonic materials [150, 249]. Nevertheless, no effective harmonic potential can comprehensively describe the intricate lattice dynamics observed in hybrid HaPs, such as $MAPbI_3$ and $MAPbBr_3$. This is primarily

due to the substantial non-Gaussian nature of atomic displacements, as shown in Fig. 3.22. This challenge appears to extend to related compounds like $CsPbBr_3$ [147].

4 Conclusions and Outlook

HaPs represent a fascinating and relatively new class of materials that hold big promise in solar cell technology. This potential becomes evident when considering the significant advancements in the photovoltaic conversion efficiency of HaP-based devices [20–23]. Despite a huge amount of research [11–19], several fundamental questions remain unanswered regarding the underlying mechanisms responsible for the intriguing structural and optoelectronic properties of HaPs [24].

A key concept for understanding the optoelectronic properties is the interactions between electrons and the lattice. The conventional framework for describing these is the Fröhlich interaction, which assumes the formation of large polarons. Despite the presence of various experimental observations that indicate polaronic effects, such as the development of stress fields following light absorption in $MAPbBr_3$ [172] and the photoinduced compositional segregation in mixed-halide crystals [173–175], doubts have been raised concerning the presence of large polarons as described in the Fröhlich interaction framework. These doubts stem from observations of optical and charge carrier behaviors in HaPs. Specifically, Ref. [189] has demonstrated that the incorporation of high-order terms in the calculation of temperature-dependent band gaps in HaPs leads to substantial changes, indicating that low-order electron-phonon coupling terms may be insufficient. Furthermore, numerical calculations of the polaron mobility in the Fröhlich formalism [192], applied to HaPs with intermediate coupling strength, are in stark contradiction with experimental findings [116, 194–199]. Additionally, in the context of HaPs, more fundamental concepts from the polaron and band theory frameworks appear to have limited applicability. This is primarily attributed to the unique structural characteristics of HaPs, including their soft and polar lattice, which gives rise to local polar fluctuations and low-frequency lattice vibrations. These factors result in remarkably short scattering and relaxation times for charge carriers and short mean free paths. Consequently, it is highly probable that the MIR criterion is violated in HaPs, particularly around room temperature. This suggests that conventional models, such as the Boltzmann transport equation and polaronic scattering mechanisms, cannot adequately capture the behavior of charge carrier transport in HaPs.

We introduced an alternative concept called "dynamic disorder," drawing inspiration from carrier scattering in organic crystals. Although the time and length scales associated with carrier scattering in HaPs still differ from those in organic crystals, we proposed that the dynamic disorder perspective provides a viable and insightful interpretation of electron-lattice interactions. We contended that this mechanism not only encompasses the traditional polaronic vibrations used in the Fröhlich Hamiltonian but also comprehensively considers nonlinear coupling contributions and the anharmonic vibrations of the lattice. As demonstrated in Refs. [5, 206] and in this

work, the dynamic disorder framework successfully addresses various limitations of conventional band-theory approaches.

To be precise, we conducted computational studies using DFT, MD, and TB to compare two representative examples of hybrid HaPs, namely, $MAPbI_3$ and $MAPbBr_3$. Our focus was to investigate the relationship between anharmonicity and dynamic disorder and their influence on optoelectronic properties. Utilizing a multi-scale TB model parameterized through first-principles MD simulations and applied to large-scale supercells derived from classical FF MD simulations, we calculated optoelectronic properties and performed semiclassical Ehrenfest charge carrier dynamics simulations. We elucidated the connection between the broadened band gap distributions observed in $MAPbBr_3$ in comparison to $MAPbI_3$ and the magnitude of the Urbach energy, thereby shedding light on the impact of the disorder on the properties of solar-absorber materials. Moreover, we calculated the charge carrier mobilities, providing valuable insights into electrical transport properties. In Fig. 4.1, we illustrate how our multi-scale TB model, incorporating the dynamic disorder framework, reproduces the experimentally observed temperature dependence of the charge carrier mobility in HaPs. This stands in stark contrast to the results obtained when combining the large-polaron concept with the Boltzmann transport equation.

In addition, through our approach, it was possible to explain the differences in the temperature-dependent mobilities observed in $MAPbI_3$ and $MAPbBr_3$. Across a broad temperature range, $MAPbBr_3$ exhibits increased anharmonicity. Simultaneously, its charge carrier mobility experiences a significant reduction compared to that of $MAPbI_3$, closely reflecting the varying atomic dynamics in these two materials. As the temperature rises, the degrees of anharmonicity and the associated dynamic disorder in both compounds become more similar, a phenomenon linked to their different tetragonal-to-cubic phase transition temperatures. Through a series of gedankenexperiments, we found that the degree of dynamic disorder directly influences the magnitude of the charge carrier mobilities. Conversely, neither the pure band momentum picture nor the consideration of effective masses alone can adequately account for the temperature-dependent variations in mobilities. These findings hold considerable practical significance, as they offer insights into the tailoring of specific properties in semiconductor devices to meet their desired specifications.

Numerous intriguing questions and areas of research remain unexplored. First, it is widely recognized that relativistic effects, such as SOC, play an important role in HaPs [250]. This is closely linked with the transient localization of band-edge carriers, a phenomenon that remains not fully understood. This localization not only influences the dynamic changes in orbital overlaps and dynamic disorder but also impacts polaronic effects in HaPs. To illustrate, it is worth noting that the scenario where mobility decreases with temperature due to dynamic disorder and transient localization [251] stands in contrast to the more typical scenario where localization results in an increase in mobility with temperature.

Our TB model could also explore the influence of defects on the optoelectronic

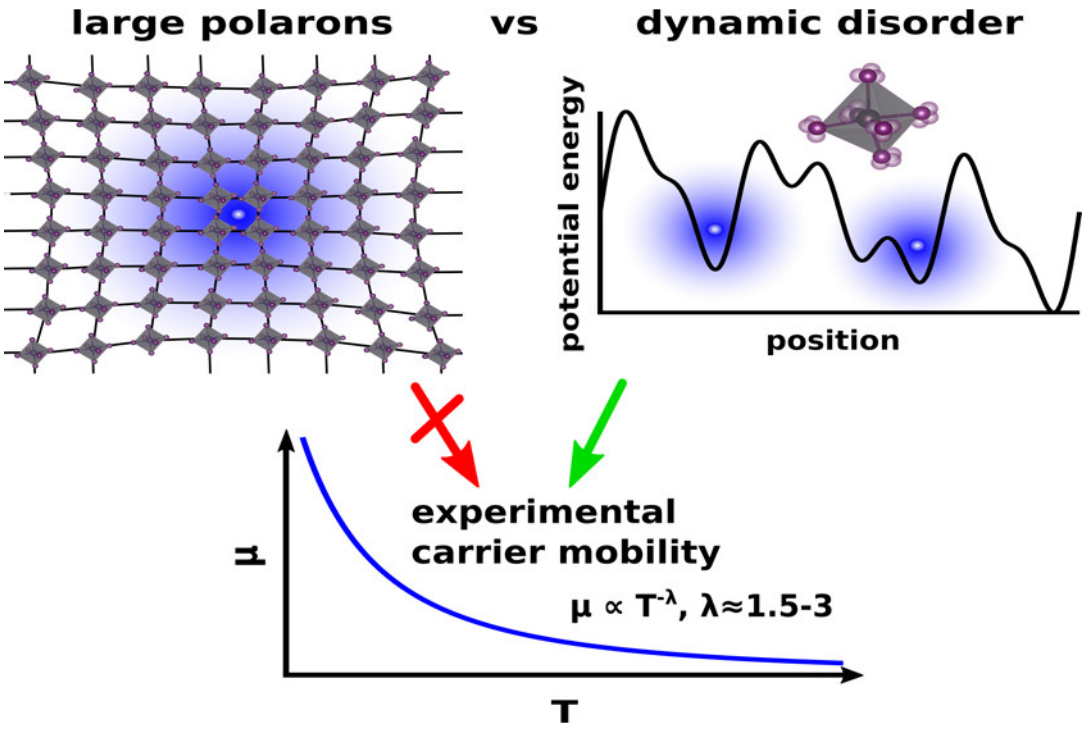

Figure 4.1: Schematic diagram illustrating that the experimental temperature-dependent mobility behavior can be reproduced by employing the dynamic disorder model in conjunction with the TB formalism, in contrast to relying solely on the large-polaron and Boltzmann transport approach. Reprinted with permission from Ref. [1]. Copyright 2021 American Chemical Society.

properties in HaPs. Defects, such as vacancies and doping, are very important for developing solar cell devices, and their understanding can have a major influence on the design of perovskites for energy conversion. In general, there is a large variety of theoretical and experimental work [114, 252, 253]. Nevertheless, there is no doubt that defects can contribute to the optoelectronic properties of HaPs. For example, the exact influence of defect-related trap densities on the optoelectronic properties remains unclear. Our multi-scale model could be expanded so that it takes into account vibrations around defects. In general, there are many types of possible defects in HaPs, as in any semiconductor. One could parametrize the TB model using DFT calculations of defect-containing supercells, starting with simple halide vacancies and interstitials and proceeding to more complicated scenarios (e.g., defect pairs). As has been shown in Ref. [254] the temporal fluctuations in defect eigenvalues of the HaP crystal $CsPbBr_3$ are reasonably well correlated with distances between neighboring atoms. Hence, one could again parameterize the TB model with nearest-neighbor parameters.

Another intriguing prospective challenge involves exploring the excited-state dynamics of hot carriers and excitons using a Bloch equation formalism, which is parameterized with the help of TB and MD. Excitons are fundamental electronic excitations found in semiconductor crystals, corresponding to bound states

of electron-hole pairs. Interestingly, the MIR criterion seems to be violated over a broad temperature range for excitons, as indicated by an experimental investigation of the temperature-dependent exciton mobilities in a 2D HaP material [255]. Therefore, further exploration of the interaction between dynamic disorder and excitonic phenomena seems to be very interesting. For that reason, one could develop a two-particle model. Unlike the one-particle scenario, where we need to decide whether to focus on electrons or holes, leading to the utilization of different Wannier functions for the conduction and valence bands as initial conditions for time evolution, a two-particle approach could potentially tackle both simultaneously.

The term "hot carriers", on the other hand, refers to either electrons or holes, which acquire kinetic energy significantly higher than what would be expected at thermal equilibrium. This can be the result of an acceleration by an electric field. Hot carriers can have both positive and negative effects. On the one hand, in certain types of solar cells, the generation of hot carriers can increase the efficiency of energy conversion. On the other hand, due to their heightened kinetic energy, hot carriers have the potential to be trapped in specific regions of semiconductor devices, leading to the creation of a space charge, which, in turn, can cause instability in the device. Research into the transport of hot carriers holds significant promise. This is particularly relevant in the context of solar cell efficiency, where surpassing the Shockley-Queisser limit of 33% [9] is possible due to efficient charge transport in thin films [256]. Achieving this goal hinges on efficiently extracting hot charge carriers from solar cells before they lose energy during their journey toward equilibrium. Additionally, Ref. [129] demonstrated that energy could be transferred from the lattice, as evidenced by changes in mean squared atomic displacements. To address excitons, it may be advantageous to employ Semiconductor Bloch equations and parameterize them using our TB methodology. The general framework for employing Bloch equations is outlined in Ref. [257]. In this context, Bloch equations describe the interconnected dynamics of carrier occupation in the conduction and valence bands, and a similar approach can be applied to investigate hot carriers.

Moreover, the formalism of the multi-scale TB model could be transferred to a broad spectrum of materials. Its application to other perovskites like $CsPbBr_3$ or $SrTiO_3$ would be straightforward. This holds practical relevance given the desire to remove toxic lead from perovskite materials. In the context of the previously discussed organic crystals, the TB scheme can be applied to organic semiconductors, which hold great significance in the advancement of PV materials [23, 258].

Last but not least, we could further generalize our TB model. This entails the development of mathematical tools and formalisms that simplify the parameterization of a TB model without the need to conduct numerous intricate and resource-intensive procedures. This idea is the basis of a recent study by Schwade et al. [3], in which they introduce a TB approach utilizing hybrid-orbital basis functions. This approach incorporates distance-dependent matrix elements via a numerical integration of atomic orbitals. The resulting parameter set can be efficiently optimized through DFT. In a subsequent phase, this model can be combined with advanced techniques such as machine learning MD and hybrid DFT to compute electronic properties at

finite temperatures for classic and straightforward semiconductors like GaAs. Implementing this approach for more complex materials such as HaPs can significantly enhance our understanding of these compounds and related materials.

Bibliography

[1] M. J. Schilcher, P. J. Robinson, D. J. Abramovitch, L. Z. Tan, A. M. Rappe, D. R. Reichman, D. A. Egger, *ACS Energy Lett.* **2021**, *6*, 2162–2173.

[2] M. J. Schilcher, D. J. Abramovitch, M. Z. Mayers, L. Z. Tan, D. R. Reichman, D. A. Egger, *Phys. Rev. Materials* **2023**, *7*, L081601.

[3] M. Schwade, M. J. Schilcher, C. R. Baecker, M. Grumet, D. A. Egger, **2023**, DOI 10.48550/ARXIV.2308.08897.

[4] E. Sirotti, L. I. Wagner, C.-M. Jiang, J. Eichhorn, F. Munnik, V. Streibel, M. J. Schilcher, B. März, M. Kuhl, M. Höldrich, D. A. Egger, I. D. Sharp, *in preparation* **2023**.

[5] M. Z. Mayers, L. Z. Tan, D. A. Egger, A. M. Rappe, D. R. Reichman, *Nano Lett.* **2018**, *18*, 8041–8046.

[6] D. Egger, *Blick Wiss.* **2018**, *26*, 9–13.

[7] J. N. Mayer, S. Philipps, N. S. Hussein, T. Schlegl, C. Senkpiel, *Fraunhofer ISE* **2015**.

[8] C. Ballif, F.-J. Haug, M. Boccard, P. J. Verlinden, G. Hahn, *Nat. Rev. Mater.* **2022**, *7*, 597–616.

[9] W. Shockley, H. J. Queisser, *J. Appl. Phys.* **1961**, *32*, 510–519.

[10] D. Weber, *Z. Für Naturforschung B* **1978**, *33*, 1443–1445.

[11] T. M. Brenner, D. A. Egger, L. Kronik, G. Hodes, D. Cahen, *Nat. Rev. Mater.* **2016**, *1*, 15007.

[12] A. Kojima, K. Teshima, Y. Shirai, T. Miyasaka, *J. Am. Chem. Soc.* **2009**, *131*, 6050–6051.

[13] M. M. Lee, J. Teuscher, T. Miyasaka, T. N. Murakami, H. J. Snaith, *Science* **2012**, *338*, 643–647.

[14] J. Burschka, N. Pellet, S.-J. Moon, R. Humphry-Baker, P. Gao, M. K. Nazeeruddin, M. Grätzel, *Nature* **2013**, *499*, 316–319.

[15] M. Liu, M. B. Johnston, H. J. Snaith, *Nature* **2013**, *501*, 395–398.

[16] S. Kazim, M. K. Nazeeruddin, M. Grätzel, S. Ahmad, *Angew. Chem. Int. Ed.* **2014**, *53*, 2812–2824.

[17] S. D. Stranks, H. J. Snaith, *Nat. Nanotechnol.* **2015**, *10*, 391–402.

[18] J.-P. Correa-Baena, M. Saliba, T. Buonassisi, M. Grätzel, A. Abate, W. Tress, A. Hagfeldt, *Science* **2017**, *358*, 739–744.

[19] H. Tsai, R. Asadpour, J.-C. Blancon, C. C. Stoumpos, O. Durand, J. W. Strzalka, B. Chen, R. Verduzco, P. M. Ajayan, S. Tretiak, J. Even, M. A. Alam, M. G. Kanatzidis, W. Nie, A. D. Mohite, *Science* **2018**, *360*, 67–70.

[20] N.-G. Park, *J. Phys. Chem. Lett.* **2013**, *4*, 2423–2429.

[21] H. J. Snaith, *J. Phys. Chem. Lett.* **2013**, *4*, 3623–3630.

[22] T. M. Brenner, D. A. Egger, A. M. Rappe, L. Kronik, G. Hodes, D. Cahen, *J. Phys. Chem. Lett.* **2015**, *6*, 4754–4757.

[23] Best Research-Cell Efficiency Chart, https://www.nrel.gov/pv/cell-efficiency.html, **2023**.

[24] D. A. Egger, A. Bera, D. Cahen, G. Hodes, T. Kirchartz, L. Kronik, R. Lovrincic, A. M. Rappe, D. R. Reichman, O. Yaffe, *Adv. Mater.* **2018**, *30*, 1800691.

[25] A. Sadhanala, F. Deschler, T. H. Thomas, S. E. Dutton, K. C. Goedel, F. C. Hanusch, M. L. Lai, U. Steiner, T. Bein, P. Docampo, D. Cahen, R. H. Friend, *J. Phys. Chem. Lett.* **2014**, *5*, 2501–2505.

[26] S. De Wolf, J. Holovsky, S.-J. Moon, P. Löper, B. Niesen, M. Ledinsky, F.-J. Haug, J.-H. Yum, C. Ballif, *J. Phys. Chem. Lett.* **2014**, *5*, 1035–1039.

[27] S. P. Senanayak, B. Yang, T. H. Thomas, N. Giesbrecht, W. Huang, E. Gann, B. Nair, K. Goedel, S. Guha, X. Moya, C. R. McNeill, P. Docampo, A. Sadhanala, R. H. Friend, H. Sirringhaus, *Sci. Adv.* **2017**, *3*, e1601935.

[28] J. B. Patel, Q. Lin, O. Zadvorna, C. L. Davies, L. M. Herz, M. B. Johnston, *J. Phys. Chem. Lett.* **2018**, *9*, 263–268.

[29] M. Ledinsky, T. Schönfeldová, J. Holovský, E. Aydin, Z. Hájková, L. Landová, N. Neyková, A. Fejfar, S. De Wolf, *J. Phys. Chem. Lett.* **2019**, *10*, 1368–1373.

[30] L. Wang, D. Beljonne, *J. Chem. Phys.* **2013**, *139*, 064316.

[31] J. W. Demmel, O. A. Marques, B. N. Parlett, C. Vömel, *SIAM J. Sci. Comput.* **2008**, *30*, 1508–1526.

[32] E. Prodan, W. Kohn, *Proc. Natl. Acad. Sci. U.S.A.* **2005**, *102*, 11635–11638.

[33] D. R. Bowler, T. Miyazaki, *Rep. Prog. Phys.* **2012**, *75*, 036503.

[34] N. W. Ashcroft, N. D. Mermin, *Solid State Physics*, Holt, Rinehart and Winston, New York, **1976**.

[35] R. M. Martin, *Electronic Structure: Basic Theory and Practical Methods*, 2nd ed., Cambridge University Press, **2020**.

[36] M. T. Dove, *Introduction to Lattice Dynamics*, 1st ed., Cambridge University Press, **1993**.

[37] D. Frenkel, B. Smit, *Understanding Molecular Simulation: From Algorithms to Applications*, 2nd ed, Academic Press, San Diego, **2002**.

[38] *A Primer in Density Functional Theory*, (Eds.: C. Fiolhais, F. Nogueira, M. A. L. Marques), Springer, Berlin ; New York, **2003**.

[39] P. H. Hünenberger in *Advanced Computer Simulation*, *Vol. 173*, (Eds.: A. Abe, J.-F. Joanny, A.-C. Albertsson, R. Duncan, H.-H. Kausch, S. Kobayashi, K. Dušek, K.-S. Lee, W. De Jeu, L. Leibler, O. Nuyken, T. E. Long, E. Terentjev, B. Voit, I. Manners, G. Wegner, M. Möller, C. Dr. Holm, K. Prof. Dr. Kremer), Springer Berlin Heidelberg, Berlin, Heidelberg, **2005**, pp. 105–149.

[40] H. B. Lee, W. Cai, Ewald Summation for Coulomb Interactions in a Periodic Supercell, https://api.semanticscholar.org/CorpusID:43767138, **2009**.

[41] D. Marx, J. Hutter, *Ab Initio Molecular Dynamics: Basic Theory and Advanced Methods*, 1st ed., Cambridge University Press, **2009**.

[42] R. Gross, A. Marx, *Festkörperphysik*, Oldenbourg, München, **2012**.

[43] A. Nitzan, *Chemical Dynamics in Condensed Phases: Relaxation, Transfer, and Reactions in Condensed Molecular Systems*, OUP Oxford, **2013**.

[44] The VASP Manual - Vaspwiki, https://www.vasp.at/wiki/index.php/The_VASP_Manual, **2023**.

[45] LAMMPS Documentation, https://docs.lammps.org/Manual.html, **2023**.

[46] Wannier90: User Guide, https://wannier.org/support/, **2023**.

[47] M. Born, R. Oppenheimer, *Ann. Phys.* **1927**, *389*, 457–484.

[48] P. Hohenberg, W. Kohn, *Phys. Rev.* **1964**, *136*, B864–B871.

[49] W. Kohn, L. J. Sham, *Phys. Rev.* **1965**, *140*, A1133–A1138.

[50] D. M. Ceperley, B. J. Alder, *Phys. Rev. Lett.* **1980**, *45*, 566–569.

[51] J. P. Perdew, K. Burke, M. Ernzerhof, *Phys. Rev. Lett.* **1996**, *77*, 3865–3868.

[52] E. Antončík, *Czech. J. Phys.* **1954**, *4*, 439–451.

[53] E. Antončík, *J. Phys. Chem. Solids.* **1959**, *10*, 314–320.

[54] J. C. Phillips, L. Kleinman, *Phys. Rev.* **1959**, *116*, 287–294.

[55] D. R. Hamann, M. Schlüter, C. Chiang, *Phys. Rev. Lett.* **1979**, *43*, 1494–1497.

[56] G. Kresse, D. Joubert, *Phys. Rev. B* **1999**, *59*, 1758–1775.

[57] J. Feng, *APL Mater.* **2014**, *2*, 081801.

[58] Y. Wang, T. Gould, J. F. Dobson, H. Zhang, H. Yang, X. Yao, H. Zhao, *Phys. Chem. Chem. Phys.* **2014**, *16*, 1424–1429.

[59] D. A. Egger, L. Kronik, *J. Phys. Chem. Lett.* **2014**, *5*, 2728–2733.

[60] C. Motta, F. El-Mellouhi, S. Kais, N. Tabet, F. Alharbi, S. Sanvito, *Nat. Commun.* **2015**, *6*, 7026.

[61] M. Faghihnasiri, M. Izadifard, M. E. Ghazi, *J. Phys. Chem. C* **2017**, *121*, 27059–27070.

[62] A. Tkatchenko, M. Scheffler, *Phys. Rev. Lett.* **2009**, *102*, 073005.

[63] N. Marom, A. Tkatchenko, M. Rossi, V. V. Gobre, O. Hod, M. Scheffler, L. Kronik, *J. Chem. Theory Comput.* **2011**, *7*, 3944–3951.

[64] W. A. Al-Saidi, V. K. Voora, K. D. Jordan, *J. Chem. Theory Comput.* **2012**, *8*, 1503–1513.

[65] X. Chu, A. Dalgarno, *J. Chem. Phys.* **2004**, *121*, 4083–4088.

[66] P.-O. Löwdin, *J. Chem. Phys.* **1950**, *18*, 365–375.

[67] M. Menon, K. R. Subbaswamy, *Phys. Rev. B* **1997**, *55*, 9231–9234.

[68] J. C. Slater, G. F. Koster, *Phys. Rev.* **1954**, *94*, 1498–1524.

[69] A. K. Geim, *Science* **2009**, *324*, 1530–1534.

[70] J. Arkowski, M. Obremska, K. Kędzierski, A. Sławuta, M. Wawrzyńska, *Adv. Clin. Exp. Med.* **2020**, *29*, 1497–1504.

[71] O. D. Salahdin, H. Sayadi, R. Solanki, R. M. R. Parra, M. Al-Thamir, A. T. Jalil, S. E. Izzat, A. T. Hammid, L. A. B. Arenas, E. Kianfar, *Appl. Phys. A* **2022**, *128*, 703.

[72] D. J. Chadi, M. L. Cohen, *phys. stat. sol. (b)* **1975**, *68*, 405–419.

[73] P. P. Ewald, *Ann. Phys.* **1921**, *369*, 253–287.

[74] G. H. Wannier, *Phys. Rev.* **1937**, *52*, 191–197.

[75] N. Marzari, D. Vanderbilt, *Phys. Rev. B* **1997**, *56*, 12847–12865.

[76] I. Souza, N. Marzari, D. Vanderbilt, *Phys. Rev. B* **2001**, *65*, 035109.

[77] N. Marzari, A. A. Mostofi, J. R. Yates, I. Souza, D. Vanderbilt, *Rev. Mod. Phys.* **2012**, *84*, 1419–1475.

[78] A. A. Mostofi, J. R. Yates, Y.-S. Lee, I. Souza, D. Vanderbilt, N. Marzari, *Computer Physics Communications* **2008**, *178*, 685–699.

[79] A. A. Mostofi, J. R. Yates, G. Pizzi, Y.-S. Lee, I. Souza, D. Vanderbilt, N. Marzari, *Comput. Phys. Commun.* **2014**, *185*, 2309–2310.

[80] A. Mattoni, A. Filippetti, M. I. Saba, P. Delugas, *J. Phys. Chem. C* **2015**, *119*, 17421–17428.

[81] T. Hata, G. Giorgi, K. Yamashita, C. Caddeo, A. Mattoni, *J. Phys. Chem. C* **2017**, *121*, 3724–3733.

[82] S. Nosé, *J. Chem. Phys.* **1984**, *81*, 511–519.

[83] W. G. Hoover, *Phys. Rev. A* **1985**, *31*, 1695–1697.

[84] H. C. Andersen, *J. Chem. Phys.* **1980**, *72*, 2384–2393.

[85] H. J. C. Berendsen, J. P. M. Postma, W. F. Van Gunsteren, A. DiNola, J. R. Haak, *J. Chem. Phys.* **1984**, *81*, 3684–3690.

[86] T. Schneider, E. Stoll, *Phys. Rev. B* **1978**, *17*, 1302–1322.

[87] D. J. Evans, *J. Chem. Phys.* **1983**, *78*, 3297–3302.

[88] M. Parrinello, A. Rahman, *J. Appl. Phys.* **1981**, *52*, 7182–7190.

[89] G. J. Martyna, D. J. Tobias, M. L. Klein, *J. Chem. Phys.* **1994**, *101*, 4177–4189.

[90] E. Braun, J. Gilmer, H. B. Mayes, D. L. Mobley, J. I. Monroe, S. Prasad, D. M. Zuckerman, *LiveCoMS* **2019**, *1*, DOI `10.33011/livecoms.1.1.5957`.

[91] B. R. Sutherland, E. H. Sargent, *Nature Photon* **2016**, *10*, 295–302.

[92] H. Kim, J. S. Han, J. Choi, S. Y. Kim, H. W. Jang, *Small Methods* **2018**, *2*, 1700310.

[93] M. A. Green, A. Ho-Baillie, H. J. Snaith, *Nat. Photon.* **2014**, *8*, 506–514.

[94] W. Li, Z. Wang, F. Deschler, S. Gao, R. H. Friend, A. K. Cheetham, *Nat. Rev. Mater.* **2017**, *2*, 16099.

[95] P. K. Nayak, S. Mahesh, H. J. Snaith, D. Cahen, *Nat. Rev. Mater.* **2019**, *4*, 269–285.

[96] V. M. Goldschmidt, *Naturwissenschaften* **1926**, *14*, 477–485.

[97] C. C. Stoumpos, M. G. Kanatzidis, *Adv. Mater.* **2016**, *28*, 5778–5793.

[98] B. Saparov, D. B. Mitzi, *Chem. Rev.* **2016**, *116*, 4558–4596.

[99] N. N. Lal, Y. Dkhissi, W. Li, Q. Hou, Y.-B. Cheng, U. Bach, *Adv. Energy Mater.* **2017**, *7*, 1602761.

[100] C. C. Stoumpos, C. D. Malliakas, M. G. Kanatzidis, *Inorg. Chem.* **2013**, *52*, 9019–9038.

[101] L. M. Herz, *ACS Energy Lett.* **2017**, *2*, 1539–1548.

[102] G. Giorgi, J.-I. Fujisawa, H. Segawa, K. Yamashita, *J. Phys. Chem. Lett.* **2013**, *4*, 4213–4216.

[103] F. Brivio, K. T. Butler, A. Walsh, M. van Schilfgaarde, *Phys. Rev. B* **2014**, *89*, 155204.

[104] X. Y. Chin, D. Cortecchia, J. Yin, A. Bruno, C. Soci, *Nat Commun* **2015**, *6*, 7383.

[105] J.-P. Yang, M. Meissner, T. Yamaguchi, X.-Y. Zhang, T. Ueba, L.-W. Cheng, S. Ideta, K. Tanaka, X.-H. Zeng, N. Ueno, S. Kera, *Sol. RRL* **2018**, *2*, 1800132.

[106] F. Zu, P. Amsalem, D. A. Egger, R. Wang, C. M. Wolff, H. Fang, M. A. Loi, D. Neher, L. Kronik, S. Duhm, N. Koch, *J. Phys. Chem. Lett.* **2019**, *10*, 601–609.

[107] M. Puppin, S. Polishchuk, N. Colonna, A. Crepaldi, D. N. Dirin, O. Nazarenko, R. De Gennaro, G. Gatti, S. Roth, T. Barillot, L. Poletto, R. P. Xian, L. Rettig, M. Wolf, R. Ernstorfer, M. V. Kovalenko, N. Marzari, M. Grioni, M. Chergui, *Phys. Rev. Lett.* **2020**, *124*, 206402.

[108] E. M. Hutter, M. C. Gélvez-Rueda, A. Osherov, V. Bulović, F. C. Grozema, S. D. Stranks, T. J. Savenije, *Nature Mater.* **2017**, *16*, 115–120.

[109] T. Wang, B. Daiber, J. M. Frost, S. A. Mann, E. C. Garnett, A. Walsh, B. Ehrler, *Energy Environ. Sci.* **2017**, *10*, 509–515.

[110] J. Endres, D. A. Egger, M. Kulbak, R. A. Kerner, L. Zhao, S. H. Silver, G. Hodes, B. P. Rand, D. Cahen, L. Kronik, A. Kahn, *J. Phys. Chem. Lett.* **2016**, *7*, 2722–2729.

[111] S. D. Stranks, G. E. Eperon, G. Grancini, C. Menelaou, M. J. P. Alcocer, T. Leijtens, L. M. Herz, A. Petrozza, H. J. Snaith, *Science* **2013**, *342*, 341–344.

[112] F. Zheng, L. Z. Tan, S. Liu, A. M. Rappe, *Nano Lett.* **2015**, *15*, 7794–7800.

[113] D. Niesner, M. Wilhelm, I. Levchuk, A. Osvet, S. Shrestha, M. Batentschuk, C. Brabec, T. Fauster, *Phys. Rev. Lett.* **2016**, *117*, 126401.

[114] W.-J. Yin, T. Shi, Y. Yan, *Appl. Phys. Lett.* **2014**, *104*, 063903.

[115] H. Zhu, K. Miyata, Y. Fu, J. Wang, P. P. Joshi, D. Niesner, K. W. Williams, S. Jin, X. Y. Zhu, *Science* **2016**, *353*, 1409–1413.

[116] M. Karakus, S. A. Jensen, F. D'Angelo, D. Turchinovich, M. Bonn, E. Cánovas, *J. Phys. Chem. Lett.* **2015**, *6*, 4991–4996.

[117] A. Létoublon, S. Paofai, B. Rufflé, P. Bourges, B. Hehlen, T. Michel, C. Ecolivet, O. Durand, S. Cordier, C. Katan, J. Even, *J. Phys. Chem. Lett.* **2016**, *7*, 3776–3784.

[118] M. Yang, Y. Zhou, Y. Zeng, C.-S. Jiang, N. P. Padture, K. Zhu, *Adv. Mater.* **2015**, *27*, 6363–6370.

[119] H. Zhu, Y. Fu, F. Meng, X. Wu, Z. Gong, Q. Ding, M. V. Gustafsson, M. T. Trinh, S. Jin, X.-Y. Zhu, *Nature Mater.* **2015**, *14*, 636–642.

[120] S. Sun, Y. Fang, G. Kieslich, T. J. White, A. K. Cheetham, *J. Mater. Chem. A* **2015**, *3*, 18450–18455.

[121] Y. Rakita, S. R. Cohen, N. K. Kedem, G. Hodes, D. Cahen, *MRS Commun.* **2015**, *5*, 623–629.

[122] O. Yaffe, Y. Guo, L. Z. Tan, D. A. Egger, T. Hull, C. C. Stoumpos, F. Zheng, T. F. Heinz, L. Kronik, M. G. Kanatzidis, J. S. Owen, A. M. Rappe, M. A. Pimenta, L. E. Brus, *Phys. Rev. Lett.* **2017**, *118*, 136001.

[123] A. Poglitsch, D. Weber, *J. Chem. Phys.* **1987**, *87*, 6373–6378.

[124] T. Baikie, N. S. Barrow, Y. Fang, P. J. Keenan, P. R. Slater, R. O. Piltz, M. Gutmann, S. G. Mhaisalkar, T. J. White, *J. Mater. Chem. A* **2015**, *3*, 9298–9307.

[125] S. Colella, E. Mosconi, P. Fedeli, A. Listorti, F. Gazza, F. Orlandi, P. Ferro, T. Besagni, A. Rizzo, G. Calestani, G. Gigli, F. De Angelis, R. Mosca, *Chem. Mater.* **2013**, *25*, 4613–4618.

[126] K. G. Stamplecoskie, J. S. Manser, P. V. Kamat, *Energy Environ. Sci.* **2015**, *8*, 208–215.

[127] E. T. Hoke, D. J. Slotcavage, E. R. Dohner, A. R. Bowring, H. I. Karunadasa, M. D. McGehee, *Chem. Sci.* **2015**, *6*, 613–617.

[128] L. D. Whalley, J. M. Skelton, J. M. Frost, A. Walsh, *Phys. Rev. B* **2016**, *94*, 220301.

[129] X. Wu, L. Z. Tan, X. Shen, T. Hu, K. Miyata, M. T. Trinh, R. Li, R. Coffee, S. Liu, D. A. Egger, I. Makasyuk, Q. Zheng, A. Fry, J. S. Robinson, M. D. Smith, B. Guzelturk, H. I. Karunadasa, X. Wang, X. Zhu, L. Kronik, A. M. Rappe, A. M. Lindenberg, *Sci. Adv.* **2017**, *3*, e1602388.

[130] A. Marronnier, H. Lee, B. Geffroy, J. Even, Y. Bonnassieux, G. Roma, *J. Phys. Chem. Lett.* **2017**, *8*, 2659–2665.

[131] A. Marronnier, G. Roma, S. Boyer-Richard, L. Pedesseau, J.-M. Jancu, Y. Bonnassieux, C. Katan, C. C. Stoumpos, M. G. Kanatzidis, J. Even, *ACS Nano* **2018**, *12*, 3477–3486.

[132] J. P. H. Rivett, L. Z. Tan, M. B. Price, S. A. Bourelle, N. J. L. K. Davis, J. Xiao, Y. Zou, R. Middleton, B. Sun, A. M. Rappe, D. Credgington, F. Deschler, *Nat. Commun.* **2018**, *9*, 3531.

[133] C. Wang, Y. Liu, S. F. Liu, B. Li, Y. Chen, *J. Phys. Chem. Lett.* **2018**, *9*, 3029–3034.

[134] A. Gold-Parker, P. M. Gehring, J. M. Skelton, I. C. Smith, D. Parshall, J. M. Frost, H. I. Karunadasa, A. Walsh, M. F. Toney, *Proc. Natl. Acad. Sci. U.S.A.* **2018**, *115*, 11905–11910.

[135] T. Zhu, E. Ertekin, *Energy Environ. Sci.* **2019**, *12*, 216–229.

[136] C. Gehrmann, D. A. Egger, *Nat. Commun.* **2019**, *10*, 3141.

[137] R. Sharma, Z. Dai, L. Gao, T. M. Brenner, L. Yadgarov, J. Zhang, Y. Rakita, R. Korobko, A. M. Rappe, O. Yaffe, *Phys. Rev. Mat.* **2020**, *4*, 092401.

[138] D. H. Fabini, R. Seshadri, M. G. Kanatzidis, *MRS Bull.* **2020**, *45*, 467–477.

[139] A. N. Beecher, O. E. Semonin, J. M. Skelton, J. M. Frost, M. W. Terban, H. Zhai, A. Alatas, J. S. Owen, A. Walsh, S. J. L. Billinge, *ACS Energy Lett.* **2016**, *1*, 880–887.

[140] M. Wang, S. Lin, *Adv. Funct. Mater.* **2016**, *26*, 5297–5306.

[141] D. H. Fabini, G. Laurita, J. S. Bechtel, C. C. Stoumpos, H. A. Evans, A. G. Kontos, Y. S. Raptis, P. Falaras, A. Van der Ven, M. G. Kanatzidis, R. Seshadri, *J. Am. Chem. Soc.* **2016**, *138*, 11820–11832.

[142] D. H. Fabini, T. Hogan, H. A. Evans, C. C. Stoumpos, M. G. Kanatzidis, R. Seshadri, *J. Phys. Chem. Lett.* **2016**, *7*, 376–381.

[143] G. Laurita, D. H. Fabini, C. C. Stoumpos, M. G. Kanatzidis, R. Seshadri, *Chem. Sci.* **2017**, *8*, 5628–5635.

[144] K. L. Brown, S. F. Parker, I. R. García, S. Mukhopadhyay, V. G. Sakai, C. Stock, *Phys. Rev. B* **2017**, *96*, 174111.

[145] M. A. Carignano, S. A. Aravindh, I. S. Roqan, J. Even, C. Katan, *J. Phys. Chem. C* **2017**, *121*, 20729–20738.

[146] E. Cockayne, B. P. Burton, *Phys. Rev. B* **2000**, *62*, 3735–3743.

[147] J. Klarbring, O. Hellman, I. A. Abrikosov, S. I. Simak, *Phys. Rev. Lett.* **2020**, *125*, 045701.

[148] L. A. D. Irvine, A. B. Walker, M. J. Wolf, *Phys. Rev. B* **2021**, *103*, L220305.

[149] K.-C. Zhang, C. Shen, H.-B. Zhang, Y.-F. Li, Y. Liu, *Phys. Rev. B* **2022**, *106*, 235202.

[150] M. Zacharias, G. Volonakis, F. Giustino, J. Even, *npj Comput Mater* **2023**, *9*, 153.

[151] S. A. Seidl, X. Zhu, G. Reuveni, S. Aharon, C. Gehrmann, S. Caicedo-Dávila, O. Yaffe, D. A. Egger, *Phys. Rev. Materials* **2023**, *7*, L092401.

[152] T. Debnath, D. Sarker, H. Huang, Z.-K. Han, A. Dey, L. Polavarapu, S. V. Levchenko, J. Feldmann, *Nat. Commun.* **2021**, *12*, 2629.

[153] O. Cannelli, J. Wiktor, N. Colonna, L. Leroy, M. Puppin, C. Bacellar, I. Sadykov, F. Krieg, G. Smolentsev, M. V. Kovalenko, A. Pasquarello, M. Chergui, G. F. Mancini, *J. Phys. Chem. Lett.* **2022**, *13*, 3382–3391.

[154] X. Zhu, S. Caicedo-Dávila, C. Gehrmann, D. A. Egger, *ACS Appl. Mater. Interfaces* **2022**, *14*, 22973–22981.

[155] E. Fransson, P. Rosander, F. Eriksson, J. M. Rahm, T. Tadano, P. Erhart, *Commun Phys* **2023**, *6*, 173.

[156] N. J. Weadock, T. C. Sterling, J. A. Vigil, A. Gold-Parker, I. C. Smith, B. Ahammed, M. J. Krogstad, F. Ye, D. Voneshen, P. M. Gehring, A. M. Rappe, H.-G. Steinrück, E. Ertekin, H. I. Karunadasa, D. Reznik, M. F. Toney, *Joule* **2023**, *7*, 1051–1066.

[157] R. X. Yang, J. M. Skelton, E. L. da Silva, J. M. Frost, A. Walsh, *J. Phys. Chem. Lett.* **2017**, *8*, 4720–4726.

[158] J. Klarbring, *Phys. Rev. B* **2019**, *99*, 104105.

[159] J. Liu, A. E. Phillips, D. A. Keen, M. T. Dove, *J. Phys. Chem. C* **2019**, *123*, 14934–14940.

[160] A. C. Ferreira, S. Paofai, A. Létoublon, J. Ollivier, S. Raymond, B. Hehlen, B. Rufflé, S. Cordier, C. Katan, J. Even, P. Bourges, *Commun. Phys.* **2020**, *3*, 48.

[161] T. Lanigan-Atkins, X. He, M. J. Krogstad, D. M. Pajerowski, D. L. Abernathy, G. N. M. N. Xu, Z. Xu, D.-Y. Chung, M. G. Kanatzidis, S. Rosenkranz, R. Osborn, O. Delaire, *Nat. Mater.* **2021**, *20*, 977–983.

[162] P. Y. Yu, M. Cardona, *Fundamentals of Semiconductors: Physics and Materials Properties*, Springer, Berlin, Germany, **2010**.

[163] G. D. Mahan, *Many Particle Physics, Third Edition*, Plenum, New York, **2000**.

[164] N.-E. Lee, J.-J. Zhou, H.-Y. Chen, M. Bernardi, *Nat Commun* **2020**, *11*, 1607.

[165] A. D. Wright, C. Verdi, R. L. Milot, G. E. Eperon, M. A. Pérez-Osorio, H. J. Snaith, F. Giustino, M. B. Johnston, L. M. Herz, *Nat. Commun.* **2016**, *7*, 11755.

[166] M. Sendner, P. K. Nayak, D. A. Egger, S. Beck, C. Müller, B. Epding, W. Kowalsky, L. Kronik, H. J. Snaith, A. Pucci, R. Lovrinčić, *Mater. Horiz.* **2016**, *3*, 613–620.

[167] H. Fröhlich, *Advances in Physics* **1954**, *3*, 325–361.

[168] C. M. Iaru, A. Brodu, N. J. J. Van Hoof, S. E. T. Ter Huurne, J. Buhot, F. Montanarella, S. Buhbut, P. C. M. Christianen, D. Vanmaekelbergh, C. De Mello Donega, J. G. Rivas, P. M. Koenraad, A. Y. Silov, *Nat. Commun.* **2021**, *12*, 5844.

[169] C. Franchini, M. Reticcioli, M. Setvin, U. Diebold, *Nat Rev Mater* **2021**, *6*, 560–586.

[170] J. M. Frost, *Phys. Rev. B* **2017**, *96*, 195202.

[171] M. Schlipf, S. Poncé, F. Giustino, *Phys. Rev. Lett.* **2018**, *121*, 086402.

[172] B. Guzelturk, T. Winkler, T. W. J. Van de Goor, M. D. Smith, S. A. Bourelle, S. Feldmann, M. Trigo, S. W. Teitelbaum, H.-G. Steinrück, G. A. de la Pena, R. Alonso-Mori, D. Zhu, T. Sato, H. I. Karunadasa, M. F. Toney, F. Deschler, A. M. Lindenberg, *Nat. Mater.* **2021**, *20*, 618–623.

[173] C. G. Bischak, C. L. Hetherington, H. Wu, S. Aloni, D. F. Ogletree, D. T. Limmer, N. S. Ginsberg, *Nano Lett.* **2017**, *17*, 1028–1033.

[174] C. G. Bischak, A. B. Wong, E. Lin, D. T. Limmer, P. Yang, N. S. Ginsberg, *J. Phys. Chem. Lett.* **2018**, *9*, 3998–4005.

[175] D. T. Limmer, N. S. Ginsberg, *J. Chem. Phys.* **2020**, *152*, 230901.

[176] B. Guzelturk, T. Winkler, T. Van de Goor, M. D. Smith, S. A. Bourelle, S. Feldmann, M. Trigo, S. Teitelbaum, H.-G. Steinrück, G. A. de la Pena, R. Alonso-Mori, D. Zhu, T. Sato, H. I. Karunadasa, M. F. Toney, F. Deschler, A. M. Lindenberg, **2020**, DOI 10.48550/ARXIV.2011.03103.

[177] W. H. Sio, C. Verdi, S. Poncé, F. Giustino, *Phys. Rev. Lett.* **2019**, *122*, 246403.

[178] W. H. Sio, C. Verdi, S. Poncé, F. Giustino, *Phys. Rev. B* **2019**, *99*, 235139.

[179] K. Miyata, D. Meggiolaro, M. T. Trinh, P. P. Joshi, E. Mosconi, S. C. Jones, F. De Angelis, X.-Y. Zhu, *Sci. Adv.* **2017**, *3*, e1701217.

[180] D. Emin, *Journal of Applied Physics* **2018**, *123*, 055105.

[181] J. Wiktor, F. Ambrosio, A. Pasquarello, *J. Mater. Chem. A* **2018**, *6*, 16863–16867.

[182] T. Kirchartz, T. Markvart, U. Rau, D. A. Egger, *J. Phys. Chem. Lett.* **2018**, *9*, 939–946.

[183] P. B. Allen, V. Heine, *J. Phys. C: Solid State Phys.* **1976**, *9*, 2305–2312.

[184] P. B. Allen, M. Cardona, *Phys. Rev. B* **1983**, *27*, 4760–4769.

[185] B. Monserrat, N. D. Drummond, R. J. Needs, *Phys. Rev. B* **2013**, *87*, 144302.

[186] M. Zacharias, F. Giustino, *Phys. Rev. B* **2016**, *94*, 075125.

[187] F. Giustino, *Rev. Mod. Phys.* **2017**, *89*, 015003.

[188] F. Karsai, M. Engel, E. Flage-Larsen, G. Kresse, *New J. Phys.* **2018**, *20*, 123008.

[189] W. A. Saidi, S. Poncé, B. Monserrat, *J. Phys. Chem. Lett.* **2016**, *7*, 5247–5252.

[190] A. Francisco-López, B. Charles, O. J. Weber, M. I. Alonso, M. Garriga, M. Campoy-Quiles, M. T. Weller, A. R. Goñi, *J. Phys. Chem. Lett.* **2019**, *10*, 2971–2977.

[191] A. Thongnum, U. Pinsook, *Nanoscale* **2020**, *12*, 14112–14119.

[192] A. S. Mishchenko, L. Pollet, N. V. Prokof'ev, A. Kumar, D. L. Maslov, N. Nagaosa, *Phys. Rev. Lett.* **2019**, *123*, 076601.

[193] S. Poncé, M. Schlipf, F. Giustino, *ACS Energy Lett.* **2019**, *4*, 456–463.

[194] H. Oga, A. Saeki, Y. Ogomi, S. Hayase, S. Seki, *J. Am. Chem. Soc.* **2014**, *136*, 13818–13825.

[195] T. J. Savenije, C. S. Ponseca, L. Kunneman, M. Abdellah, K. Zheng, Y. Tian, Q. Zhu, S. E. Canton, I. G. Scheblykin, T. Pullerits, A. Yartsev, V. Sundström, *J. Phys. Chem. Lett.* **2014**, *5*, 2189–2194.

[196] R. L. Milot, G. E. Eperon, H. J. Snaith, M. B. Johnston, L. M. Herz, *Adv. Funct. Mater.* **2015**, *25*, 6218–6227.

[197] H. T. Yi, X. Wu, X. Zhu, V. Podzorov, *Adv. Mater.* **2016**, *28*, 6509–6514.

[198] S. Shrestha, G. J. Matt, A. Osvet, D. Niesner, R. Hock, C. J. Brabec, *J. Phys. Chem. C* **2018**, *122*, 5935–5939.

[199] A. Biewald, N. Giesbrecht, T. Bein, P. Docampo, A. Hartschuh, R. Ciesielski, *ACS Appl. Mater. Interfaces* **2019**, *11*, 20838–20844.

[200] A. F. Ioffe, A. R. Regel, *Prog. Semicond* **1960**, *4*, 237–291.

[201] N. F. Mott, *Philos. Mag.* **1972**, *26*, 1015–1026.

[202] B. A. A. Martin, J. M. Frost, *Phys. Rev. B* **2023**, *107*, 115203.

[203] L. V. Titova, T. L. Cocker, D. G. Cooke, X. Wang, A. Meldrum, F. A. Hegmann, *Phys. Rev. B* **2011**, *83*, 085403.

[204] D. G. Cooke, A. Meldrum, P. Uhd Jepsen, *Appl. Phys. Lett.* **2012**, *101*, 211107.

[205] A. H. Hill, C. L. Kennedy, E. S. Massaro, E. M. Grumstrup, *J. Phys. Chem. Lett.* **2018**, *9*, 2808–2813.

[206] A. Lacroix, G. T. de Laissardière, P. Quémerais, J.-P. Julien, D. Mayou, *Phys. Rev. Lett.* **2020**, *124*, 196601.

[207] J. L. M. van Mechelen, D. van der Marel, C. Grimaldi, A. B. Kuzmenko, N. P. Armitage, N. Reyren, H. Hagemann, I. I. Mazin, *Phys. Rev. Lett.* **2008**, *100*, 226403.

[208] J. T. Devreese, S. N. Klimin, J. L. M. van Mechelen, D. van der Marel, *Phys. Rev. B* **2010**, *81*, 125119.

[209] J.-J. Zhou, M. Bernardi, *Phys. Rev. Research* **2019**, *1*, 033138.

[210] J. Ma, L.-W. Wang, *Nano Lett.* **2015**, *15*, 248–253.

[211] M. E. Gershenson, V. Podzorov, A. F. Morpurgo, *Rev. Mod. Phys.* **2006**, *78*, 973–989.

[212] S. Fratini, M. Nikolka, A. Salleo, G. Schweicher, H. Sirringhaus, *Nat. Mater.* **2020**, *19*, 491–502.

[213] A. Troisi, G. Orlandi, *Phys. Rev. Lett.* **2006**, *96*, 086601.

[214] S. Fratini, D. Mayou, S. Ciuchi, *Adv. Funct. Mater.* **2016**, *26*, 2292–2315.

[215] S. Fratini, S. Ciuchi, D. Mayou, G. T. de Laissardière, A. Troisi, *Nat. Mater.* **2017**, *16*, 998–1002.

[216] S. Giannini, O. G. Ziogos, A. Carof, M. Ellis, J. Blumberger, *Adv. Theory Simul.* **2020**, *3*, 2000093.

[217] A. S. Eggeman, S. Illig, A. Troisi, H. Sirringhaus, P. A. Midgley, *Nature Mater.* **2013**, *12*, 1045–1049.

[218] M. Asher, D. Angerer, R. Korobko, Y. Diskin-Posner, D. A. Egger, O. Yaffe, *Adv. Mater.* **2020**, *32*, 1908028.

[219] Y. C. Cheng, R. J. Silbey, D. A. da Silva Filho, J. P. Calbert, J. Cornil, J. L. Brédas, *J. Chem. Phys.* **2003**, *118*, 3764–3774.

[220] J. H. Fetherolf, D. Golež, T. C. Berkelbach, *Phys. Rev. X* **2020**, *10*, 021062.

[221] D. J. Abramovitch, W. A. Saidi, L. Z. Tan, *Phys. Rev. Mater.* **2021**, *5*, 085404.

[222] A. Troisi, *Chem. Soc. Rev.* **2011**, *40*, 2347.

[223] M.-A. Stoeckel, Y. Olivier, M. Gobbi, D. Dudenko, V. Lemaur, M. Zbiri, A. A. Y. Guilbert, G. D'Avino, F. Liscio, A. Migliori, L. Ortolani, N. Demitri, X. Jin, Y.-G. Jeong, A. Liscio, M.-V. Nardi, L. Pasquali, L. Razzari, D. Beljonne, P. Samorì, E. Orgiu, *Adv. Mater.* **2021**, *33*, 2007870.

[224] S. Giannini, L. Di Virgilio, M. Bardini, J. Hausch, J. Geuchies, W. Zheng, M. Volpi, J. Elsner, K. Broch, Y. H. Geerts, F. Schreiber, G. Schweicher, H. I. Wang, J. Blumberger, M. Bonn, D. Beljonne, "Transiently Delocalized States Enhance Hole Mobility in Organic Molecular Semiconductors", **2023**.

[225] S. Boyer-Richard, C. Katan, B. Traoré, R. Scholz, J.-M. Jancu, J. Even, *J. Phys. Chem. Lett.* **2016**, *7*, 3833–3840.

[226] S. Ashhab, O. Voznyy, S. Hoogland, E. H. Sargent, M. E. Madjet, *Sci. Rep.* **2017**, *7*, 8902.

[227] G. Kresse, J. Furthmüller, *Phys. Rev. B* **1996**, *54*, 11169–11186.

[228] P. Mohazzabi, S. P. Shankar, *JAMP* **2018**, *06*, 602–612.

[229] P. Giannozzi, O. Baseggio, P. Bonfà, D. Brunato, R. Car, I. Carnimeo, C. Cavazzoni, S. de Gironcoli, P. Delugas, F. Ferrari Ruffino, A. Ferretti, N. Marzari, I. Timrov, A. Urru, S. Baroni, *J. Chem. Phys.* **2020**, *152*, 154105.

[230] S. Plimpton, *J. Comput. Phys.* **1995**, *117*, 1–19.

[231] C. W. Greeff, H. R. Glyde, *Phys. Rev. B* **1995**, *51*, 1778–1783.

[232] S. John, C. Soukoulis, M. H. Cohen, E. N. Economou, *Phys. Rev. Lett.* **1986**, *57*, 1777–1780.

[233] F. Urbach, *Phys. Rev.* **1953**, *92*, 1324–1324.

[234] C. Ayik, I. Studenyak, M. Kranjec, M. Kurik, *optics* **2014**, *4*, 76–83.

[235] G. Mannino, I. Deretzis, E. Smecca, A. La Magna, A. Alberti, D. Ceratti, D. Cahen, *J. Phys. Chem. Lett.* **2020**, *11*, 2490–2496.

[236] V. Bruevich, L. Kasaei, S. Rangan, H. Hijazi, Z. Zhang, T. Emge, E. Y. Andrei, R. A. Bartynski, L. C. Feldman, V. Podzorov, *Adv. Mater.* **2022**, *34*, 2205055.

[237] C. Q. Xia, J. Peng, S. Poncé, J. B. Patel, A. D. Wright, T. W. Crothers, M. Uller Rothmann, J. Borchert, R. L. Milot, H. Kraus, Q. Lin, F. Giustino, L. M. Herz, M. B. Johnston, *J. Phys. Chem. Lett.* **2021**, *12*, 3607–3617.

[238] Y. Chen, S. G. Motti, R. D. J. Oliver, A. D. Wright, H. J. Snaith, M. B. Johnston, L. M. Herz, M. R. Filip, *J. Phys. Chem. Lett.* **2022**, *13*, 4184–4192.

[239] A. Madhukar, W. Post, *Phys. Rev. Lett.* **1977**, *39*, 1424–1427.

[240] Y. Chang, C. H. Park, K. Matsuishi, *J. Korean Phys. Soc.* **2004**, *44*, 889–893.

[241] B. Traore, J. Even, L. Pedesseau, M. Képénekian, C. Katan, *Phys. Rev. Materials* **2022**, *6*, 014604.

[242] J. Feng, B. Xiao, *J. Phys. Chem. Lett.* **2014**, *5*, 1278–1282.

[243] Q. Chen, N. De Marco, Y. (Yang, T.-B. Song, C.-C. Chen, H. Zhao, Z. Hong, H. Zhou, Y. Yang, *Nano Today* **2015**, *10*, 355–396.

[244] K. Galkowski, A. Mitioglu, A. Miyata, P. Plochocka, O. Portugall, G. E. Eperon, J. T.-W. Wang, T. Stergiopoulos, S. D. Stranks, H. J. Snaith, R. J. Nicholas, *Energy Environ. Sci.* **2016**, *9*, 962–970.

[245] E. Mosconi, P. Umari, F. De Angelis, *Phys. Chem. Chem. Phys.* **2016**, *18*, 27158–27164.

[246] U.-G. Jong, C.-J. Yu, J.-S. Ri, N.-H. Kim, G.-C. Ri, *Phys. Rev. B* **2016**, *94*, 125139.

[247] Y. Yamada, H. Mino, T. Kawahara, K. Oto, H. Suzuura, Y. Kanemitsu, *Phys. Rev. Lett.* **2021**, *126*, 237401.

[248] A. Filippetti, A. Mattoni, C. Caddeo, M. I. Saba, P. Delugas, *Phys. Chem. Chem. Phys.* **2016**, *18*, 15352–15362.

[249] O. Hellman, P. Steneteg, I. A. Abrikosov, S. I. Simak, *Phys. Rev. B* **2013**, *87*, 104111.

[250] J. Even, L. Pedesseau, J.-M. Jancu, C. Katan, *J. Phys. Chem. Lett.* **2013**, *4*, 2999–3005.

[251] Y. Imry, *Phys. Rev. Lett.* **1980**, *44*, 469–471.

[252] H.-S. Duan, H. Zhou, Q. Chen, P. Sun, S. Luo, T.-B. Song, B. Bob, Y. Yang, *Phys. Chem. Chem. Phys.* **2015**, *17*, 112–116.

[253] J. H. Heo, D. H. Song, H. J. Han, S. Y. Kim, J. H. Kim, D. Kim, H. W. Shin, T. K. Ahn, C. Wolf, T.-W. Lee, S. H. Im, *Adv. Mater.* **2015**, *27*, 3424–3430.

[254] A. V. Cohen, D. A. Egger, A. M. Rappe, L. Kronik, *J. Phys. Chem. Lett.* **2019**, *10*, 4490–4498.

[255] J. D. Ziegler, J. Zipfel, B. Meisinger, M. Menahem, X. Zhu, T. Taniguchi, K. Watanabe, O. Yaffe, D. A. Egger, A. Chernikov, *Nano Lett.* **2020**, *20*, 6674–6681.

[256] Z. Guo, Y. Wan, M. Yang, J. Snaider, K. Zhu, L. Huang, *Science* **2017**, *356*, 59–62.

[257] M. T. Mihnev, F. Kadi, C. J. Divin, T. Winzer, S. Lee, C.-H. Liu, Z. Zhong, C. Berger, W. A. de Heer, E. Malic, A. Knorr, T. B. Norris, *Nat. Commun.* **2016**, *7*, 11617.

[258] J. D. Myers, J. Xue, *Polymer Reviews* **2012**, *52*, 1–37.